UNITED NATIONS EDUCATIONAL, SCIENTIFIC AND CULTURAL ORGANIZATION
INTERNATIONAL ATOMIC ENERGY AGENCY
INTERNATIONAL CENTRE FOR THEORETICAL PHYSICS
I.C.T.P., P.O. BOX 586, 34100 TRIESTE, ITALY, CABLE: CENTRATOM TRIESTE

H4.SMR/1013-13

SCHOOL ON THE USE OF SYNCHROTRON RADIATION
IN SCIENCE AND TECHNOLOGY:
"John Fuggle Memorial"

3 November - 5 December 1997

Miramare - Trieste, Italy

Progress in Surface Science

C. S. Fadley
Lawrence Berkeley Laboratory , California - USA

Volume 16 Number 3 1984

(2)

Progress in Surface Science

An International Review Journal

EDITOR: Professor Sydney G. Davison

ISBN 0 08 030892 9
ISSN 0079-6816
PSSFBP 16(3) 275–388 (1984)

PERGAMON PRESS
New York / Oxford / Toronto
Paris / Frankfurt / Sydney

Progress in Surface Science, Vol. 16, pp. 275-388, 1984.
Printed in the USA.

0079-6816/84 $0.00 + .50

ANGLE-RESOLVED X-RAY PHOTOELECTRON SPECTROSCOPY

CHARLES S. FADLEY

Department of Chemistry, University of Hawaii at Manoa, Honolulu, Hawaii 96822

Abstract

In this review, various aspects of angle-resolved x-ray photoelectron spectroscopy (ARXPS) as applied to solid state- and surface chemical- studies are discussed. Special requirements for instrumentation are first considered. The use of grazing-emission angles to enhance surface sensitivity and study surface concentration profiles of various types is then discussed. Various effects that may limit the accuracy of such measurements such as surface roughness, electron refraction, and elastic scattering are considered. Several examples of surface-specific electronic structure changes as studied by grazing-emission ARXPS (e.g., valence-band narrowing and core-level shifts) are also reviewed. The use of grazing-incidence geometries for surface enhancement is also briefly considered. Single-crystal studies providing additional types of information via ARXPS are next discussed. For core-level emission from single-crystal substrates or adsorbed overlayers, x-ray photoelectron diffraction (XPD) is found to produce considerable fine structure in polar- or azimuthal- scans of intensity. Such XPD effects can be very directly related to the atomic geometry near a surface, for example, through simple intramolecular or intermolecular scattering processes. A straightforward single scattering or kinematical theory also appears to describe such effects rather well, thus far permitting several structures to be solved by analyses of azimuthal intensity scans. Likely future developments and possible limitations of such XPD structure studies are also discussed. Finally, valence-band ARXPS is considered, and it is shown that pronounced direct-transition effects can be observed provided that the specimen Debye-Waller factor is not too small. A simple free-electron final-state model is found to predict these direct-transition effects very well, and future studies at low temperatures and with higher angular resolution seem promising.

Contents

Abbreviations

ARUPS	Angle-Resolved Ultraviolet Photoelectron Spectroscopy
ARXPS	Angle-Resolved X-ray Photoelectron Spectroscopy
ARXUPS	Angle-Resolved XUV Photoelectron Spectroscopy
DT	Direct Transition
EXAFS	Extended X-ray Absorption Fine Structure
ESDIAD	Electron Stimulated Desorption Ion Angular Distribution
FWHM	Full Width at Half Maximum Intensity
LEED	Low Energy Electron Diffraction
ME	Matrix Element
MS	Multiple Scattering
NDT	Non-Direct Transition
NPD	Normal Photoelectron Diffraction
PhD	Photoelectron Diffraction
RHEED	Reflection High Energy Electron Diffraction
SEXAFS	Surface Extended X-ray Absorption Fine Structure
SIMS	Secondary Ion Mass Spectrometry
SSC	Single Scattering Cluster
UHV	Ultra-High Vacuum
UPS	Ultraviolet Photoelectron Spectroscopy
XPD	X-ray Photoelectron Diffraction
XPS	X-ray Photoelectron Spectroscopy

1. Introduction

Angle-resolved photoelectron spectroscopy in fact has a rather long history, as recently reviewed by Jenkin et al.[1]. However, the current interest in angle-resolved x-ray photoelectron spectroscopy (ARXPS) as applied to solids and surfaces is only approximately ten years old, having begun with observations of diffraction-induced channeling effects in single-crystal specimens by Siegbahn et al.[2] and by Fadley and Bergström[3] and of enhanced surface sensitivity for grazing angles of emission by Fadley and Bergström[3]. A number of other effects of interest in surface science have been noted since these first studies, and several quantitative models have been developed for describing them. This type of measurement has been treated in prior general reviews in 1974[4], 1976[5], and 1978[6], and the present discussion will thus principally stress those developments that have occurred in the past few years, particularly with regard to using ARXPS for quantitative surface analysis, surface atomic geometry investigations, and valence-band studies.

The XPS energy regime will here be defined in what might be termed the classical way so as to involve excitation at photon energies $\gtrsim$ 1.0 keV as derivable from standard x-ray tubes (e.g., using MgKα or AlKα radiation). The many very interesting studies performed to date at lower energies in angle-resolved uv- or xuv- photoelectron spectroscopy (ARUPS or ARXUPS) will thus not be considered in detail. However, at various points, comparisons of the characteristics of a given type of measurement (e.g., core-level photoelectron diffraction) as carried out in the low- and high- energy domains will be made. Further details concerning such lower-energy work as based upon both standard radiation sources and synchrotron radiation are contained in other reviews.[7-9]

It is useful to begin by considering a general experimental geometry for angle-resolved x-ray photoemission from a solid surface, as shown in Fig. 1. X-rays are incident at an angle $\theta_{h\nu}$ with respect to the surface. Photoelectrons are emitted into the acceptance solid angle of the analyzer Ω_a. The initial direction of a given trajectory into this solid angle is given by its polar angle θ (here measured with respect to the surface) and its azimuthal angle ϕ (measured with respect to some arbitrary direction in the plane of the surface). The angle between the direction of radiation propagation $\hat{k}_{h\nu}$ and the direction of electron emission $\hat{k}$ is defined to be α. In most current XPS systems, α is a constant fixed by the mechanical design, although much UPS work has been carried out with movable analyzers and thus variable α. In addition, the geometry shown here is somewhat special in that the directions of radiation propagation and electron emission

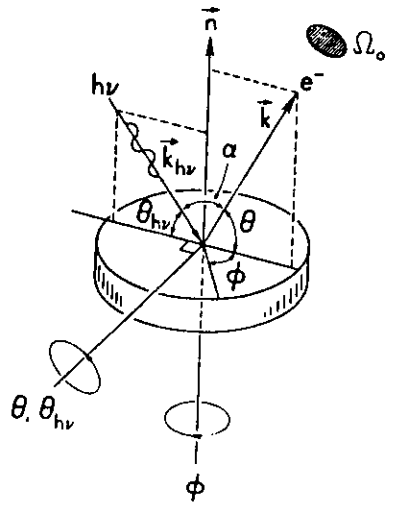

Fig. 1. General geometry for an angle-resolved photoemission experiment. Specimen rotations on the two perpendicular axes shown vary θ, ϕ, and $\theta_{h\nu}$ over their full allowed ranges. $\hat{n}$ is the surface normal. Movement of the electron analyzer relative to the radiation source also can be used to vary α and choose any θ, ϕ, $\theta_{h\nu}$, $\phi_{h\nu}$ combination, but in XPS this has been done very little to date.

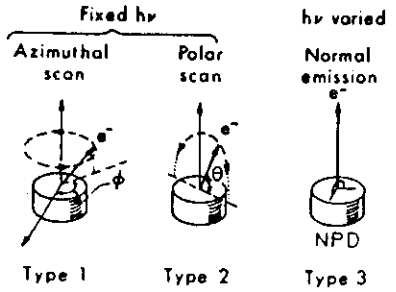

Fig. 2. Schematic illustration of three often-used types of angle-resolved photoemission experiments: (1) an azimuthal scan at constant polar angle, (2) a polar scan at constant azimuthal angle, and (3) a scan of hν at fixed normal emission (also referred to as normal photoelectron diffraction or NPD).

define a plane that also contains the surface normal. In this situation, rotation on the two perpendicular axes shown permits varying the angles θ, ϕ, and $\theta_{h\nu}$ over all possible values (consistent, of course with the geometric requirement that $\theta_{h\nu} + \alpha + \theta = \pi$). The θ, $\theta_{h\nu}$ axis is here taken to be perpendicular to the plane containing $\hat{k}_{h\nu}$, $\hat{k}$ and the surface normal, and the ϕ axis is parallel to the surface normal.

More general experimental geometries in which the analyzer can rotate on one or two axes with respect to the specimen and radiation source are also possible. In this case $\hat{k}_{h\nu}$ and $\hat{k}$ need not be co-planar with the surface normal and the four angles θ, ϕ, $\theta_{h\nu}$ and $\phi_{h\nu}$ are in general necessary to fully define the experiment. Such geometries have been used considerably in angle-resolved measurements at lower energies[7-9], but very little to date in the XPS regime. A final addition that is possible is the utilization of polarized radiation, as is just become practically possible in XPS studies with synchrotron radiation[10]; in this case, the angles θ_ε and ϕ_ε specifying the orientation of the polarization vector $\vec{\varepsilon}$ must also be known. However the standard XPS sources with which virtually all studies at $h\nu \gtrsim 1$ keV have to date been performed yield largely unpolarized radiation, so that we will only later comment briefly on polarization effects as an interesting subject for future investigation.

For a given photon energy hν, the two basic types of measurements possible in such experiments are thus an azimuthal scan at fixed polar angle (Type 1 of Fig. 2) and a polar scan at fixed azimuthal angle (Type 2 of Fig. 2). A third and more recently developed type of experiment[11] requiring the continuously tunable character of synchrotron radiation is also shown in Fig. 2; here, the emission direction is held parallel to the surface normal and hν is swept. In core-level studies, this type of measurement has been termed normal photoelectron diffraction or NPD.

The remainder of this discussion will consider specific problems and areas of application. In Section 2, instrumentation requirements are briefly considered. In Section 3, the general ideas relating to surface sensitivity enhancement at grazing emission are introduced, and various examples of the uses of this effect such as concentration profile measurements, overlayer studies, and investigations of surface-specific electronic structure changes are discussed. The less-utilized effect of surface-sensitivity enhancement at grazing x-ray incidence is briefly considered in Section 4. Section 5 discusses various types of effects involved in core-level emission from single crystals, particularly as related to deriving surface atomic geometry information. In Section 6, valence-level emission from single crystals is considered, largely from the point of view of its relationship to bulk valence band structure.

2. Instrumentation

Beyond the normal instrumentation requirements for an XPS experiment, which are reviewed elsewhere[6], those for adding the capability to do angle-resolved measurements are relatively straightforward.

The solid angle Ω_o over which electrons are accepted into the analyzer (cf. Fig. 1) needs to be well defined and reasonably small. Depending upon the application intended, a range of angles corresponding to $\Delta\theta \times \Delta\phi$ from a minimum of $\sim 1° \times \sim 1°$ to a maximum of $\sim 10° \times \sim 10°$ could be suitable. For the two most commonly utilized analyzer configurations, the hemispherical electrostatic and cylindrical mirror electrostatic, some degree of baffling thus is in general required to adequately define the solid angle, and this will, of necessity, reduce the overall intensity of the instrument. In certain hemispherical analyzers with pre-retarding lens systems, the solid angle may already be relatively well defined, as discussed in detail for one system by Baird and Fadley[12], but in general this is not at all the case, with much larger angular deflections of $\sim \pm 20°$-$30°$ being allowed in a direction perpendicular to the central reference trajectory of the analyzer. This loss of intensity associated with reducing Ω_o also suggests the use of some form of multichannel detection as a compensating factor. A further problem that may be encountered with any analyzer is that Ω_o may vary over the effective emitting area of the specimen and also may depend upon electron kinetic energy or other analyzer parameters, as, for example, the degree of retardation.[5] Such changes in solid angle and also in emitting area can in addition lead to a purely instrumental change in intensity with angle, usually dependent on θ only. Such instrument response functions are discussed in Section 3.C and in prior reviews[4-6,12]. In addition, some instruments will exhibit a change in energy resolution with θ that must be allowed for in precise analyses of spectra[12]. Plummer[13] has also recently considered general criteria for designing analyzers for angle-resolved studies over a range of energies.

In addition to defining Ω_o, it is necessary to be able to rotate the specimen so as to change the angles θ, ϕ, and perhaps also $\theta_{h\nu}$. A single polar axis of rotation varying θ and $\theta_{h\nu}$ is very easy to add in an overall geometry such as that of Fig. 1. A second azimuthal axis for varying ϕ requires additional mechanical complexity, but commercial manipulators providing at least partial azimuthal rotation are available, and custom designs with greater flexibility exist in several laboratories for both ARXPS[5] and ARUPS[14,15] measurements.

As one example of a reasonably flexible system for performing ARXPS at ultra-high vacuum conditions, Figs. 3 and 4 show different aspects of one unit currently in use in our laboratory. (An earlier high-vacuum device with a simpler

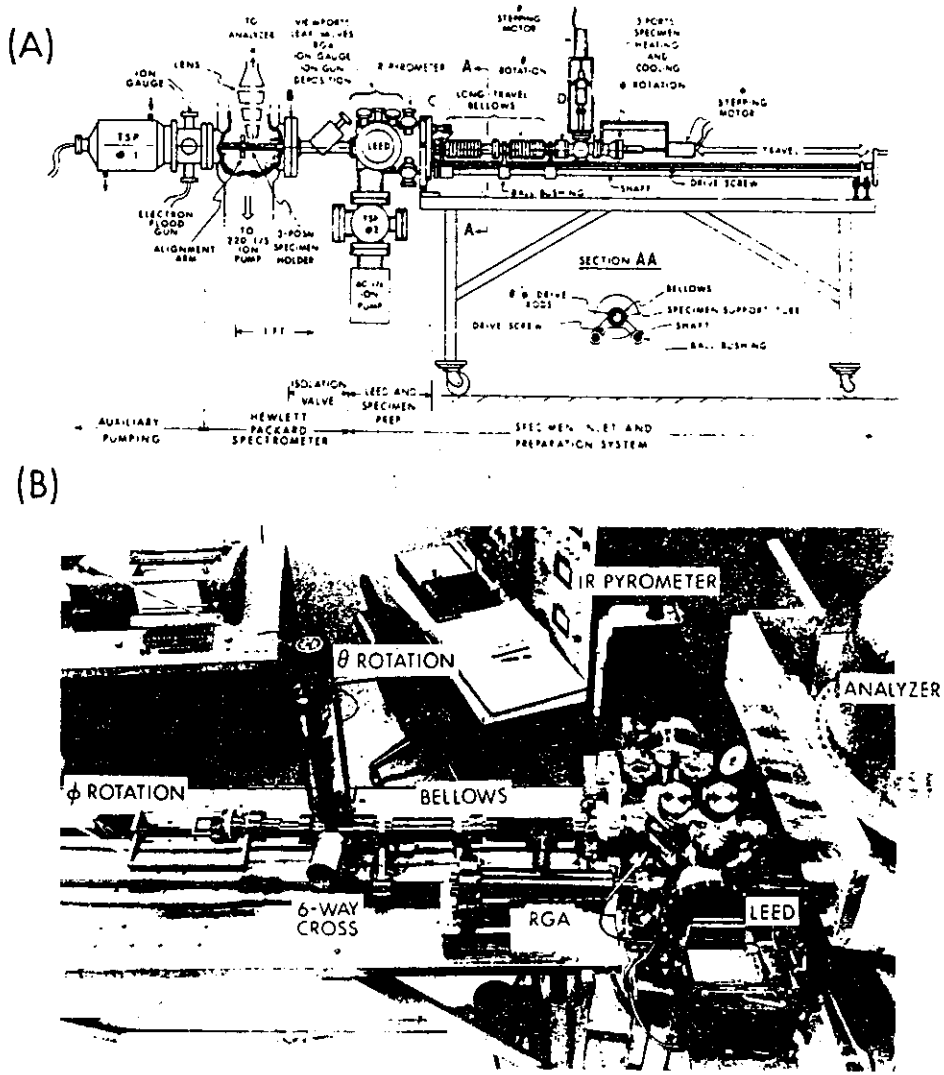

Fig. 3. (a) Schematic drawing of the specimen inlet side of a Hewlett Packard XPS spectrometer that has been specially modified for angle-resolved studies. Various components are labelled. (b) Overall photo of the system in (a) as viewed from the opposite side.

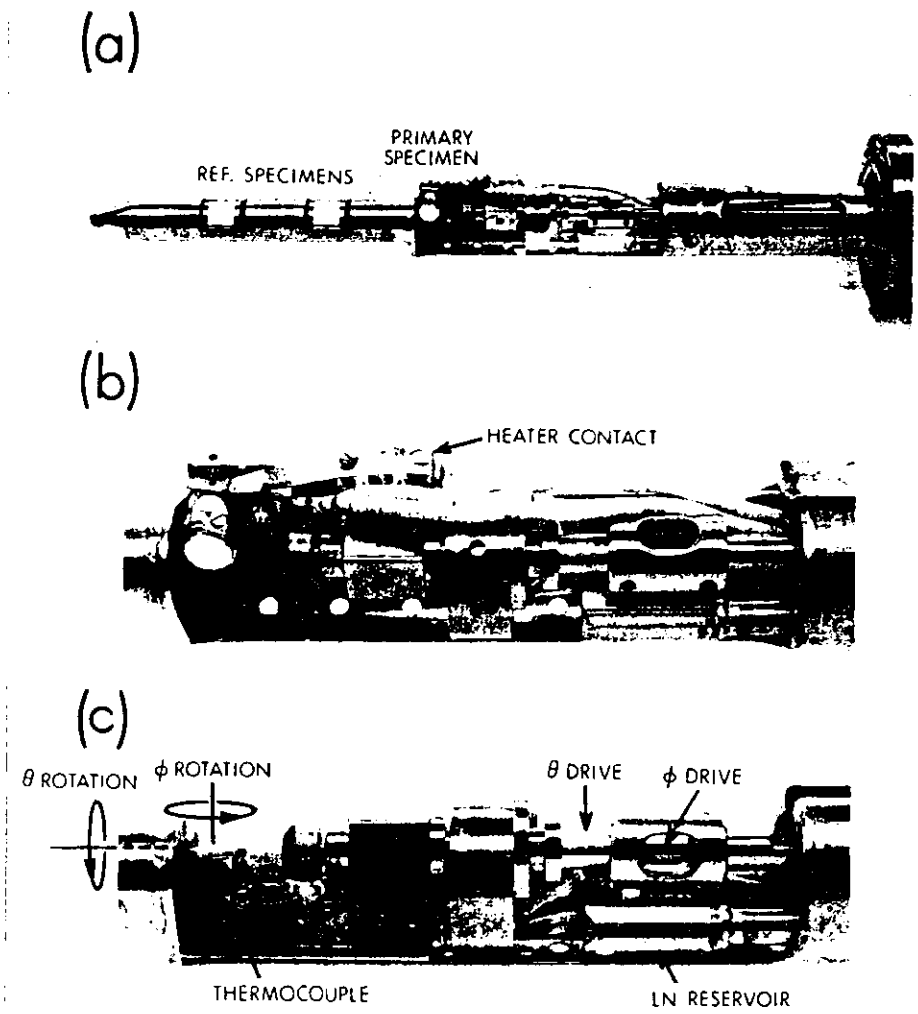

Fig. 4. Three different views of a two-axis goniometer used for variable-temperature ARXPS studies at angular accuracies of ≤±0.5°: (a) overview including reference sample positions, and (b),(c) two close ups with different polar orientation. The smaller-diameter section at left in (a) mates with an alignment arm in the analyzer (cf. Fig. 3(a)).

rack-and-pinion drive is described in ref. 5.) The basic XPS analyzer and chamber to which the specimen preparation chamber, specimen goniometer, and translating-bellows inlet system is mounted is a Hewlett-Packard Model 5950A. Fig. 3(a) is a line drawing of the overall system and Fig. 3(b) a photographic view from the isolation valve on the XPS chamber to the preparation chamber and inlet system. The interior specimen support tube translates on external ball bushings, and is controlled by a drive screw. Various standard components such as a LEED unit, residual gas analyzer, ion gun, leak valves, and infrared pyrometer permit cleaning, preparing, and characterizing specimens before admitting them to the XPS chamber through the isolation valve. Two rotary feedthrus driven by computer-controlled stepping motors permit precision scanning on the two axes shown in Fig. 1. These feedthrus are mounted on a six-way cross together with other feedthrus for electrical heating, thermocouple temperature measurement, and liquid nitrogen cooling. Full ultra-high vacuum operation is also achieved with this system, with base pressures in the XPS chamber of $\sim 4\text{-}6\times10^{-11}$ torr and in the preparation chamber of $\sim 8\text{-}10\times10^{-11}$ torr.

Fig. 4 shows three photographic views of the specimen end of this goniometer. The θ drive comes in on the vertical port of the six-way cross, turns a right angle with a set of bevel gears, and is then transmitted directly to the rotating specimen support arm via a 1/4" o.d. drive tube. This drive tube is supported on precision ball bearings over its entire length of ~110 cm. The φ drive enters via the rear port of the six-way cross and is transmitted via a straight internal drive shaft of 1/8" diameter to sets of bevel gears and then spur gears so as effect φ motion. The φ drive shaft is internal to and concentric with the θ drive tube. Precision stainless steel ball bearings are used at all rotation points. Although there is an overall lash in this system between the coupled θ and φ motions of $\lesssim 1°$ due to the various mechanical linkages involved, the consistent use of identical directions of rotation in making settings permits overall precisions and accuracies of $\lesssim 0.5°$ in both θ and φ. Particularly for the grazing-emission azimuthal scans to be discussed in Section 5, such accuracies appear to be absolutely required for obtaining reproducible data. The specimen can be heated up to ~1000°C with an internal resistive button heater (Varian No. 981-2058) to which current passes via a contact ring and a spring-loaded floating contact. Alternatively, an electron bombardment heater for temperatures up to ~2500°C can also be mounted in the same position. Thus, full azimuthal rotational freedom is maintained, an extremely useful feature in providing a self-consistency check on data from single crystals, where the crystal rotational symmetry should be mirrored in the azimuthal data. Thermocouple and liquid-nitrogen connections can also be made to points near the specimen as needed.

3. Surface Sensitivity Enhancement at Grazing Electron Emission Angles

A. Introduction

The basic mechanism of surface sensitivity enhancement at grazing emission angles is illustrated in Fig. 5 for the case of an idealized homogeneous, semi-infinite, flat-surface specimen in which any effects due to atomic positional order are assumed to be fully averaged over. The mean free path for inelastic scattering Λ_e is further taken to be a constant independent of emission angle. In this case, the mean depth of no-loss photoelectron emission as measured perpendicular to the surface is exactly equal to Λ_e for normal emission or $\theta = 90°$, but it decreases as $\Lambda_e \sin\theta$ for non-normal emission. For typical XPS mean free paths of 15-20 Å[16-18], this simple model thus predicts that between normal emission and grazing emission at $\theta = 10°$, the mean depth should decrease from roughly 8-10 atomic layers down to only ~2-3 atomic layers, respectively. Polar scans of photoelectron intensity are thus expected to exhibit varying degrees of surface sensitivity, as has been demonstrated in numerous prior investigations[4-6].

A qualitative illustration of how significant this low-θ effect can be is presented in Fig. 6, where broad-scan spectra are shown at three angles for a highly-polished Si specimen with an oxide overlayer approximately 1-2 atomic layers in thickness and an outermost overlayer of carbon-containing materials from the residual gas of approximately the same thickness[19]. The pronounced peaks due to the O1s, C1s, Si2s, and Si2p core levels are found to change dramatically in relative intensity as θ is changed from 70° (near normal) to 5° (grazing). With maximum bulk sensitivity at 70°, the Si peaks are most intense, then O1s, then C1s, but at 5°, this order is completely reversed. These results thus directly provide a qualitative depth profile of the specimen, with C lying outside O (present primarily as a Si oxide) and O lying outside the elemental Si of the substrate.

Closer examination of such oxidized Si spectra also shows Si core-level chemical shifts between oxide and element, with different angular behavior for the two, as illustrated in the results of Hill et al.[19] for a 14 Å oxide layer in Fig. 7. Here, the Si2p(oxide) peak is enhanced relative to Si2p(element) at low θ, as expected; the quantitative analysis of this type of overlayer data will be discussed further in Section 3.D.

A final and even more subtle example of the qualitative use of variable-θ data is provided by Si in some very recent results due to Grunthaner et al.[20] shown in Fig. 8. Here, the Si2p data from a chemically-cleaned surface exhibit a very small change in peak shape in going from $\theta = 38.5°$ to the more surface sensitive $\theta = 18.5°$. These results are also shown after a resolution enhancement procedure

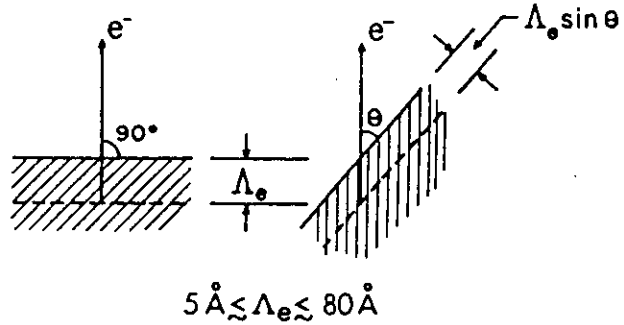

Fig. 5. Illustration of the basic mechanism producing surface sensitivity enhancement for low electron exit angles θ. The average depth for no-loss emission as measured perpendicular to the surface is $\Lambda_e \sin\theta$.

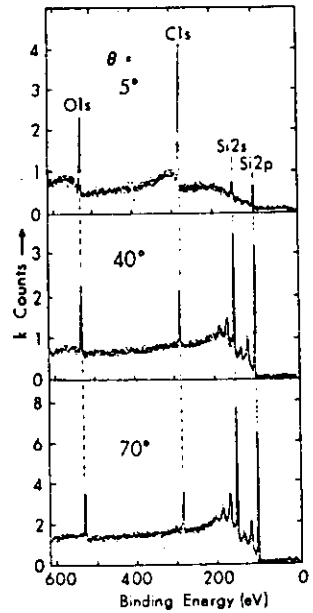

Fig. 6. Broad-scan core-level spectra at three electron exit angles between low and high values for a Si specimen with a thin oxide overlayer (~4Å) and an outermost carbon contaminant layer approximately 1 monolayer in thickness. Note the marked enhancement of the surface-associated O1s and C1s signals for low θ.

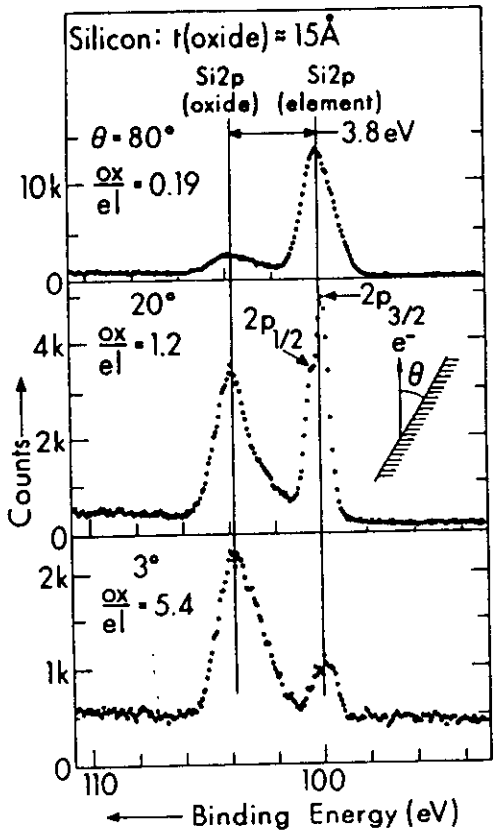

Fig. 7. Si2p spectra at three electron exit angles for a Si specimen with a 15-Å thick oxide overlayer. Note the complete reversal of the relative intensities of oxide and element between high and low θ. (From Hill et al., ref. (19).)

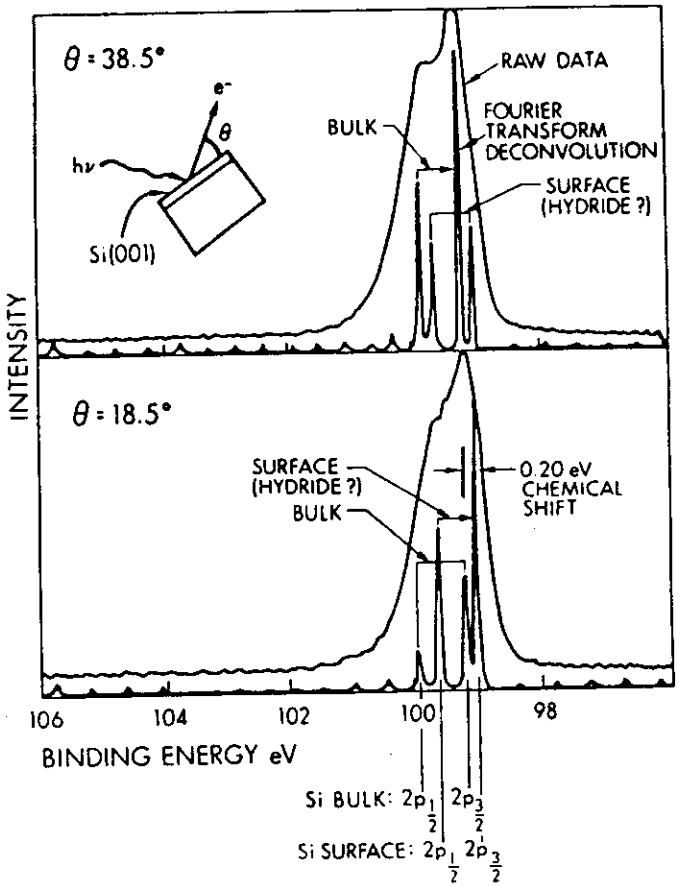

Fig. 8. Si2p spectra at two exit angles from a chemically-cleaned Si surface thought to have a surface hydride present. The raw data and curves obtained via a Fourier-transform (FT) deconvolution procedure are shown. Note the enhancement of the hydride FT peak at θ = 18.5°. (From Vasquez et al., ref. (20).)

using Fourier transform deconvolution to yield two doublets chemically shifted by only 0.30 eV from one another. The lower-binding-energy doublet is enhanced in relative intensity at low θ, suggesting a surface species. The fact that the 2:1 intensity ratio of the expected $2p_{3/2}$:$2p_{1/2}$ spin-orbit doublet is found in the area ratios of the peaks in each Fourier transform doublet for both angles lends further support to the results of the deconvolution procedure, and provides a further internal consistency check for it. The surface species is thought by the authors to be a chemically-produced hydride[20].

B. Simple quantitative models

In more quantitatively discussing such variations of peak intensities with polar angle, it is useful to consider the idealized spectrometer geometry shown in Fig. 9, as has been done in several prior studies[4-6,21,22]. Here, a uniform flux of x-rays I_o is taken to be incident at $\theta_{h\nu}$ on the atomically flat surface of a specimen of arbitrary thickness t. The radiation may in general be refracted into $\theta_{h\nu}' \neq \theta_{h\nu}$ inside the specimen, after which it penetrates to a depth z below the surface and excites a photoelectron from some level k. X-ray refraction will be negligible for $\theta_{h\nu} \gtrsim 1\text{-}2°$, so that it will not be considered further until the specific discussion of Section 4. Photoelectron excitation is described by the differential photoelectric cross section $d\sigma_k/d\Omega$. The k-level- derived photoelectrons travel to the surface, during which they can be inelastically attenuated according to $\exp(-z/\Lambda_e \sin\theta')$, where θ' is the internal propagation angle and $z/\sin\theta'$ is the path length to the surface. Elastic scattering in travelling to and escaping from the surface is for the moment neglected, although we will consider its possible effects later. In escaping from the surface, the photoelectrons may be refracted from θ' to the external propagation angle θ due to the surface barrier or inner potential V_o; refraction will also be neglected for the moment, although an estimate of the low-θ limit of validity of this approximation is presented later in this section. Next, the analyzer is assumed to be adequately described in terms of an effective solid angle of Ω_o acting over an effective source area of A_o (as measured perpendicular to the mean electron trajectory), so that all electrons emitted from within the dotted projection of A_o (the active specimen volume) into Ω_o are energy analyzed. Possible retardation from an initial energy of $E_{kin} \equiv E_k$ to a final energy of E_o during analysis is also indicated in Fig. 9. Finally, a detection efficiency D_o can be included which allows for either less than full counting of the electrons entering Ω_o (in which case $D_o < 1$) or the presence of a multichannel detection system (for which $D_o >> 1$). In general, the mean free path, the effective solid angle, the effective

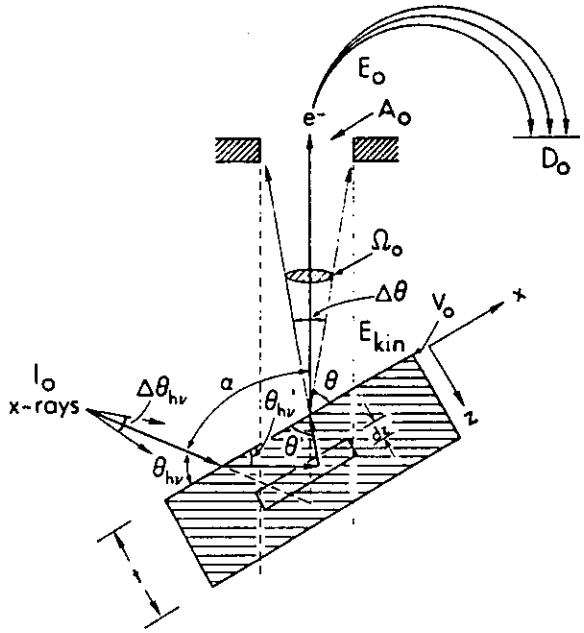

Fig. 9. Idealized spectrometer geometry for calculating angular-dependent photoelectron peak intensities, with various important parameters and variables indicated.

area, and the detection efficiency will depend on electron kinetic energy, so these will be written as $\Lambda_e(E_k)$, $\Omega_0(E_k)$, $A_0(E_k)$, and $D_0(E_k)$.

Within the assumptions of this simple, but for many experimental systems rather realistic, model, expressions for θ-dependent peak intensities can be directly derived for several useful specimen morphologies[4-6,21,22]. These are depicted in Fig. 10, where $N(\theta)$ denotes a θ-dependent photoelectron intensity, ρ denotes the atomic/molecular number density of the species on which the emitting level is located, a subscript k indicates a substrate level and a subscript ℓ denotes a level originating in an overlayer atom or molecule. Each of these cases will now be discussed, but we will return later in this section to consider several ways in which the model from which the equations have been derived may be somewhat oversimplified.

The different specimen morphologies are:

(i) Semi-infinite specimen, atomically clean surface, peak k with $E_{kin} \equiv E_k$. No θ dependence is predicted and the intensity is given by:

$$N_k^{\infty} \equiv I_0\Omega_0(E_k)A_0(E_k)D_0(E_k)\rho_k(d\sigma_k/d\Omega)\Lambda_e(E_k) \ . \qquad (1)$$

This case corresponds to an optimal measurement on a homogeneous specimen for which no surface chemical alteration or contaminant layer is present. The expression given permits predicting the absolute peak intensities resulting for a given specimen, or, of much more interest in practice, the relative intensities of the various peaks. If absolute intensities are to be derived, then the incident flux I_0 must be determined, as well as the kinetic energy dependences of the effective solid angle Ω_0, the effective specimen area A_0, and the detection efficiency D_0. In relative intensity measurements in which the quantity of interest is $N_k/N_{k'}$, for two peaks k and k', the I_0 factors will cancel, although the $\Omega_0 A_0 D_0$ factors need not due to their kinetic energy dependence. The densities ρ_k or $\rho_{k'}$ of the atoms or molecules on which subshell k or k' is located may be known beforehand, or may in many cases be the desired end result in quantitative chemical analyses using XPS. For core levels, the differential cross section $d\sigma_k/d\Omega$ can be calculated for either unpolarized or polarized radiation from a knowledge of the total subshell cross section σ_k and the asymmetry parameter β_k via[6,23-25]

$$\frac{d\sigma_k}{d\Omega} = \frac{\sigma_k}{4\pi}[1 + \beta_k(\tfrac{3}{2}\sin^2\alpha - 1)]. \qquad (2)$$

Within a one-electron central-potential model, tabulations of theoretical relativistic $\sigma_{n\ell j}$'s by Scofield[23] and non-relativistic $\beta_{n\ell}$'s by Reilman et al.[24] can be used to determine $d\sigma_{n\ell j}/d\Omega$, or the non-relativistic results of Goldberg et al.[25] for $\sigma_{n\ell}$ and $\beta_{n\ell}$ for a number of atoms can be used. All of these tabulations

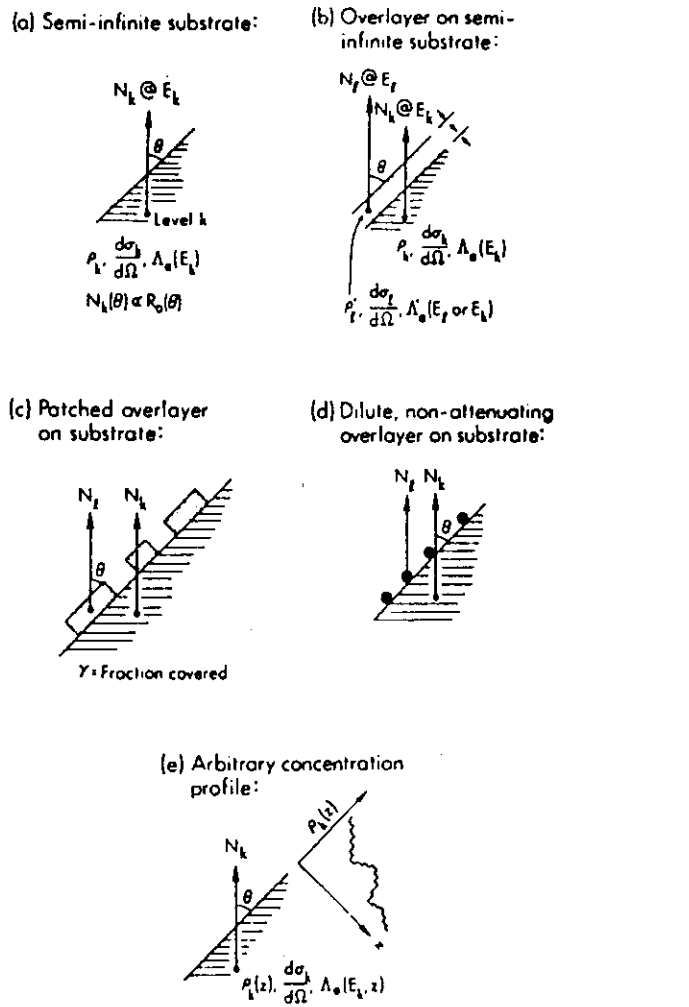

Fig. 10. Several specimen morphologies for which variable-θ peak intensities can be used in order to derive concentration profiles and other analytical information: (a) a uniform semi-infinite substrate, (b) a semi-infinite substrate with a uniform surface overlayer, (c) a semi-infinite substrate with a patched surface overlayer, (d) a semi-infinite substrate with a dilute, non-attenuating overlayer (e.g., a fractional monolayer coverage of an adsorbate), and (e) a semi-infinite substrate with arbitrary concentration profiles inward from the surface.

eV), as well as several lower energies[23,25]. Possible effects of multi-electron processes on the use of such cross sections are discussed elsewhere[6]. For valence levels involved in bonding, the determination of $d\sigma_k/d\Omega$ is more complex[6]. The last quantity involved is $\Lambda_e(E_k)$ which can either be taken from tabulations of previously measured values[18-18], or, within a given specimen, be estimated from Penn's theoretical treatment[26]. More simply, its dependence on kinetic energy for $E_k \gtrsim$ a few hundred eV can be assumed to follow an empirical square-root dependence as[6,18]: $\Lambda_e(E_k) \propto (E_k)^{1/2}$; this relationship thus permits determining Λ_e's at any energy for a given specimen provided that a single value is known.

Note that there is no θ dependence in N_k within this simple model, a prediction that was first made and verified experimentally by Henke[21]. Its origin lies in the fact that the effective emitting depth is $\Lambda_e\sin\theta$ (cf. Fig. 5), while the effective specimen surface area is $A_o/\sin\theta$ (cf. Fig. 9); the effective specimen volume at any θ is thus the product of the two, in which the $\sin\theta$ factors cancel. This behavior is expected to hold as long as θ is not made so small that the edges of the specimen lie within the aperture A_o[4,5]. For such low θ values an additional $\sin\theta$ factor appears in Eq. (1). This is one illustration of the origins of instrument-specific response functions modulating intensities[4,5,12]. This effect generally leads to the unfortunate characteristic that intensities at grazing emission are markedly reduced compared to those at higher θ.

Prior tests of Eq. (1) in the quantitative analysis of homogeneous samples at relatively high emission angles have generally yielded results in agreement with experimental peak ratios to within $\sim\pm$10%, as discussed elsewhere[6,27-29].

(ii) Specimen of thickness t, atomically clean surface, peak k with $E_{kin} \equiv E_k$. The intensity in this case is given by

$$N_k(\theta) = I_o\Omega_o(E_k)A_o(E_k)D_o(E_k)\rho_k(d\sigma_k/d\Omega)\Lambda_e(E_k)[(1-\exp(-t/\Lambda_e(E_k)\sin\theta)]$$
$$= N_k^{\infty}[1-\exp(-t/\Lambda_e(E_k)\sin\theta)]. \qquad (3)$$

Here, the intensity of a peak originating in a specimen of finite thickness is predicted to increase with decreasing θ (again with the proviso that θ not be so small that the specimen edges lie within A_o).

(iii) Semi-infinite substrate with uniform overlayer of thickness t. As first discussed by Fraser et al.[22], the two types of intensities here are:

Peak k from substrate with $E_{kin} \equiv E_k$:

$$N_k(\theta) = I_o\Omega_o(E_k)A_o(E_k)D_o(E_k)\rho_k(d\sigma_k/d\Omega)\Lambda_e(E_k)\exp(-t/\Lambda_e'(E_k)\sin\theta)$$
$$= N_k^{\infty}\exp(-t/\Lambda_e'(E_k)\sin\theta), \qquad (4)$$

Peak ℓ from overlayer with $E_{kin} \equiv E_\ell$:

$$N_\ell(\theta) = I_o\Omega_o(E_\ell)A_o(E_\ell)D_o(E_\ell)\rho_\ell'(d\sigma_\ell/d\Omega)\Lambda_e'(E_\ell)[1-\exp(-t/\Lambda_e'(E_\ell)\sin\theta]$$
$$= N_\ell^{\infty}[1-\exp(-t/\Lambda_e'(E_\ell)\sin\theta)] \qquad (5)$$

where

Λ_e = an attenuation length in the substrate

Λ_e' = an attenuation length in the overlayer

ρ = an atomic density in the substrate

ρ' = an atomic density in the overlayer .

Or, it is often more convenient to deal with peak ratios in which I_o and any purely instrumental variations with θ cancel:

Overlayer/substrate ratio:

$$R(\theta) \equiv \frac{N_\ell(\theta)}{N_k(\theta)} = \frac{\Omega_o(E_\ell)A_o(E_\ell)D_o(E_\ell)\rho_\ell'(d\sigma_\ell/d\Omega)\Lambda_e'(E_\ell)}{\Omega_o(E_k)A_o(E_k)D_o(E_k)\rho_k(d\sigma_k/d\Omega)\Lambda_e(E_k)} \times [1-\exp(-t/\Lambda_e'(E_\ell)\sin\theta)]\exp(t/\Lambda_e'(E_k)\sin\theta) \qquad (6)$$
$$= \frac{N_\ell^{\infty}}{N_k^{\infty}} \times [1-\exp(-t/\Lambda_e'(E_\ell)\sin\theta)]\exp(t/\Lambda_e'(E_k)\sin\theta).$$

This case represents a much more common experimental situation in which the primary specimen acts as substrate and possesses an intentional or unintentional contaminant overlayer (for example, an oxide on a semiconductor as in Figs. 6 and 7 or a layer deposited from the spectrometer residual gases). Substrate peaks are attenuated by inelastic scattering in the overlayer, an effect that is much enhanced at low θ. The overlayer/substrate ratio is thus predicted to increase strongly as θ decreases, and this model provides a quantitative description of the effects discussed qualitatively in the previous section. It is also useful to consider several trivial modifications of Eqs. (4)-(6) that have been found useful in analyzing data. Rearranging Eq. (4) and taking the logarithm yields[30]

$$\ell n\left[\frac{N_k(\theta)}{N_k^{\infty}}\right] = -\frac{t}{\Lambda_e'(E_k)\sin\theta}, \qquad (7)$$

and proceeding similarly for Eq. (5) gives

$$\ell n\left[1-\frac{N_\ell(\theta)}{N_\ell^{\infty}}\right] = \frac{t}{\Lambda_e'(E_\ell)\sin\theta}. \qquad (8)$$

In Eq. (6), if the two kinetic energies E_k and E_ℓ are very nearly equal (as, for example, in chemically-shifted peaks such as those of Fig. 7), then $\Lambda_e'(E_k) = \Lambda_e'(E_\ell)$ (although in general $\Lambda_e'(E_\ell) \neq \Lambda_e(E_k)$ because they apply to different materials) and the $\Omega_oA_oD_o$ products will cancel in the ratio. Defining

$K \equiv \frac{N_\ell^\infty}{N_k^\infty}$ then yields after similar manipulation[19]

$$\ell n\left[\frac{R(\theta)}{K}+1\right] = \frac{t}{\Lambda_e'(E_k)\sin\theta} \quad (9)$$

Eqs. (7)-(9) thus represent linearized methods for plotting data versus $1/\sin\theta$ that will be considered further in Section (3.D), where the quantitative use of this model is discussed. The slopes of such plots are thus given by plus or minus the effective overlayer thickness $\tau \equiv t/\Lambda_e'$.

(iv) Semi-infinite substrate with a uniform, but patched, overlayer of thickness t[5,31,32]. If the fraction of surface area covered by the overlayer is γ, that uncovered is thus $(1-\gamma)$, and the resultant intensities are given by:

Peak k from substrate:

$$N_k(\theta) = (1-\gamma)(\text{Eq. (1)}) + \gamma(\text{Eq. (4)})$$
$$= N_k^\infty[(1-\gamma) + \gamma\exp(-t/\Lambda_e'(E_k)\sin\theta)] \quad (10)$$

Peak ℓ from overlayer:

$$N_\ell(\theta) = \gamma(\text{Eq. (5)})$$
$$= \gamma N_\ell^\infty [1-\exp(-t/\Lambda_e'(E_\ell)\sin\theta)] \quad (11)$$

Overlayer/substrate ratio:

$$\frac{N_\ell(\theta)}{N_k(\theta)} = \frac{N_\ell^\infty}{N_k^\infty}\,\gamma\,[1-\exp(-t/\Lambda_e'(E_\ell)\sin\theta)] \times [(1-\gamma) + \gamma\exp(-t/\Lambda_e'(E_k)\sin\theta)]^{-1}. \quad (12)$$

The overlayer/substrate ratio thus has a θ dependence different from Eq. (6), and, in particular, the enhancement of the overlayer relative intensity at low θ is predicted to be less pronounced in the presence of patching or clustering. This model might be expected to apply for overlayer growth in which the overlayer material (for example, a metal) is more compatible with itself than the substrate, or could also be qualitatively useful as an extreme representation of the effects of non-uniform overlayer growth (for example, in certain types of oxide formation). This model has been compared previously with experimental results[31,32], although it is not clear that patching effects can be clearly distinguished from those due to other phenomena such as surface roughness (to be discussed below).

(v) Semi-infinite substrate with a very thin, non-attenuating overlayer. One important example of such a specimen type is an adsorbate present on a substrate at fractional monolayer coverage. The relevant intensities are[5,6]:

Peak k from substrate:

$$N_k(\theta) = N_k^\infty \text{ as Eq. (1)} \quad (13)$$

Peak ℓ from overlayer:

$$N_\ell(\theta) = I_o\Omega_o(E_\ell)A_o(E_\ell)D_o(E_\ell)s'(d\sigma_\ell/d\Omega)(\sin\theta)^{-1} \quad (14)$$

Overlayer/substrate ratio:

$$\frac{N_\ell(\theta)}{N_k(\theta)} = \frac{\Omega_o(E_\ell)A_o(E_\ell)D_o(E_\ell)s'(d\sigma_\ell/d\Omega)d}{\Omega_o(E_k)A_o(E_k)D_o(E_k)s(d\sigma_k/d\Omega)\Lambda_e(E_k)\sin\theta} = \left[\frac{s'}{s}\right] \times \frac{D_o(E_\ell)\Omega_o(E_\ell)A_o(E_\ell)(d\sigma_\ell/d\Omega)d}{D_o(E_k)\Omega_o(E_k)A_o(E_k)(d\sigma_k/d\Omega)\Lambda_e(E_k)\sin\theta} \quad (15)$$

with

- s' = the mean surface density of overlayer atoms in which peak ℓ originates (in cm^{-2})
- s = the mean surface density of substrate atoms (in cm^{-2})
- s'/s = the fractional monolayer coverage of the atomic species in which peak ℓ originates
- d = the mean separation between layers of density s in the substrate (calculable from s/ρ).

These expressions are useful in surface-chemical studies at very low exposures to adsorbate molecules ($s'/s \lesssim 1$), as they permit an estimation of the fractional monolayer coverage from observed peak intensities. The assumption of no inelastic attenuation in the overlayer is an extreme one, but is justified because the macroscopic Λ_e' of case (iii) is both difficult to estimate and dubious in its application to such thin, non-macroscopic layers, and also because it represents a correct limiting form for zero coverage. A recent attempt to quantitatively assess the utility of this analysis[33] is discussed below in Section 3.E.

(vi) An arbitrary concentration profile $\rho_k(z)$ of a given species in a semi-infinite substrate[34].

Peak k from a species of interest:

As a first approximation to such a situation, if the mean free path $\Lambda_e(E_k)$ can be assumed to be constant with depth z and thus independent of the composition change associated with $\rho_k(z)$, a simple summation over atomic layers with spacing d at depths of $z_n = nd$ ($n = 1,2, \ldots \infty$) can be made to yield:

$$N_k(\theta) = I_o\Omega_o(E_k)A_o(E_k)D_o(E_k)\Lambda_e(E_k)(d\sigma_k/d\Omega) \times \sum_{n=1}^{\infty}\rho_k(z_n)\exp(-z_n/\Lambda_e(E_k)\sin\theta) . \quad (16)$$

If Λ_e depends on z also as $\Lambda_e(E_k,z)$, the resulting expression is, however, considerably more complex[34]:

$$N_k(\theta) = I_o\Omega_o(E_k)A_o(E_k)D_o(E_k)(d\sigma_k/d\Omega) \times \sum_{n=1}^{\infty} [\rho_k(z_n)(1-\exp(-d/\Lambda_e(E_k,z_n)\sin\theta)) \prod_{\substack{m=1 \\ (n\geq 2)}}^{n-1} \exp(-d/\Lambda_e(E_k,z_n)\sin\theta)] \quad (17)$$

Taking ratios of two such intensities N_k and N_k' as derived from species with different concentration profiles has been suggested as a method for deriving profiles by Hollinger et al.[34], although a complex, multiparameter fit to the θ-dependent data results, and it appears that physically reasonable constraints must be placed on the forms of $\rho_k(z)$ to yield unique solutions. Vasquez and Grunthaner[35] have also considered a very similar model for oxide growth in fixed-angle XPS measurements. This method is discussed in more detail in Section 3.F.

C. Additional complicating effects

With reference to the idealized spectrometer geometry of Fig. 9 and a few further assumptions made in arriving at the results of the last section, there are several additional effects that need to be considered in order to fully understand the behavior of experimental data.

(i) The instrument response function. Beyond the extreme low-θ deviation of intensities from the constancy predicted by Eq. (1) that we have mentioned before, additional purely instrumental effects can be introduced by a non-uniform x-ray flux (as, for example, will be produced by most x-ray monochromators[12]) and a solid angle that varies over the active portion of the specimen. All of these factors can be combined into an effective instrument response function, as discussed in detail in prior reviews[4-6]. Denoting this by $R_o(E_k,\theta)$, it is conveniently defined in terms of an integral over differential surface elements of the product of spatially varying x-ray flux I, solid angle Ω, and detection efficiency D. The specimen surface can be considered to lie in the x,y plane, thus yielding[5]

$$R_o(E_k,\theta) \equiv \sin\theta \int_A I(\theta,x,y)\Omega(E_k,\theta,x,y)D(E_k,\theta,x,y)dxdy . \quad (18)$$

The detection efficiency will depend principally on E_k and so can probably be removed from the integral. With this definition, any of Eqs. (1) and (3)-(17) can be modified so as to apply to an arbitrary spectrometer simply by replacing the combined factor $I_o(E_k)\Omega_o(E_k)A_o(E_k)D_o(E_k)$ by $R_o(E_k,\theta)$. Inspection of Eq. (1) with and without R_o inserted shows that the form of such a response function can be empirically determined simply by measuring the θ dependence (and perhaps also the E_k dependence) of the k photoelectron intensity originating from a homogeneous semi-infinite specimen with a clean surface (cf. Fig. 10(a)).

Examples of non-ideal response functions are shown in Fig. 11. Here, curves calculated with a slightly simplified version of Eq. (18) are compared with experimental points obtained with a Hewlett Packard spectrometer[12]. These results are for a system with monochromatized radiation in which I is very strongly peaked in the middle of the specimen surface, but for which the Ω_o, A_o approximation of Fig. 9 is essentially valid. Also shown in Fig. 11 is the measured response function for a Vacuum Generators ESCALAB spectrometer; note that it comes much closer to the constancy with θ predicted by Eq. (1), as its non-monochromatized source yields a much more nearly uniform x-ray flux.

It is finally reasonable to suppose that for some spectrometers, $R_o(E_k,\theta)$ will have the same functional form in θ regardless of E_k[5,12], and in this case, that any intensity ratio $N_k(\theta)/N_{k'}(\theta)$ from a given specimen will yield θ variations independent of instrument effects. (Clark and co-workers[36] have noted, however, that this simplification may not hold for all analyzer systems.) Thus, such peak ratios should in general be more amenable to straightforward analysis, although they still may carry information on the E_k dependence of R_o. For example, an energy dependence of Ω_o as shown in Fig. 12[37] must be considered in analyzing peak ratios at any θ for the Hewlett Packard instrument of Figs. 3 and 11.

(ii) Surface roughness effects. The qualitative effects of surface roughness are illustrated in Fig. 13(a), and they are twofold: (1) For a given macroscopic or experimental angle of emission θ as measured with respect to the planar average of the roughness, the microscopic or true emission angle θ^t at an arbitrary surface point may be significantly different. Thus, the true degree of surface enhancement at low θ may differ appreciably from that expected on the basis of the macroscopic θ alone. (2) Certain regions on the surface may be shaded for emission at a given θ by adjacent raised areas, as indicated by the cross-hatched regions in Fig. 13(a). Such shading will tend to be fully effective if the roughness contours are large with respect to typical Λ_e values of 10-40 Å, or only partial if the contours are on the scale of Λ_e. In any case, regions of the surface will be selected by shading as being more active in emission, and over these regions, it is an integration of the true-angle emission behavior that will correctly predict the observed intensities.

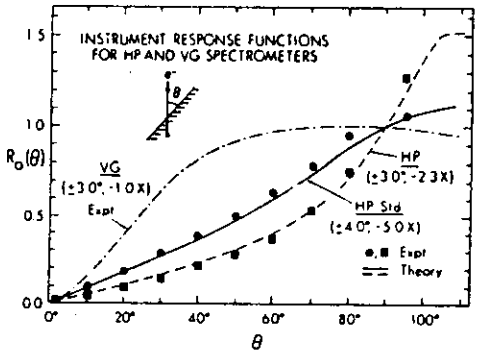

Fig. 11. Instrument response functions $R_0(\theta)$ for two different spectrometer systems, a Hewlett Packard 5950A with monochromatized AlKα x-ray source and α = 72° and a VG ESCALAB5 with a standard AlKα source and α = 48°. All curves have arbitrarily been set to 1.0 at θ = 90° (electron emission normal to the surface). For the HP system, two different entry lens magnifications have been used: standard of 5.0X and a second option of 2.3X. Cls intensities were used for the HP results; $Cu2p_{3/2}$ for the VG. Note the different shapes of the curves, with the monochromatized system showing greater deviations from the simple predictions of Eq. (1) of a constant response function. (From ref. (12) plus R.C. White and C.S. Fadley, unpublished results.)

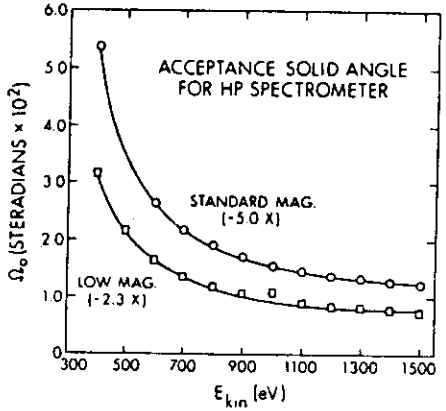

Fig. 12. Kinetic energy dependence of the solid angle of acceptance into a Hewlett Packard 5950A spectrometer, as determined from detailed electron trajectory calculations for two different entry lens magnifications. (From Baird, ref. (37).

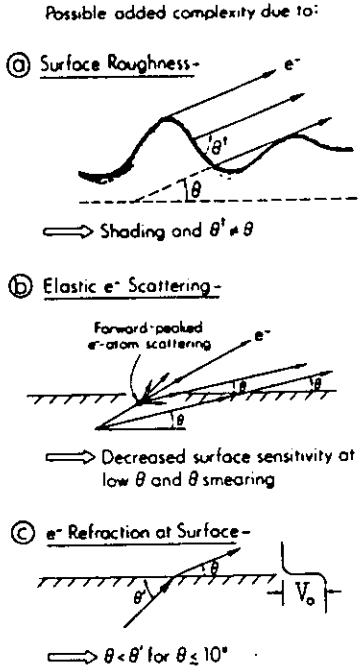

Fig. 13. Illustration of three effects providing additional complexities in the analysis of angle-resolved peak intensities: (a) surface roughness, (b) elastic electron scattering, and (c) electron refraction in crossing the surface barrier V_0.

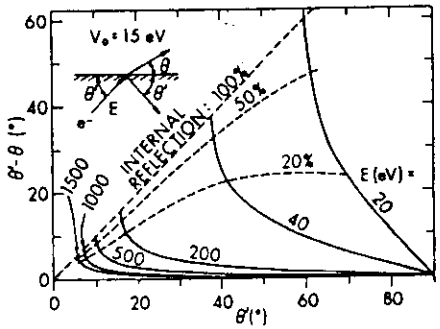

Fig. 14. Calculation of electron refraction effects for different electron kinetic energies and a typical V_0 value of 15eV. The degree of refraction is indicated by the difference θ' (internal) − θ (external). Contours of equal probability of internal reflection are also shown. (From ref. (5).)

In prior investigations[4,5,38,39], roughness effects have been considered for several idealized topographies from both a theoretical and experimental point of view. For example, the triangular-periodic surfaces of aluminum diffraction gratings with thin oxide overlayers exhibit dramatic angular variations in the Al2p(oxide)/Al2p(metal) ratio that are fully consistent with theoretical calculations incorporating the two effects mentioned above[38]. The precise form of the effects seen depends strongly on the exact nature of the profile, which is usually not known for an arbitrary specimen unless it has been very carefully prepared. However, it is possible to conclude that the presence of roughness will in general reduce the degree of surface sensitivity enhancement possible at low θ, although in the limit of very low θ, roughness with rounded contours should again give reasonable enhancement (i.e., an average $\theta_t \gtrsim \theta \gtrsim 0°$)[5].

Thus, roughness must be kept in mind as a possible source of deviations from the simple models of the last section for all specimens. However, even for rather randomly roughened surfaces, such effects do not seem to preclude the use of high-θ and low-θ comparisons to do qualitative depth profiling[39], as discussed in Section 3.A. Also, a procedure as simple as unidirectional course polishing of an aluminum surface and subsequent θ scanning in a plane parallel to the polishing grooves and normal to the surface is, for example, found to significantly enhance the amount of surface sensitivity enhancement at low θ[39].

(iii) Elastic electron scattering. Elastic electron scattering during photoelectron travel to and escape from the surface has been neglected in this simple model, but it could lead to several effects. Each interaction of the photoelectron wave with an atomic center will produce scattered intensity deviating from the initial propagation direction. Thus, the simple straight-line paths assumed in the model are not a fully accurate representation. Fortunately, at typical XPS energies of $\sim 10^3$ eV, the scattered intensity due to each atom will be strongly forward peaked; that is, most of the intensity will lie very close to the initial direction and will in fact be within $\sim \pm 10°$-$15°$ of it. (Such effects will be discussed in much more detail in Section 5, as they have been found to produce pronounced photoelectron diffraction effects in single-crystal studies.) But even in that case, there may be sufficient displacement of intensity to alter the final emission distribution significantly, especially at low θ. The possible effects of elastic scattering on grazing-emission surface enhancement have been discussed qualitatively for some time[5,19], but only rather recently have Nefedov et al.[40] attempted to quantitatively determine their nature and importance.

One important effect of elastic scattering will be to reduce surface sensitivity enhancement at low θ according to the mechanism of Fig. 13(b). For some very low

emission angle θ, the direct or unscattered wave travels along a long path of inelastic attenuation in reaching the surface. It is possible, however, that a wave initially propagating at some higher angle (and thus with a shorter path length to the surface) can be scattered just before escaping so as to yield significant intensity in the θ direction with respect to that of the direct wave. Thus, higher-θ relative intensities for different peaks can be scattered into lower-θ regions, reducing surface sensitivity enhancement. This discussion implicitly neglects any diffraction or interference effects between waves by assuming that the positions of the atomic scatterers are random and averaged over in different emission events. (For single-crystal specimens, such averaging does not occur and diffraction effects can be very strong.)

A second type of effect discussed by Nefedov et al.[40] is the effective lengthening of the average path length of a photoelectron caused by a random walk of elastic scattering events. Thus, they postulate that measured inelastic mean free paths λ_e are too large due to a lack of allowance for such elastic effects.

An example of possible elastic scattering effects is presented in Section 3.D in discussing ARXPS data for the SiO_2/Si system.

(iv) Electron refraction at the surface. As the photoelectron escapes from the surface, it must surmount a potential barrier or inner potential V_o that can be from 5-25 eV in magnitude for typical clean surfaces[41,42]. In doing so, the component of momentum perpendicular to the surface will be reduced, along with the kinetic energy, and a net refraction as shown in Fig. 13(c) will be produced. A fraction of the intensity can also be reflected back into the solid. As the internal angle θ' will thus always be greater than the external angle θ, refraction will act to decrease the degree of surface sensitivity enhancement relative to that expected at θ.

Such refraction and reflection effects can be easily calculated provided that V_o is known[5], and a family of curves for different kinetic energies E and a typical V_o of 15 eV is shown in Fig. 14. The equations utilized in calculating θ and the fractional internal reflection R_e for a given θ' are:

$$\theta = \tan^{-1}[(\sin^2\theta' - V_o/E)^{1/2}/\cos\theta'] \tag{19}$$

and

$$R_e = \left[\frac{1-(1-V_o/E\sin^2\theta')^{1/2}}{1+(1-V_o/E\sin^2\theta')^{1/2}}\right]^2 . \tag{20}$$

The difference θ'-θ between the internal and external angles is used as a gauge of the degree of refraction, and contours of equal percentage of internal reflection are also shown. From these results, it is clear that such refraction and

reflection effects can be very serious problems in measurements in the UPS regime of 20-40 eV. In the XPS region of ~500-1500 eV by contrast, refraction and reflection should not be significant for $\theta \gtrsim$ 10-15°, where $\theta'-\theta \lesssim 3°$ and the internal reflection is $\lesssim$ 10%. Nonetheless, such effects should be taken into account whenever possible in any fully quantitative analysis of ARXPS data for $\theta \lesssim$ 20-30°.

Having considered both the simple quantitative models applicable to ARXPS intensities and several effects which could cause deviations from them, we now turn to illustrative examples involving several specimen morphologies and several types of phenomena that it has been possible to study.

D. Applications to uniform overlayers

As one example of ARXPS as applied to the study of uniform overlayers, we consider work by Clark and co-workers[36] on polymer films deposited in situ on metal substrates. In this study, poly(p-xylylene) films of different thicknesses were deposited on a smooth Au substrate. Thicknesses t were measured with a quartz crystal deposition monitor. The Cls intensity from the film and $Au4f_{7/2}$ intensity from the substrate were measured at several θ values for each film, including values obtained in the limit of infinite thickness. Plots of

$$\ln\left[1-\frac{N_{Cls}(\theta)}{N^{\infty}_{Cls}}\right] \text{ and } \ln\left[\frac{N_{Au4f_{7/2}}(\theta)}{N^{\infty}_{Au4f_{7/2}}}\right] \text{ vs } t/\sin\theta$$

were then made, according to the linearized relations of Eqs. (7) and (8). Such data are shown in Fig. 15 and it is clear that the points for various thicknesses and θ values are very well described by a straight line. There is also very good agreement in the overlayer Λ_e' values obtained via least-squares fits for data at different θ's, as given for both the Cls and $Au4f_{7/2}$ kinetic energies on the figure. Varying θ thus provides a very useful additional dimension in such data. We note, however, that high θ values were utilized, being from 90° (normal emission) down to 40°, and thus that various additional effects expected to be stronger at low θ such as roughness, elastic scattering, and refraction have probably been minimized.

As a second case, we consider SiO_2 overlayers thermally grown on highly polished single-crystal Si substrates; some example data have already been shown in Fig. 7. In the first ARXPS study of this type by Hill et al.[19], four oxide thicknesses as determined by ellipsometry were studied and the θ dependence of the Si2p(oxide)/Si2p(element) ratio measured. As the kinetic energies of the two peaks are essentially identical, Eq. (9) provides a useful method for analyzing

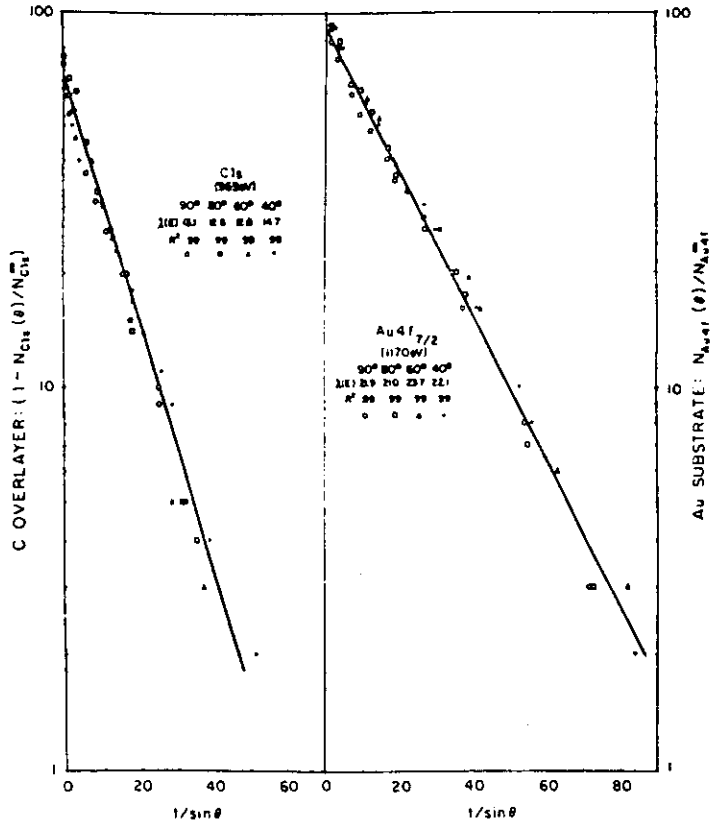

Fig. 15. Angle-resolved core-level intensities from a specimen consisting of a uniform overlayer of poly(p-xylyene) on a polycrystalline Au substrate. Overlayer Cls and substrate $Au4f_{7/2}$ intensities were measured at four θ values and for different overlayer thicknesses, and then plotted according to Eqs. (7) and (8). Line slopes were then used to derive $\Lambda_e(E)$ values in the overlayer (here indicated as λ(E)). (After Clark and Thomas, ref. (36).

the data, and a plot of $\ln[\frac{R(\theta)}{K} + 1]$ versus $t/\sin\theta$ is shown in Fig. 16 over a broad θ range from 90° to as low at 5°. The data were found to be linear over the θ range of 90° to 30°-40°, but showed similar deviations from linearity for lower θ values in a direction so as to reduce the relative intensity of the oxide peak. These deviations could be due to a combinations of factors: roughness, elastic scattering, electron refraction, incomplete averaging over single crystal effects, and the presence of a non-abrupt transition region between SiO_2 and Si[19]. More recently, Nefedov et al.[40] have reanalyzed this data with the incorporation of only elastic scattering effects, and they find good agreement as to the qualitative form of the deviations from linearity expected at low θ. Pijolet and Hollinger[34] have also very recently analyzed similar Si2p(oxide)/Si2p(element) data using a simplified version of Eq. (17) which allows for an interface layer of intermediate composition between SiO_2 and Si; This analysis suggests that the transition region is rather abrupt and does not exceed $\sim$ 3 Å for an oxide film of $\sim$28 Å thickness. However, even this small a transition region also could account for some of the low-θ deviations, as was noted previously in the analysis by Hill et al.[19]. But in any case, the use of $\tau = t/\Lambda_e'$ values derived over the linear regions for the three thickest SiO_2 overlayers permitted deriving a Λ_e'(oxide) of 37±4 Å and, via the experimentally determined constant K (cf. Eqs. (1) and (9)), also a Λ_e(element) of 27±6 Å[19]. These values have subsequently been found to be accurate by other investigators[35,43,44]. Thus, provided that such data are tested via Eq. (9) and the appropriate high-θ range used, this type of analysis seems capable of providing accurate Λ_e' or Λ_e values (or, once Λ_e' is known, accurate t values).

E. Analysis of adsorbate overlayers at fractional monolayer coverage

In chemisorption studies, one is often dealing with fractional monolayer coverages of some adsorbate, and it is thus of interest to ask how accurate ARXPS is for both determining the coverage and also perhaps detecting whether an adsorbate has penetrated into the surface. Single-crystal effects are also often present in such studies, so that some allowance for them needs to be made also.

The example chosen here is from a recent study by Connelly et al.[33] of the very well characterized system c(2x2)S on Ni(001), for which an ordered half-monolayer of S atoms is present, occupying every other fourfold hole site on the Ni surface. Previous structural studies[45] indicate further that the S atoms are 1.3 Å above the first plane of Ni atoms, as will be discussed further in Section 5.E.

Polar scans of S2p(E_{kin} = 1317 eV), Ni2$p_{3/2}$(627 eV), and Ni3p(1413 eV) core-level intensities were made for two different azimuthal orientations

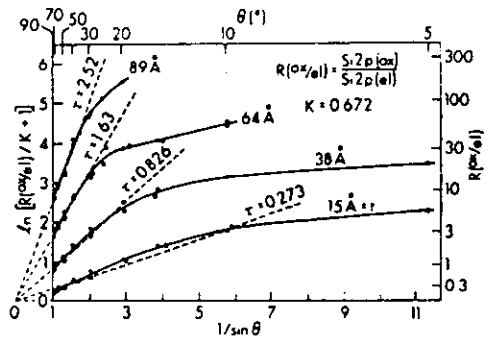

Fig. 16. Angle-resolved core-level intensity ratios from Si specimens with four different oxide overlayer thicknesses from 15Å to 89Å. The Si2p oxide/element ratio (cf. Fig. 7) has been plotted according to Eq. (9) so as to derive Λ_e(oxide) = t/τ. (From Hill et al., ref. (19).)

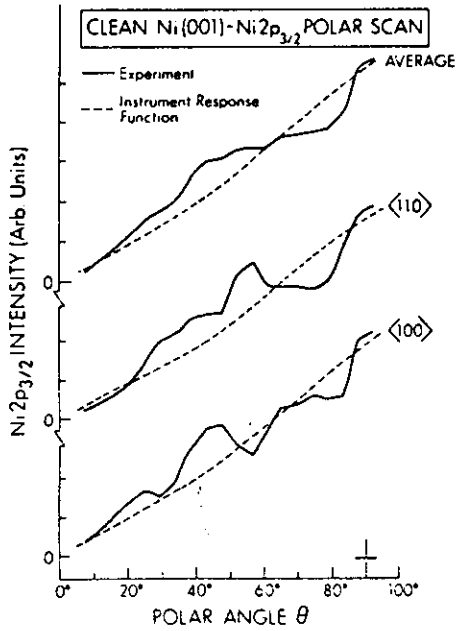

Fig. 17. Polar-scans of Ni2$p_{3/2}$ intensities above a (001) Ni surface. Shown are two scans along the symmetry-inequivalent azimuths [100] and [110], together with an average of these two scans. Before averaging strong diffraction features are evident. Also shown is the instrument response function (cf. Fig. 11). (From ref. (33).)

corresponding to [100] and [111] directions. (For $Ni2p_{3/2}$, it was important to include the intensity of the satellite at ~6 eV.) As expected, the Ni levels showed marked single-crystal channeling effects in their polar scans, but these were very nearly averaged out in a sum of the two scans at different azimuths. This is illustrated in Fig. 17, where the summed data for each Ni level also fit rather well the form expected for the Hewlett-Packard instrument response function (cf. Fig. 11).

The adsorbate/substrate ratios S2p/Ni3p and $S2p/Ni2p_{3/2}$ were calculated from Eq. (15), with all parameters being evaluated as accurately as possible for the specimen and experimental geometry utilized. This included utilizing the known coverage of s'/s = 0.5, theoretical photoelectric cross sections[25], and energy dependences of both λ_e in the substrate as given by $(E_k)^{1/2}$ and Ω_o as given by Fig. 12. The calculated curves are directly compared with experiment in Fig. 18, and there is very good agreement as to both the $1/\sin\theta$ form and the absolute magnitude of the ratio, even though the θ range covered is extremely broad (90°-7°). The two sets of data never disagree with theory by more than ~±10%. Theory is however above experiment at low θ for the $2p_{3/2}$ ratio, whereas it is below in the same region for the 3p ratio. This could be due to the much shorter mean free path for the lower energy $Ni2p_{3/2}$ peak, a fact which could lead to some low-θ inelastic attenuation in the overlayer that is not included in the model of Eq. (15). Nonetheless, these effects are not large, and, particularly if higher energy peaks are utilized, it appears that such azimuthally-summed measurements should permit rather accurate coverage measurements to be made, even in the presence of strong single crystal effects. In addition, differences in the forms of such ratio curves as a function of exposure or annealing could be useful in detecting adsorbate penetration into the substrate, as the degree of increase in an adsorbate/substrate ratio at low θ should decrease in the presence of any penetration. For too high adsorbate coverages, however, there could be concern as to the validity of the non-attenuating assumption for the overlayer[5].

F. Studies of more complex concentration profiles

In the category of more complex concentration profiles, we begin by considering a single-crystal specimen of LaB_6 with alternating layers of La atoms and B_6 octahedra perpendicular to the (001) surface (cf. Fig. 19(a)). When such a surface is polished, cleaned in situ by ion bombardment, and annealed to form a well-ordered system, the question arises as to whether La or B_6 layers will lie on the surface. Aono et al.[46] have studied this with ARXPS, measuring polar scans of both La and B core levels, as shown in Fig. 19(b) at two different azimuths. Although there are pronounced single-crystal channeling effects in the intensities

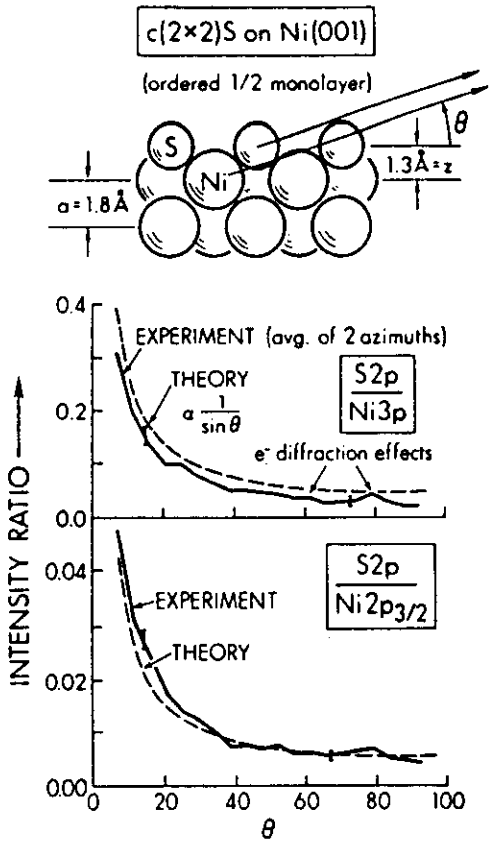

Fig. 18. Comparison of experiment and theory for the polar-angle dependence of an adsorbate/substrate intensity ratio for the very well defined overlayer of c(2x2)S on Ni(001). The $Ni2p_{3/2}$ and Ni3p intensities are averages of two azimuths (cf. Fig. 17). The theoretical curves are calculated according to Eq. (15) with no adjustable parameters. (From ref. (33).)

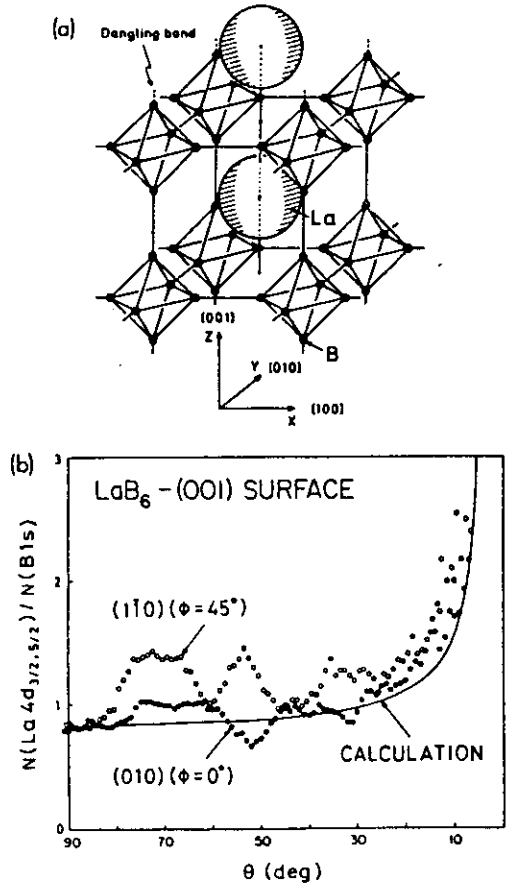

Fig. 19. The crystal structure of LaB_6 is shown in (a), together with the measured and calculated θ dependence of the La4d/B1s intensity ratio in (b). Two different azimuths are shown for the experimental results. (After Aono et al., ref. (46).)

of both peaks, it is nonetheless clear that the La relative intensity is enhanced at low θ. This system represents a straightforward application of Eq. (16) in which Λ_e does not vary with z, but it can be set up in two ways depending upon whether La atoms or B_6 moieties make up layer 1 (the surface layer). Aono and co-workers have carried out calculations of the $La4d_{3/2,5/2}$/B1s ratio in both ways and it is clear that the agreement with experiment is much better for a La surface layer. This observation via ARXPS has thus assisted in explaining the unusually low work function of LaB_6, and should be generally useful for ordered structures with layering of this type.

Binary metal alloys provide another example for which concentration profiles can be much more complex, with one component often segregating preferentially at the surface[47]. The concentration of this species may then monotonically decay into the bulk until it reaches the average bulk value, or it may in certain cases exhibit single-layer oscillations as it approaches the bulk value. Ion bombardment may, on the other hand, cause preferential depletion of one species at such a surface. As a qualitative illustration of such effects, Nefedov et al.[48] have studied permalloy with a composition of about $Fe_{0.2}Ni_{0.8}$. They compared the polar dependence of the Fe3p/Ni3p intensity ratio for an air-exposed film and for the same film after ion bombardment. Their results are shown in Fig. 20, where it is clear that Fe is surface segregated for the air-exposed film, but that very little segregation of either species is present after ion bombardment. Thus, it is possible to conclude that the ion bombardment has selectively removed Fe, perhaps leading to a slight enrichment of Ni at the surface.

Beyond such qualitatively useful conclusions concerning alloys, the question also arises as to whether the detailed $\rho_k(z)$ profile can be determined by analyzing such ARXPS data. Pijolet and Hollinger[34] have recently discussed this general problem from the point of view of using peak ratios $N_k(\theta)/N_{k'}(\theta)$ based upon Eq. (17). A simplex method is used to choose the best $\rho_k(z)$ and $\rho_{k'}(z)$ by minimizing the difference between the experimental and theoretical ratios. However, the ρ curves so derived are found to be extremely sensitive to the exact data points fit and the convergence criteria used, so that effectively, multiple solutions can result if quite arbitrary profiles are utilized. However, by incorporating physically realistic constraints on ρ_k and $\rho_{k'}$ as they are derived, much better results can be obtained. These constraints include limiting maximum and minimum values, and usually requiring a monotonically increasing or decreasing function of z. (The latter of course eliminates the possibility of seeing the oscillations in ρ(z) that are expected for certain systems.) An example of their results for a Cu/Ni alloy ion bombarded and annealed in UHV are shown in Fig. 21, together with the % Ni profile yielding the solid curve that

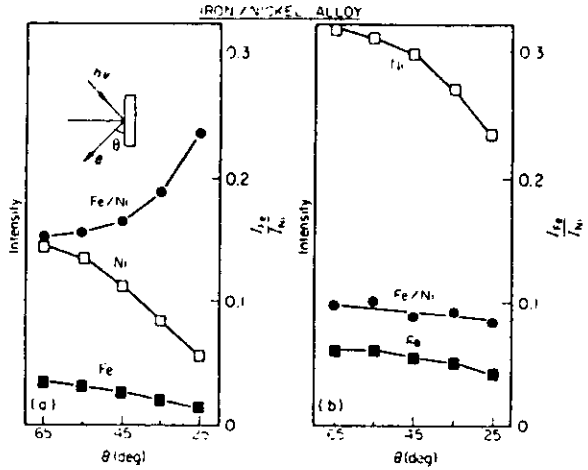

Fig. 20. The θ dependence of Fe3p and Ni3p core intensities for an Fe/Ni alloy before and after ion bombardment of the surface. Note particularly the marked change in the variation of the Fe/Ni ratio with bombardment. (After Nefedov et al., ref. (48).)

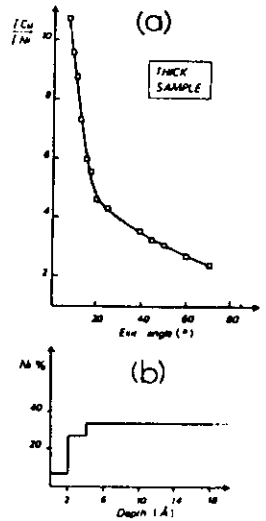

Fig. 21. Experimental $Cu2p_{3/2}$ / $Ni2p_{3/2}$ relative intensities from a Cu/Ni alloy are shown as a function of θ in (a). In (b), the Ni concentration profile as derived from these measurements using an analysis based on a simplified revision of Eq. (17) is presented. (From Pijolat and Hollinger, ref. (34).)

very well describes the $Cu2p_{3/2}/Ni2p_{3/2}$ ratio data. The profile also agrees qualitatively with that expected from theory. However, the layer-by-layer variation of ρ provides essentially a multiparameter fit, so that good agreement between theory and experiment does not assure meaningful theoretical numbers. Also, the inclusion of low-θ data down to ~6° could bring in errors due to roughness, refraction, or elastic scattering; it would be interesting to repeat the analysis for say θ ≳ 15-20° to check self-consistency. Nonetheless, this general idea for trying to derive arbitrary monotonic profiles is promising and well worth further investigation.

As a final and even more complex type of concentration distribution, mention should be made of systems that may exhibit concentration gradients both laterally along the surface as well as inward from the surface. Thus in general the density will be given by ρ(x,y,z). One important class of specimens exhibiting such character is supported heterogenous catalysts, in which active metal atoms may reside within pores in the support, or may coalesce under sintering to form very small metal particles along the surface of the support. This complex concentration distribution, together with the generally very rough character of the support surface, will make any sort of angle-resolved measurement rather difficult to interpret unambiguously, for reasons we have discussed previously. However, fixed-angle intensity measurements, together with specialized models incorporating some of the ideas in the patched overlayer of Eqs. (10) and (11), have been used to derive useful information concerning atomic migration and particle sizes on heterogenous catalysts, as discussed recently by Delgass and co-workers[49] and by Meisel et al.[50].

G. Studies of surface-specific electronic structure changes

(i) Surface core-level shifts. ARXPS has also been used to verify that core-level binding energies of atoms in the outermost layer of a material can be shifted relative to the bulk. This effect was first unambiguously observed by Citrin et al.[51], who used very high resolution (~ 0.25 eV) XPS to study the θ dependence of core levels in Au, Ag, and Cu. Some of their results are summarized in Fig. 22. For Ag and Cu there is little change with θ, but for Au, a shoulder grows in on the low-binding-energy side of the $4f_{7/2}$ peak for low θ. This is reminiscent of the discussion of the Si data in Fig. 8, and suggests a less-tightly-bound species near the surface. The Au data they have analyzed using a two-component model (i.e., a one-monolayer Au(surface) layer and Au(bulk)) with θ-dependent intensities given by Eqs. (4) and (5). This model is found to provide a self-consistent analysis of the data with a surface-to-bulk shift of 0.40 eV and a surface component localized entirely in the first atomic layer. Such

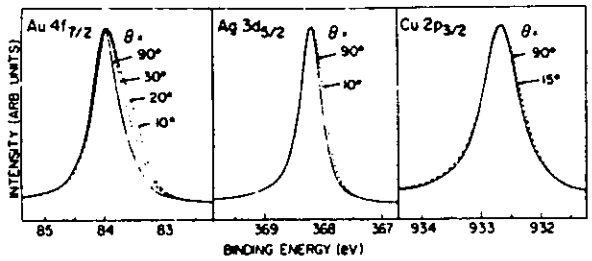

Fig. 22. The θ dependence of core line shapes from the noble metals Au, Ag, and Cu. For near-grazing emission, a shoulder is observed at lower binding energy for Au; This is interpreted as being due to a surface chemical shift of the $Au4f_{7/2}$ binding energy. (From Citrin and Wertheim, ref. (51).)

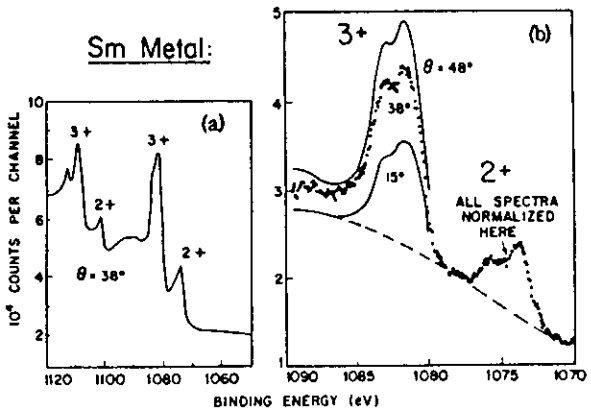

Fig. 23. The θ dependence of 3d core spectra from samarium metal. In (a), the overall 3d spectrum is shown, with both 3/2 and 5/2 regions exhibiting double peaks due to the presence of 3+ and 2+ configurations. In (b), the $3d_{5/2}$ region is shown at three different emission angles, with the 3+ peak being less important for grazing emission angles. (From Wertheim and Crecelius, ref. (53).)

surface-layer chemical shifts have subsequently been confirmed for other metals in higher-resolution synchrotron radiation studies[52]. The Si data of Fig. 8 also represents a similar observation of a surface-specific core shift, in this case thought to be due to hydride formation[20].

Thus, although both of these examples have strained the resolution of the technique to its limits, the ability to vary angle has provided an absolutely essential feature in arriving at the final conclusions.

(ii) Surface valence-state alterations. A further surface-specific effect that has been detected in ARXPS is a change in the average valency of certain rare earth species near the surface. Wertheim and Crecelius[53] first noted this effect for metallic Sm. This material is trivalent in the bulk, and exhibits corresponding multiplet splittings in both core and valence levels that can be used as fingerprints of this 3+ state. However, 2+ multiplets are also seen in the XPS spectra and they are found to increase in relative intensity as θ is decreased, as illustrated for the 3d core levels in Fig. 23. These data were successfully analyzed in terms of Eqs. (4) and (5), but with the added assumption that all Sm^{2+} was located in the first layer, although not all first-layer ions were Sm^{2+}.

(iii) Surface density-of-states changes. Inasmuch as the surface atoms of any material experience a different and usually lower coordination number in comparison to their bulk companions, it might be expected that the distribution of valence states in energy would also be different from the bulk. Such a difference, as measured by the density of states, has been predicted in numerous theoretical studies to occur on the surfaces of transition metals, where the general expectation is for a reduced d-band width as measured most accurately by the first moment of the d-band density of states[54].

One of the most convincing observations of such effects to date is based on ARXPS. Mehta and Fadley[55] studied clean polycrystalline surfaces of Cu and Ni, and for grazing emission found unambiguous narrowing of the second moment of the d band peaks by ∿ 19% and 21%, respectively. Experimental data for Cu are shown in Fig. 24. Calculations were performed to simulate these effects by taking theoretical densities of states as computed for each layer[56] $\rho(E)_j$, j = 1,2,3,... and summing them with allowance for inelastic scattering to yield a weighted density of states that should be seen in first order in the XPS measurement as:

$$\overline{\rho(E)} = \sum_{j=1}^{\infty} \rho(E)_j \exp(-z_j/\Lambda_e \sin\theta'). \qquad (21)$$

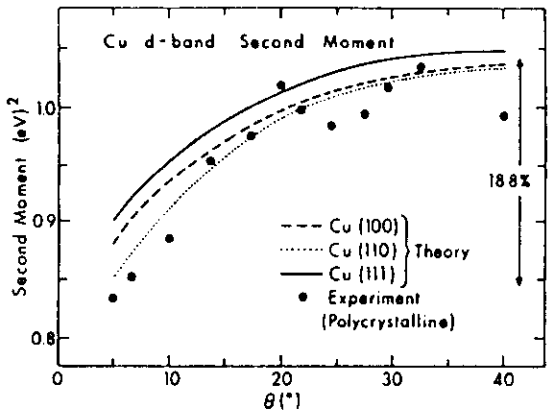

Fig. 24. Comparison of experimental and theoretical Cu 3d-band widths as a function of θ. The width is here measured using the second moment of the 3d intensity, although very similar results are obtained in using the FWHM. Theory is shown for the three lowest-index surfaces. (From Mehta and Fadley, ref. (55).)

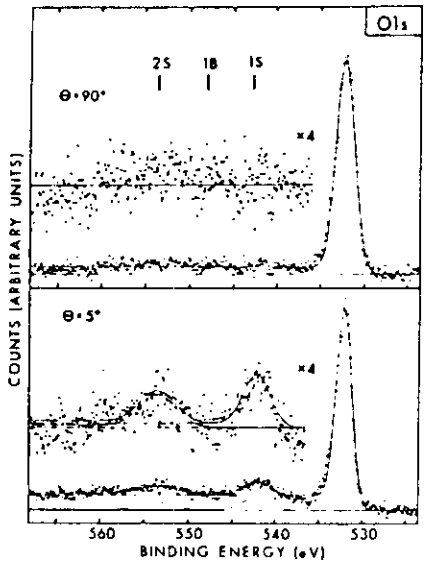

Fig. 25. Polar dependence of plasmon inelastic losses for O1s from oxygen adsorbed on a polycrystalline aluminum surface. The expected positions of bulk- and surface- plasmon loss peaks are also shown. (From Baird et al., ref. (57).)

Here, z_j is the depth of the jth layer and electron refraction has been allowed for in using θ' instead of θ. The curves calculated in this way for three low-index faces of Cu agree very well with the experimental curve, as shown in Fig. 24. The forms of the curves also agree for Ni, although theory predicts a larger effect than that observed. However, in view of the simple initial-state-only model used and the likely greater influence of many-electron effects in nickel d-band emission, the overall conclusion can certainly be made that these ARXPS results display surface d-band narrowing effects for both metals. The fact that decent agreement is obtained even at angles as low as θ=5° also suggests that surface roughness may not be a major problem for very carefully prepared surfaces (In this case, the metals were deposited in situ on ultra-smooth glass substrates.)

Citrin et al.[51] have subsequently used similar measurements on Au to isolate the surface and bulk components of the density of states, thus illustrating surface narrowing and other featural changes. The model used in analyzing this data is analogous to that described in Section 3.G(i) for surface core-level shifts. Their assumption that only the density of states of the first surface layer differs from that of the bulk deviates somewhat from theory, however[54,56], which suggests that the first 2-3 layers may differ. In any case, their results appear to be at least qualitatively correct.

Overall then, such ARXPS measurements have provided another type of information concerning the surface electronic structure of metals, and their application to other classes of materials should also be of interest.

(iv) Surface plasmon losses. A final effect that is of interest in connection with the enhanced surface sensitivity achievable at low θ is a change in the relative intensities of various inelastic loss processes. For example, for an atomically clean surface of aluminum (which exhibits well-defined surface- and bulk-plasmon excitations at different energies), it has been found by Baird et al.[57] that the surface plasmon losses are markedly enhanced in relative importance at low θ. The reason for this enhancement is that the surface- and bulk-plasmons are spatially orthogonal. Thus, because decreasing the angle of exit also decreases the mean depth of emission, the relative probability of exciting a surface plasmon is also increased at low exit angles. Comparisons of such data with theoretical calculations for a free electron metal furthermore yield good agreement with experimental relative intensities and further indicate that the creation of plasmons occurs by means of both extrinsic processes occuring after photoelectron excitation and intrinsic processes occuring during excitation[57]. A further feature of such angular-dependent loss measurements that is of interest in

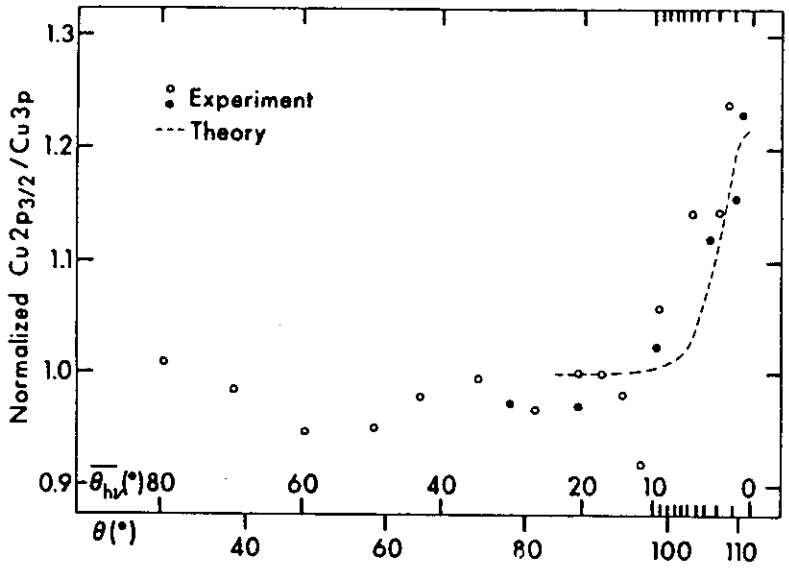

Fig. 26. Experimental and theoretical $Cu2p_{3/2}/Cu3p$ ratios for a smooth polycrystalline Cu specimen as a function of x-ray incidence angle $\theta_{h\nu}$. The $Cu2p_{3/2}$ intensity is enhanced in relative importance as $\theta_{h\nu}$ goes to zero due to its lower λ_e value and the reduced x-ray penetration depth. (M. Mehta and C. S. Fadley, unpublished results.)

a surface-chemical sense is that they may be useful in determining the locations of adsorbed molecules relative to a surface as noted by Baird et al.[57] and Bradshaw et al.[58]. Specifically, the O1s loss spectrum for an ~0.2 monolayer coverage of oxygen on aluminum exhibits only surface plasmon peaks at grazing electron exit, as shown in Fig. 25, thus suggesting that the oxygen has not penetrated significantly below the surface plane. Thus, the angular dependence of such adsorbate loss structures should provide useful complementary information concerning adsorption geometries and near-surface electronic structure.

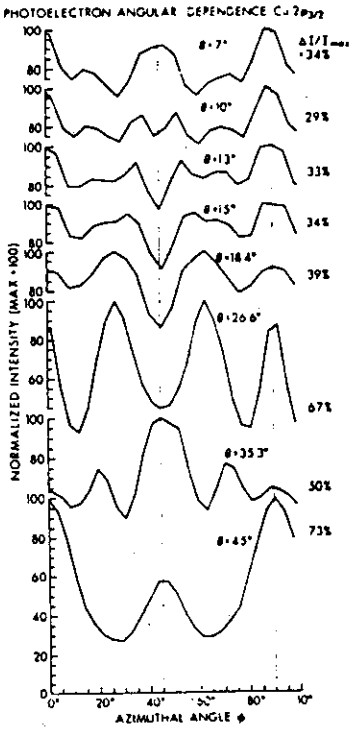

Fig. 27. Experimental azimuthal dependence of $Cu2p_{3/2}$ intensity above a Cu(001) surface for 8 different polar angles of emission. The data have been fourfold-averaged into one quadrant from a full 360° scan, but no mirror symmetrization about $\phi = 45°$ has been performed. Overall anisotropies $\Delta I/I_{max}$ are indicated as percentages. For certain θ values shown here, however (e.g., $\theta = 45°$), it has subsequently been determined that a non-linearity in the videcon multichannel detector used resulted in ~ 1.5X overestimates of the degree of an anisotropy. Compare the more accurate $\Delta I/I_{max}$ values at $\theta = 45°$ of Fig. 31. (From Kono et al., ref. (63).)

4. Surface Sensitivity Enhancement at Grazing X-ray Incidence Angles

A second mechanism producing enhanced surface sensitivity involves measurements carried out at very low x-ray incidence angles $\theta_{h\nu}$. For $\theta_{h\nu} \lesssim 1°$, it was first noted by Henke[21] that the mean x-ray penetration depth in a typical XPS experiment (which is a very large 10^3-10^5 Å for $\theta_{h\nu} >> 1°$) decreases markedly to values of the same order as the electron attenuation length λ_e. This further suggests that surface-atom signals will be enhanced in relative intensity at low $\theta_{h\nu}$, as was first demonstrated by Mehta and Fadley[59]. The reason for this decrease in x-ray penetration depth is the onset of significant refraction such that $\theta_{h\nu}' << \theta_{h\nu}$ (cf. Fig. 9) at the solid surface. The interactions of typical XPS x-rays with a homogeneous medium are furthermore well described by a macroscopic classical treatment,[21] and detailed expressions for predicting penetration depths and expected surface sensitivity enhancements in terms of the material optical constants and other parameters have been presented elsewhere.[5,21,59]

As a recent example indicating the surface sensitivity enhancement possible at low $\theta_{h\nu}$, Fig. 26 shows data obtained from a clean polycrystalline Cu surface for which the $Cu2p_{3/2}/Cu3p$ ratio was measured as a function of the mean x-ray incidence angle $\overline{\theta}_{h\nu}$[60]. Because the kinetic energy of the $Cu2p_{3/2}$ peak (549 eV) is much lower than that of the Cu3p peak (1406 eV), its mean free path will be significantly lower. Thus, the mean depth of $2p_{3/2}$ emission will be less than that of 3p emission under normal circumstances of x-ray incidence, and any significant reduction in the x-ray penetration depth at low $\theta_{h\nu}$ will act preferentially to turn off more of the 3p signal. Therefore, the ~25% increase in the $Cu2p_{3/2}/Cu3p$ ratio noted for $\overline{\theta}_{h\nu} \gtrsim 0°$ is a clear indication of surface sensitivity enhancement. There is also good agreement between experiment and theoretical calculations including both refraction and reflection effects, as also shown in Fig. 26. Note the very sharp onset of the low-$\theta_{h\nu}$ enhancement over a region of only a few degrees near $\theta_{h\nu} = 0°$. More pronounced effects have also been noted in the Cls/Au4f ratio for Au with a carbonaceous overlayer[59], and in the Si2p(oxide)/Si2p(element) ratio for silicon with varying oxide overlayer thicknesses.[61] Also, the known optical properties of several solids at XPS energies of ~1.5 keV have been used to predict that such phenomena should be of very general occurrence.[5]

It should be noted in connection with such grazing-incidence studies, however, that surface roughness effects can be extremely important in any attempt at quantitatively analyzing such data.[61] This is due to the very small incidence angles involved, so that if the true microsopic incidence angle $\theta_{h\nu}^t$ deviates by even ~0.1° from the macroscopically measureable $\theta_{h\nu}$, a significant change occurs

in the degree of refraction and reflection. Thus, surface preparation and accurate angle measurement are both very critical. Further practical problems are that the x-ray source ought to have a very well defined direction of incidence ($\Delta\theta_{h\nu} \lesssim 1°$ in Fig. 9) and that surface shading by any roughness present will generally act to much diminish absolute photoelectron intensities at low $\theta_{h\nu}$. Thus, grazing-x-ray-incidence surface enhancements may serve as a useful complement to those at grazing electron emission, but the measurement and interpretation of the former data may not be as straightforward.

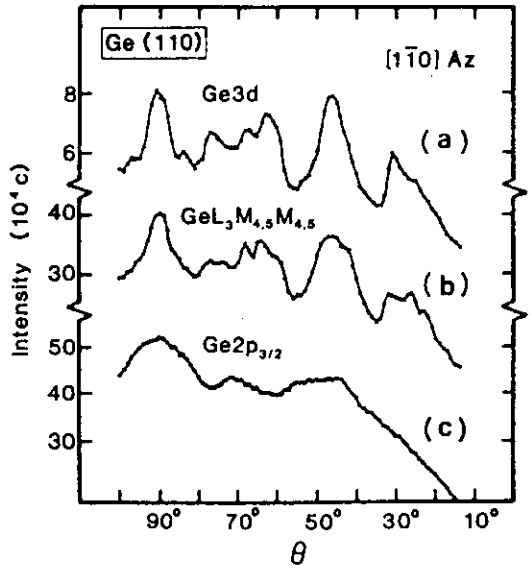

Fig. 28. Experimental polar dependence of Ge XPS and Auger intensities above a Ge(110) surface for θ scans in a [1$\bar{1}$0] azimuth. Ge3d and $Ge2p_{3/2}$ XPS intensities are shown together with the Ge $L_3M_{4,5}M_{4,5}$ Auger intensity. No allowance has been made for the instrument response function. (From Owari et al., ref. (64).)

5. Core-Level Emission from Single Crystals: X-ray Photoelectron Diffraction(XPD)

A. Introduction

In this section, we begin the consideration of effects observed in angle-resolved x-ray photoemission studies of highly-ordered single-crystal specimens. Here, emission from highly-localized, atomic-like core levels will be discussed; in Section 6 following, the more complex case of emission from delocalized valence levels will be considered. In both situations, a consideration of diffraction phenomena associated with the wave character of the emitted photoelectrons will prove essential for understanding the observed angular distributions. It is thus useful to immediately introduce the appropriate non-relativistic relationship between photoelectron wavelength λ_e and kinetic energy E_{kin}:

$$\lambda_e = h/[2mE_{kin}]^{1/2}, \quad (22)$$

where h = Planck's constant and m = the electron mass. In convenient units, this reduces to approximately

$$\lambda_e(\text{in } \mathring{A}) = [150/E_{kin}(\text{in eV})]^{1/2}. \quad (23)$$

Thus the relevant wavelengths over the typical XPS range of energies of ~500-1500 will be from 0.55 Å at 500 eV to 0.32 Å at 1500 eV. The magnitude of the associated electron wave vector $\vec{k}$ is in turn given by $k = 2\pi/\lambda_e$, and $\hat{k} = \vec{k}/k$.

In order to qualitatively introduce the different types of effects seen in such x-ray photoelectron diffraction (XPD) experiments, some typical experimental data are shown in Figs. 27-30[62-64]. These are illustrative of the various types of data which can be obtained, in that Figs. 27 and 28 both represent emission from core-levels in the single-crystal substrate (Cu with (001) orientation and Ge with (110) orientation, respectively), whereas Figs. 29 and 30 represent emission from species adsorbed on such a substrate (c(2x2)CO on Ni(001) and c(2x2)O on Cu(001), respectively. Also, two of the figures (27 and 30) represent azimuthal scans (cf. Fig. 2) whereas the other two (28 and 29) show polar scans.

From these figures, one can directly draw several useful qualitative conclusions: There are pronounced anisotropies in all of these photoelectron angular distributions. If the degree of anisotropy is measured as $(I_{max}-I_{min})/I_{max} = \Delta I/I_{max}$, we see that the values vary from as large as 73% for $Cu2p_{3/2}$ substrate emission in Fig. 27 to as small as 6% for O1s adsorbate emission at large θ values in Fig. 30. There are also some rather narrow features in these angular distributions, with widths as small as ~ 4-5°, and this indicates the possible importance of having adequate angular resolution (as discussed further below). Not surprisingly, the patterns seen exhibit certain symmetries of the underlying substrate: for example, the azimuthal data of Figs. 27 and 30 for a Cu(001)

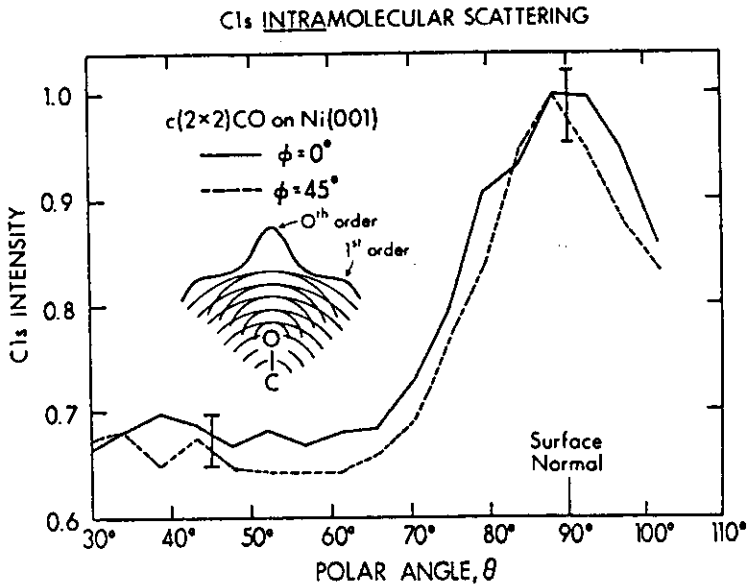

Fig. 29. Experimental polar dependence of the C1s intensity for a c(2x2) overlayer of CO on a Ni(001) surface. The data have been obtained in two symmetry-inequivalent azimuths. Also shown is a schematic illustration of the intramolecular scattering and diffraction producing such effects. (From Petersson et al., ref. (62) and Orders and Fadley, ref. (81).)

surface with C_{4v} symmetry exhibit near mirror symmetry about a [110] azimuth for ϕ = 45°, a point we will amplify on below. The strongest substrate diffraction features are also most often seen along high-symmetry azimuths as well, and this suggests the possible use of such features for determining crystal orientations. Finally, if the substrate angular distributions of Fig. 28 are considered, it is clear that the lower-energy photoelectron peaks exhibit broader features than those at higher energy: specifically, the $Ge2p_{3/2}$ angular distribution at 270 eV has less fine structure than that of Ge3d at 1457 eV. This last observation is a straightforward consequence of the change in de Broglie wavelength with energy, with shorter wavelengths at higher energies being capable of producing sharper diffraction features due to interference effects.

The previous point concerning the desirability of high angular resolution is further illustrated in Fig. 31, where experimental $Cu2p_{3/2}$ azimuthal data from Cu(001) at a polar emission angle of 45° is shown for two different analyzer angular acceptances: cones with half angles of 4.5° and 1.5°. The angle steps used in accumulating the data were $\Delta\phi$ = 1.0° for both cases. It is clear that the ±1.5° aperture yields data with considerably more fine structure, including some features of only a few degrees in width. Although most of these features can also be seen in the ±4.5° data, they are much easier to resolve in the ±1.5 curves. Thus the optimum use of XPD in deriving structural information will in many cases require instrumental angular resolutions of approximately 1-2°.

The azimuthal data of Figs. 27 and 30 further illustrate some important points concerning data analysis. The raw data of Fig. 30 for O1s emission from c(2x2)O on Cu(001), which is shown as dashed curves, has been obtained by scanning over a full 360° in azimuth. Thus, in view of the C_{4v} symmetry of the surface, there is redundancy in the data that can be used to average out noise and to check for the reliability of various features. One useful method is to fourfold average such data by adding the points at ϕ, ϕ+90°, ϕ+180°, and ϕ+270°, thus partially accounting for the known symmetry associated with the surface; in general, this averaging reduces the anisotropy $\Delta I/I_{max}$. Subtracting off the minimum intensity and replotting then yields the "flower" patterns shown as solid curves. These can in turn be compared with the raw data to be sure that all features present in the fourfold-averaged data are consistent with similar features in each quadrant of the raw data. Any misalignment of the azimuthal rotation axis with respect to the [001] surface normal also becomes very evident in such comparisons. Finally, since the symmetry operations of mirror reflection across ϕ=0°, 45°, etc. have not been included in the fourfold averaging, the presence or absence of such mirror symmetry can be used to judge feature accuracy and overall statistical reliability. For example, in Fig. 27, such fourfold-averaged data for $Cu2p_{3/2}$

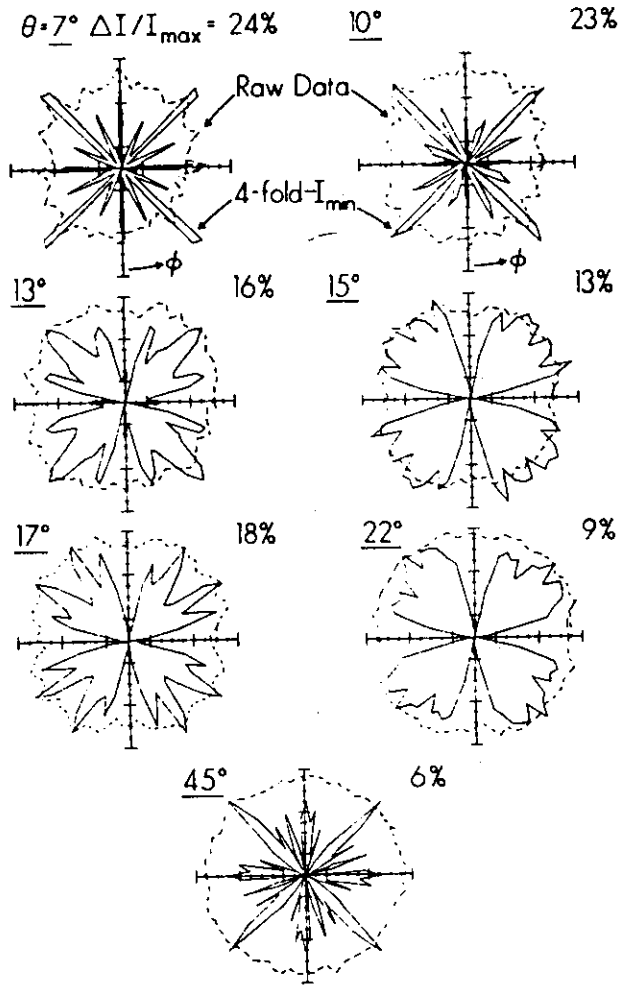

Fig. 30. Experimental azimuthal dependence of the O1s intensity for a c(2x2) overlayer of oxygen on a Cu(001) surface. Seven different polar angles of emission are shown. Both the raw data of a full 360° scan and fourfold-averaged data from which the minimum intensity has been subtracted are shown. The overall anisotropies $\Delta I/I_{max}$ are also indicated for each set of fourfold-averaged data. (From Kono et al., ref. (63).)

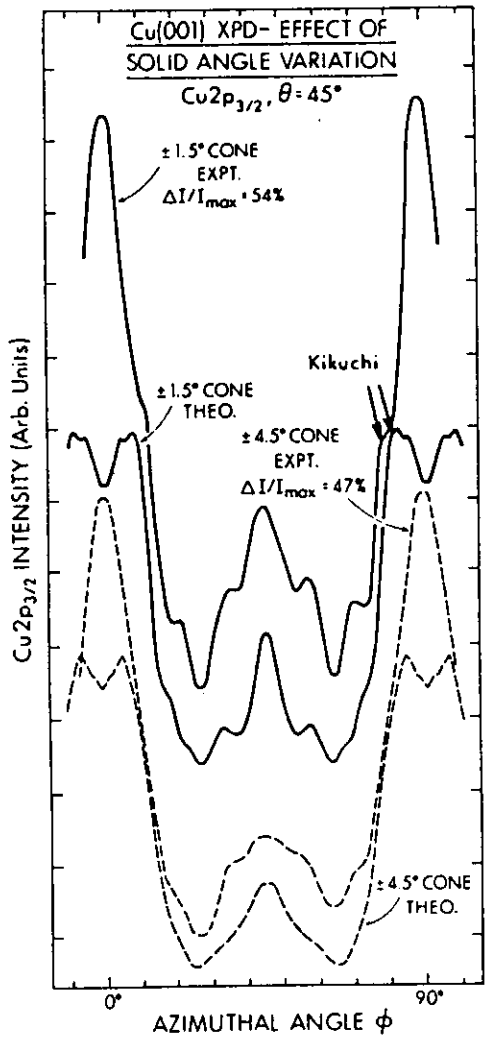

Fig. 31. Effect of analyzer solid angle variation on the experimental and theoretical azimuthal dependences of the $Cu2p_{3/2}$ intensity observed at 45° above a Cu(001) surface. Curves are shown for both a ±1.5° cone of acceptance solid angle and a ±4.5° cone of acceptance. The theoretical curves are based on the single-scattering cluster model. (R. C. White, B. Sinkovic, P. J. Orders, and C. S. Fadley, unpublished results.)

emission from Cu(001) is plotted in Cartesian form and is found to be very close to mirror symmetric about $\phi = 45°$. Other forms of azimuthal data averaging would be appropriate for surfaces with different symmetry (as a three-fold (111) surface or the stepped surfaces to be discussed in Sec. 5.E.), but in general it seems to be very useful to obtain the fullest angle scans possible to enable carrying out such analyses. Similarly, doing symmetry-equivalent polar scans (e.g., at $\phi = 0°$, 90°, 180°, 270° for a fourfold surface) and averaging these to check orientational accuracy and reduce spurious intensity variations is also very useful.

It is also worthwhile to note here that the typical mean free paths for inelastic scattering in XPS of ~10-30 Å imply that all of the features seen in Figures 27-30 must be associated with atomic order very near the surface. In fact, we have found in general that the type of surface pre-treatment utilized (for example, as to times and temperatures for ion bombardment and annealing) can have a dramatic effect on the degree of anisotropy found, even when simultaneous observation with low energy electron diffraction (LEED) shows very little visual difference in the sharpness of a pattern for different pre-treatment procedures. Thus, such XPS measurements seem to be very sensitive and quantitative indicators of the degree of near-surface order.

Before proceeding to a more quantitative discussion of these effects, we consider a few examples of how such x-ray photoelectron diffraction patterns can be used in more or less a fingerprint fashion to derive very useful information. First, the fact that substrate photoelectron emission along low-index directions in the crystal is generally associated with pronounced peaks in the XPD pattern can be used to carry out very precise crystal orientations in situ. (This peaking along low-index directions can be qualitatively explained in terms of Kikuchi bands associated with different sets of low-index planes[65], as discussed in more detail in Section 5.B.) For example, in our laboratory, the polar- and azimuthal-orientations of (001)-metal crystals are routinely determined to within ±0.5° by using a combination of polar scans through the [001] surface normal and azimuthal scans through a series of <110> directions at 45° with respect to the normal. For single crystals containing more than one type of atom, a second type of information concerns the nature of the crystal site in which a given substrate atom is sitting: for example, is it in well-defined lattice sites, has it been interstitially incorporated, or has it been randomly incorporated with respect to the other atoms of the lattice? This use of XPD was first made for a Au/Ag alloy by Fadley and Bergstrom[3]. Some more recent XPD data obtained by Thomas and co-workers[66] from a single crystal of the mineral muscovite are shown in Figure 32. Here, polar scans of different peak intensity ratios are shown. These have been analyzed by noting that photoelectrons arising from two atoms occupying

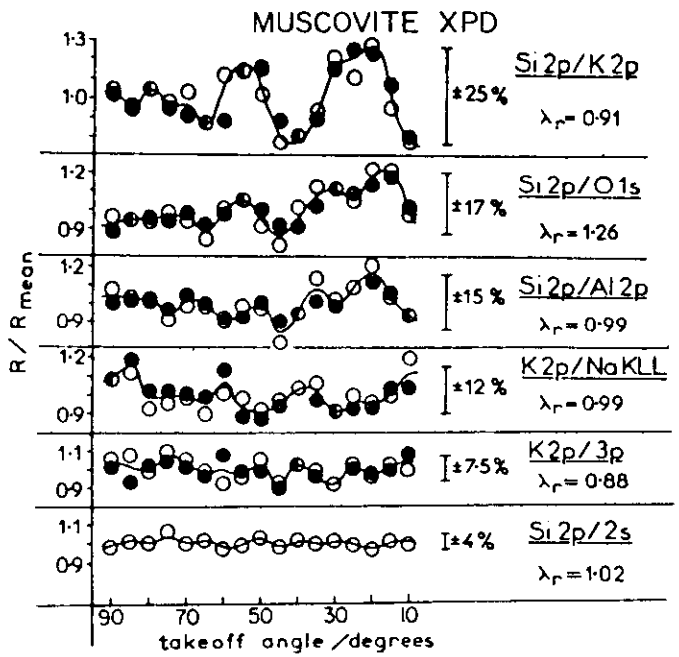

Fig. 32. Experimental polar dependence of normalized core intensity ratios for different peaks resulting from a single crystal of the mineral muscovite ($K(Al_2)(Si_3Al)O_{10}(OH)_2$). The full range of excursion is indicated as a percentage, and λ_r denotes the ratio of de Broglie wavelengths of the two peaks involved in a given ratio. (From Adams, Evans, and Thomas, ref. (66).)

exactly the same type(s) of lattice site(s) in the crystal should show exactly the same XPD pattern, as long as their de Broglie wavelengths are not different by more than ∿30%; thus, their normalized ratio should be very near unity regardless of polar angle. This is trivially the case for the K2p/K3p and Si2p/Si2s ratios arising in a single atom. By contrast, photoelectrons arising from atoms with very different sites should exhibit the greatest excursions from unity, as for the ∿±25% deviations in the Si2p/K2p ratio; this is consistent with the known structure of this mineral. The reduced value of the Si2p/Al2p excursions of ±15% (as compared, for example to Si2p/K2p) is furthermore suggestive of some Al in stoichiometric excess of that needed to occupy normal octahedral sites going into tetrahedral sites that are predominantly Si. As a second example of site-type determination, Fig. 33 shows polar-scan data obtained by Nihei et al.[67] for a Au overlayer of ∿85 Å thickness grown onto a (110) surface of GaSb. With annealing at 400°C only, the Au4f XPD pattern is relatively featureless, suggesting an amorphous overlayer, whereas both the Ga3d and Sb4d patterns exhibit considerable fine structure. After annealing at 540°C, however, the Au4f pattern becomes very nearly identical to the Ga3d pattern; as these two peaks are furthermore very close in kinetic energy, it is thus suggested that Au has preferentially displaced Ga in the GaSb lattice. This kind of atom-specific order and site information would be difficult to obtain in any other way.

As a final introductory comment, we note that Liebsch[68] first pointed out from a theoretical point of view how adsorbate core-level photoelectron diffraction might be used to determine surface structural information. This work involved multiple-scattering theory for low energies as appropriate to an ARUPS experiment.

B. The single-scattering cluster (SSC) model

In discussing more quantitatively such XPD effects, it is necessary to introduce a more detailed model of the scattering and interference phenomena that are expected to occur for photoelectrons in the ∿500-1500 eV energy regime. Such a model can be formulated at varying levels of complexity from a straightforward single-scattering or kinematical approach[62,63,69] to more complex dynamical treatments incorporating some degree of multiple scattering[68,70,71]. Fortunately, we have found that a very simple single-scattering model as applied over a finite cluster of atoms appears to very well describe most of the features in XPD[62,63,69], and it is thus this approach that will be discussed below.

The essential elements of this single-scattering cluster (SSC) model are shown schematically in Fig. 34. The basic assumptions are essentially identical to those used in describing extended x-ray absorption fine structure (EXAFS)[72,73] and a similar model has also been applied (although rather unsuccessfully) to angle-

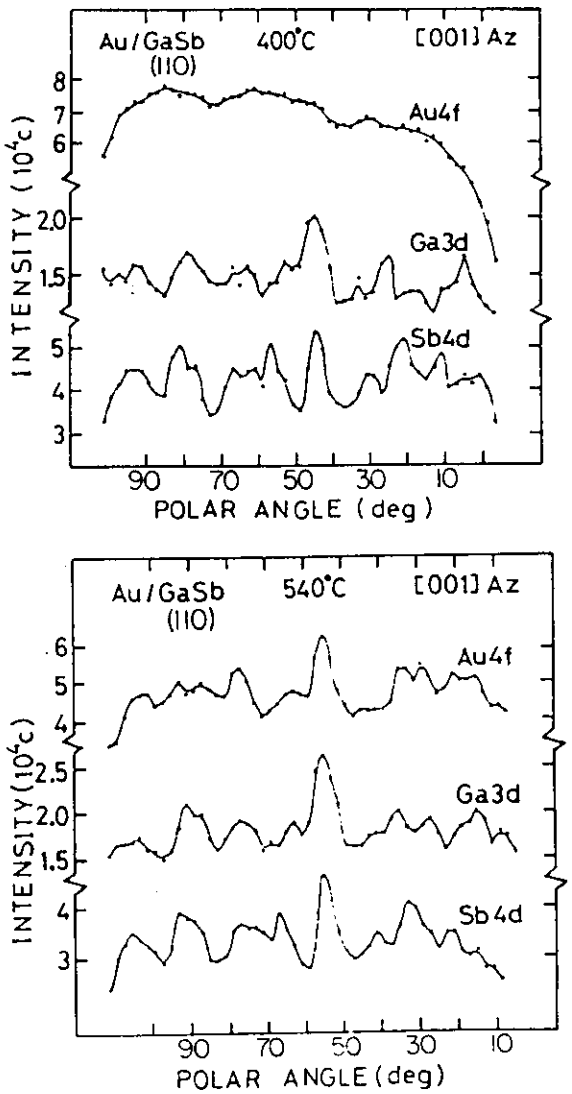

Fig. 33. Experimental polar dependence of the Au4f, Ga3d, and Sb4d peaks resulting from a Au overlayer of approximately 85Å thickness on a GaSb(110) surface. Scanning was in a [001] azimuth, and results for two different annealing temperatures of 400° and 540° are shown. Note the strong similarity of the Au4f and Ga3d curves after the higher temperature anneal. (From Koshizaki et al., ref. (67).)

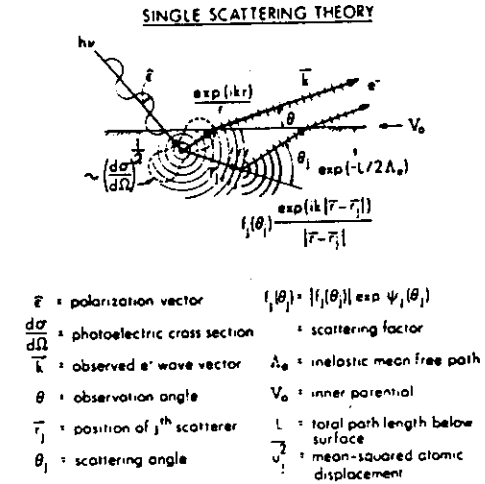

Fig. 34. Schematic illustration of the assumptions used in the single scattering cluster (SSC) model, with various important quantities defined.

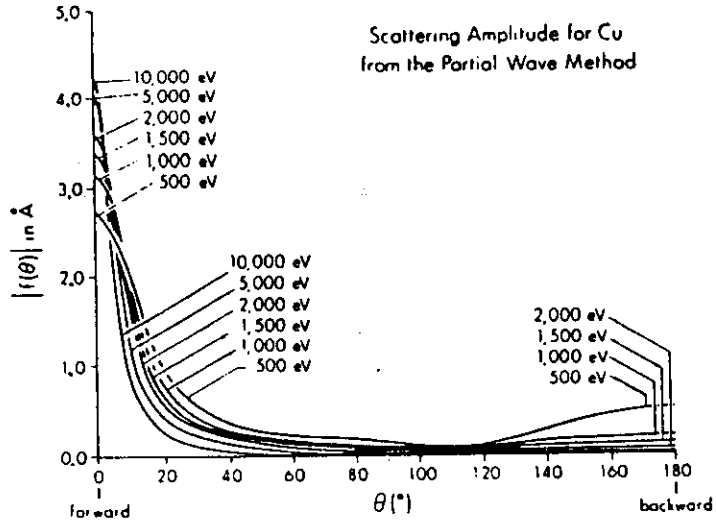

Fig. 35. The magnitude of the atomic scattering factor $|f(\theta)|$ for Cu as a function of scattering angle θ for various electron kinetic energies from 500 to 10,000 eV. Note the enhanced forward peaking as energy increases, and the concomitant decrease in the importance of any backscattering. (From Thompson, ref. (80).)

resolved Auger emission at very low energies of $\lesssim$100 eV[74]. The SSC model as appropriate to XPD is discussed in more detail elsewhere[62,63], so that only the essential assumptions and mathematical results will be outlined here.

Radiation with polarization $\hat{\varepsilon}$ is incident on some atom in the cluster, from which it ejects a core-level photoelectron. (In Fig. 34, the emitting atom is shown near the surface, but it could as well be any atom in the substrate.) The problem is then to describe the single scattering of this wave from all other atoms j in the cluster, keeping track of the phase shifts introduced by both the scattering and path length differences and finally to sum the wave amplitudes so produced to yield the total photoelectron amplitude. Squaring this amplitude then yields the intensity expected in a given emission direction, as denoted by the wave vector $\vec{k}$. That is, if $\phi_o(\vec{r},\vec{k})$ is the photoelectron wave at $\vec{r}$ as emitted directly into direction $\vec{k}$ and $\phi(\vec{r},\vec{r}_j\rightarrow\vec{k})$ is the wave resulting from initial ϕ_o emission toward a scatterer j at $\vec{r}_j$ and then subsequent scattering so as to emerge from the surface in the direction of $\vec{k}$, the overall wave amplitude will be given by

$$\psi(\vec{r},\vec{k}) = \phi_o(\vec{r},\vec{k}) + \sum_j \phi_j(\vec{r},\vec{r}_j\rightarrow\vec{k}) \qquad (24)$$

and the photoelectron intensity by

$$I(\vec{k}) \propto |\psi(\vec{r},\vec{k})|^2 \quad . \qquad (25)$$

Because the detector is situated at essentially $\vec{r} = \infty$ along $\vec{k}$, all of the waves in (24) can finally be taken to have the limiting spherical forms $\phi_o \propto \exp(ikr)/r$ or $\phi_j \propto \exp(ik|\vec{r}-\vec{r}_j|)/|\vec{r}-\vec{r}_j|$, although the actual amplitudes of each type in a given direction will be modulated by the photoexcitation matrix element and, for the ϕ_j's, also the scattering cross section. It is further assumed that the portion of ϕ_o which passes to the scatterer j to produce ϕ_j also decays in amplitude according to a spherical wave assumption, or as $1/r_j$. If the scattering angle is θ_j, the overall path length difference between ϕ_o and ϕ_j is then $r_j(1-\cos\theta_j)$.

The directional modulation of the initial photoelectron wave ϕ_o would most accurately be treated by considering both the $\ell+1$ and $\ell-1$ components produced in a dipole excitation from an $n\ell$ subshell, and determining the matrix element involved[70-72]. Fujikawa, for example, has recently discussed this approach[71]. For the special case of ns emission, however, this reduces simply to an $\hat{\varepsilon}\cdot\hat{k}$ dependence[25], and it is this form that has been used in most prior XPD analyses[63,69]. Since the differential photoelectric cross section $d\sigma_{n\ell}(\hat{\varepsilon},\hat{k})/d\Omega$ is proportional to intensity rather than amplitude, another approximation would be to use a ϕ_o modulation of $[d\sigma_{n\ell}(\hat{\varepsilon},\hat{k})/d\Omega]^{1/2}$ [64]. Although this is not strictly correct and does not account for possible sign changes in the matrix element with direction due to the photoelectron parity[75], it is probably an adequate approximation for XPD in which the electron scattering process will be seen to select out $\vec{r}_j$ choices very nearly parallel to $\vec{k}$; that is, for the range of $\vec{r}_j$ directions near the $\vec{k}$ direction that produce significant scattering, the matrix element varies little, so that a very precise description of it is not required. In fact, predicted XPD patterns have not been found to be very sensitive to the exact way in which the matrix-element modulation is included, particularly as regards averaging over $\hat{\varepsilon}$ in an unpolarized source[62,63]. We shall thus use the simple $\hat{\varepsilon}\cdot\hat{k}$ form in what follows.

The electron-atom scattering that produces ϕ_j is assumed to be adequately described by a complex scattering factor

$$f_j(\theta_j) = |f_j(\theta_j)|\exp[i\psi_j(\theta_j)], \qquad (26)$$

where $\psi_j(\theta_j)$ is the phase shift associated with the scattering. The scattered wave ϕ_j is thus proportional to $f_j(\theta_j)\exp ik|\vec{r}-\vec{r}_j|/|\vec{r}-\vec{r}_j|$, with an overall phase shift relative to ϕ_o of $kr_j(1-\cos\theta_j) + \psi_j(\theta_j)$ that is due to both path length difference and scattering. The use of this form for ϕ_j implicitly assumes that the portion of ϕ_o incident on the jth scatterer has sufficiently low curvature compared to the scattering potential dimensions to be treated as a plane wave. This is the so-called "small-atom" approximation[76], and it should be fully adequate in XPD for all but perhaps the nearest-neighbor atoms to the emitter. Even for such nearest-neighbor atoms, the only effect of inclusion of ϕ_o curvature will probably be to somewhat reduce the amplitudes of certain forward-scattering peaks in $I(\vec{k})$ in comparison to those predicted with the use of Eq. (26)[77], so that its neglect should not be serious. A further important point here is that, as energy is increased, the region of the potential well that is effective in the scattering is reduced in diameter, so that the small-atom approximation should because of this be more valid than prior criteria[76] might indicate.

The scattering factor $f_j(\theta_j)$ is most accurately determined by applying the partial-wave method to a suitable spherically symmetric-scattering potential for each atomic type in the cluster. The number of partial-wave phase shifts needed goes up with energy, and for a typical scattering potential of effective radius 1.5 Å, would be $\gtrsim$ 8 for E_{kin} = 500 eV and $\gtrsim$ 24 for 1500 eV. Tabulations of free-atom scattering factors at energies spanning the XPS regime exist[79]. Alternatively, scattering potentials more appropriate to a cluster of atoms with overlapping charge densities and potentials can be constructed via the muffin-tin model employed, for example, in LEED[41,42]. The free-atom f_j's generally are larger in magnitude than their muffin-tin counterparts due to their neglect of charge and potential overlap[62,63]. Both types of f_j's have been employed in XPD calculations, and they do not yield significantly different $I(\vec{k})$ curves, although

the use of free atom f_j's might be expected to predict slightly higher peak intensities due to their larger amplitudes. In the limit of very high energy, the use of the first Born approximation[78] for determining scattering factors might also be expected to be adequate. However, recent studies by Goldberg, Thompson et al. have shown that the Born approximation is not sufficiently accurate for XPD calculations at $\lesssim$5 keV[63,80].

Some typical scattering factor amplitudes and phase shifts for Cu are shown in Figs. 35 and 36. These curves and other available data[79] show that, over the typical energies in XPS of ~500-1500 eV, the amplitude $|f_j(\theta_j)|$ is very strongly peaked in the forward direction or near $\theta_j = 0°$, with a FWHM of only ~10-30°. This forward peaking is even more pronounced at higher energies, as illustrated in Fig. 35. The only other appreciable scattering strength occurs near $\theta_j = 180°$, but this is down by roughly an order of magnitude in comparison to the forward scattering peak. At higher energies, the back scattering peak is reduced even further, essentially disappearing at 10,000 eV. Considering the phase shifts in Figure 36 and other available data[79] also permits concluding that for XPD, ψ_j is rather small ($\lesssim$30-50°) for the θ_j region in which $|f_j|$ is large. Thus, for electron elastic scattering in XPD from atoms of low- to moderate- atomic number, the scattered waves ϕ_j are expected to be significant only for θ_j rather near zero, and in this case the scattering phase shift will also be rather small. (The optical theorem prevents ψ_j from being exactly zero unless the total scattering cross section is also zero[78].) For substrate-atom emission from well below the surface, the condition of near-forward scattering from neighbors above is geometrically possible for emission into a large number of directions $\vec{k}$ above the surface. However, for adsorbates or near-surface substrate atoms, observation at special emission directions may be necessary to see significant XPD. This is why, for example, most of the polar angles θ in Fig. 30 are near-grazing with respect to the surface. It also explains why the anisotropy in Fig. 30 falls off as the polar angle is increased away from the surface, becoming almost undetectable at θ = 45°.

The effects of inelastic scattering on wave amplitudes during propagation below the surface must also be included. Intensity falls off as $\exp(-L/\Lambda_e)$, where L is an arbitrary path length, so that amplitude is expected to fall off as the square root of this or $\exp(-L/2\Lambda_e) \equiv \exp(-\gamma L)$. Thus, $\gamma = 1/2\Lambda_e$, although γ values up to ~2-3 times this have been suggested in prior EXAFS[72] and Auger[74] analyses. Each wave ϕ_0 or ϕ_j can thus be multiplied by such a factor involving an L value which includes the total path length below some surface cutoff point. This surface cutoff is usually chosen to be the substrate surface as defined by hard-sphere atoms[62,63], although the exact choice is not found to influence the XPD patterns

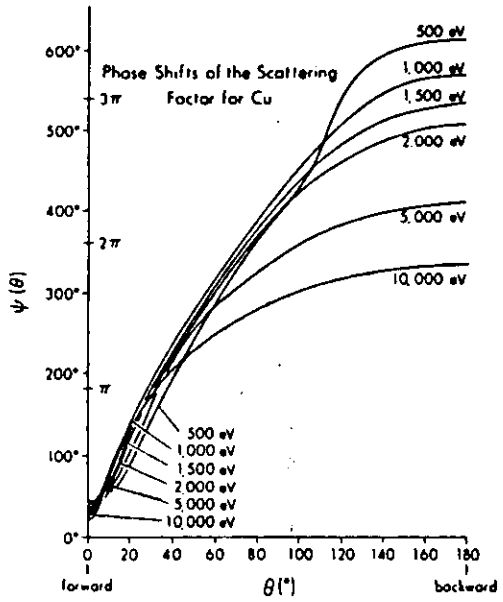

Fig. 36. The phase shift $\psi(\theta)$ for Cu as a function of scattering angle θ for various electron kinetic energies from 500 to 10,000 eV. (From Thompson, ref. (80).)

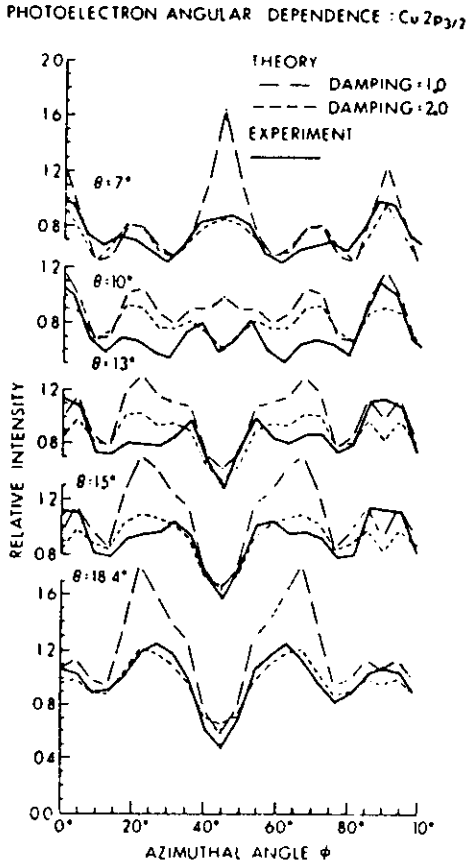

Fig. 37. Comparison of experiment and single-scattering cluster (SSC) theory for the azimuthal dependence of $Cu2p_{3/2}$ emission from Cu(001) at various polar angles between 7° and 18.4°. The notation damping = 1.0 refers to the use of $|f_j(\theta)_j|$ values with no empirical reduction factor, whereas damping = 2.0 refers to the use of values reduced by ½ to optimize agreement with experiment. Note that the only significant changes produced by the use of such damping are for two fine structure features near $\phi = 45°$ and for $\theta = 7°$ and 10°. (From Kono et al., ref. (63).)

significantly. Λ_e values can be taken from prior experimental or theoretical tabulations, but it is found that this choice also is not critical: for example, Λ_e for Cu has been varied by ~±25% without changing the substrate XPD patterns significantly[62,63].

Vibrational attenuation of interference effects is furthermore potentially important, and can be included in a standard way by multiplying each ϕ_j by its associated temperature-dependent Debye-Waller factor:

$$W_j(T) = \exp[-\Delta k^2 \overline{U_j^2}(T)] = \exp[-2k^2(1-\cos\theta_j)\overline{U_j^2}(T)] \quad (27)$$

where Δk is the magnitude of the change in wave vector produced by the scattering, and $\overline{U_j^2}(T)$ is the temperature-dependent one-dimensional mean-squared vibrational displacement of atom j with respect to the emitter. At this level of approximation, $\overline{U_j^2}$ is assumed to be isotropic in space and any correlations in the movements of near-neighbor atoms are neglected. $\overline{U_j^2}$ values can be obtained from, for example, LEED analyses[62,63]. However, the fact that the electron scattering is significant only when θ_j is rather close to zero acts through the $(1-\cos\theta_j)$ factor in the argument of Eq. (27) to yield W_j's very close to unity for all important scattered waves. Thus, the $\overline{U_j^2}$ values chosen for Cu can in fact be increased by a factor of four without appreciably altering the $I(\vec{k})$ curves[63]. So, vibrational effects are to first order not very important in forward-scattering dominated XPD, although they are, for example, very important in LEED, EXAFS, and normal photoelectron diffraction where back scattering is the dominant diffraction mode (and thus $\theta_j \gtrsim 180°$). An alternate method for allowing for vibrational effects is to assume some probability distribution of atomic positions due to vibration (as, for example, a harmonic oscillator envelope) and then to sum separate weighted diffraction intensities for all possible combinations of atomic positions. This is cumbersome, but it has been used to quantitatively look at the effects of specific types of molecular vibrations at surfaces[77,81].

The expression for intensity $I(\vec{k})$ can now be written down directly as:

$$I(\vec{k}) \propto \int \left| \hat{\varepsilon}\cdot\hat{k} e^{-\gamma L} + \sum_j \frac{\hat{\varepsilon}\cdot\hat{r}_j}{r_j} |f_j(\theta_j)| W_j e^{-\gamma L_j} (\exp i[kr_j(1-\cos\theta_j) + \psi_j(\theta_j)]) \right|^2 d\hat{\varepsilon}$$

$$+ \sum_j \int (\hat{\varepsilon}\cdot\hat{r}_j)^2 \frac{|f_j(\theta_j)|^2}{r_j^2} (1-W_j^2) e^{-2\gamma L_j} d\hat{\varepsilon}. \quad (28)$$

Here, $\hat{\varepsilon}\cdot\hat{k}$ and $\hat{\varepsilon}\cdot\hat{r}_j$ represent photoemission matrix-element modulations along the unit vectors $\hat{k}$ and $\hat{r}_j$, respectively, and $\exp(-\gamma L)$ and $\exp(-\gamma L_j)$ are appropriate inelastic attentuation factors. Thus, $(\hat{\varepsilon}\cdot\hat{k})\exp(-\gamma L)$ is the amplitude of the direct wave $\phi_0(\vec{r},\vec{k})$ and $(\hat{\varepsilon}\cdot\hat{r}_j)|f_j(\theta_j)|W_j \exp(-\gamma L_j)/r_j$ is the effective amplitude

of $\phi_j(\vec{r},\vec{r}_j,\vec{k})$ after allowance for both inelastic scattering and vibrational attenuation of interference. The complex exponential allows for the total final phase difference between ϕ_0 and each ϕ_j. The integrals on $\hat{\varepsilon}$ simply sum over different polarizations perpendicular to the radiation progagation direction, as appropriate to the usual case of a largely unpolarized x-ray source in XPS. The second $\sum_j$ corrects the first absolute value squared for the incorrect inclusion of Debye-Waller attenuations in terms involving a product of a scattered wave with itself. That is, in expanding the absolute value squared, only products involving unlike waves as $\phi_0\phi_j^*$ or $\phi_j\phi_\ell^*$ $(j \neq \ell)$ should include Debye-Waller products of W_j or W_jW_ℓ, respectively. The $(1-W_j^2)$ factor in the second summation is thus necessary to yield overall correct products of the form $\phi_j\phi_j^*$ without any W_j^2 factor. The second sum is termed the thermal diffuse scattering term and it is usually quite small with respect to the overall XPD modulations, because, as we have already noted, W_j is very close to unity for all strong scatterers. Eq. (28) is thus the basic starting point of the single scattering cluster model. It is also worth noting here that such a cluster sum makes no explicit use of the 2- or 3- dimensional translational periodicities that may be present, even though the atomic coordinates $\vec{r}_j$ used as inputs may incorporate such periodicities. Thus, neither surface- nor bulk- reciprocal lattice vectors are explicitly involved, and it makes no sense at this level of description to speak of diffraction "beams" associated with certain $\vec{g}$'s as in LEED.

Averaging over a totally unpolarized source leads to a more complex expression for $I(\vec{k})$ in terms of various geometric angles, but it can be shown that the strong forward peaking in $f_j(\theta_j)$ permits using the following relatively simple expression[62,63]:

$$I(\vec{k}) \propto |I_0 + \sum_j I_j W_j \exp\{i[kr_j(1-\cos\theta_j) + \Psi_j(\theta_j)]\}|^2 + \sum_j I_j^2(1-W_j^2) , \quad (29)$$

where θ_k or θ_{r_j} are the angles between the direction of radiation propagation and $\vec{k}$ or $\vec{r}_j$, respectively, and I_0 and I_j are defined as

$$I_0 = \sin\theta_k \exp(-\gamma L)$$

$$I_j = \sin\theta_{r_j} |f_j(\theta_j)| \exp(-\gamma L_j)/r_j .$$

That is, in averaging over $\hat{\varepsilon}$, $\hat{\varepsilon}\cdot\hat{k}$ has been replaced by $\sin\theta_k$ and $\hat{\varepsilon}\cdot\hat{r}_j$ by $\sin\theta_{r_j}$. It is this result that has been used in most XPD calculations to date.

The last parameter of importance in actually using Eqs. (28) or (29) is the range of j or the choice of a suitable cluster of atoms. This is done empirically so as to include all significant scatterers by verifying that the predicted XPD patterns do not change in any significant way with the addition of further atoms at the periphery of the cluster. The inherent weakness of all scattering events

for which θ_j is appreciably different from zero tends to limit cluster sizes in most cases. They thus can range from 2 atoms for near-normal emission from a vertically oriented diatomic molecule on a surface[77] to as many as several hundred atoms for substrate emission in which both the emission and scattering must be summed over several layers into the bulk[62,63]. However, even for the largest clusters so far considered, the inherent simplicity of Eqs. (28) and (29) still yields calculations which do not consume excessive amounts of computer time, especially by comparison with those necessary for LEED or UPS simulations.

A further physical effect of importance in making comparisons to experiment is the possibility of electron refraction at the surface, as discussed previously in Section 3.C. Fig. 14 indicates that, even at the relatively high energies of XPS, for emission near grazing, angle changes θ'-θ of a few degrees can be produced by refraction. Thus, especially for adsorbate studies such as that shown in Fig. 30, a proper allowance for refraction is necessary, at least for θ values $\lesssim 10°$. This is done by using a suitable inner potential V_0 derived from experiment and/or theory and Eq. (19) to predict θ for a given internal propagation direction θ'. In the presence of an adsorbate, the exact form of the surface potential barrier thus becomes important, as it may not then be possible to assume an abrupt rise to the vacuum level at the substrate surface. Also, the presence of adsorbate atoms may alter V_0 through changes in the work function, and these atoms also may occupy positions above the surface in which only a fraction of V_0 is appropriate. Although a prior study of O on Cu(001) indicates that the predicted XPD results are not particularly sensitive to the choice of V_0[62,63], it is important to realize that not properly allowing for it may shift theoretical XPD patterns by as much as a few degrees with respect to the actual θ values at which they will be observed.

A final step in any realistic calculation based upon this model is to integrate the direction of emission $\vec{k}$ over the solid angle Ω_0 accepted into the electron analyzer[62,63]. For most of the calculations reported here, this has been over a cone of ±3.0-3.5° half angle, although for certain cases a smaller cone of ±1.5° has been used.

There are several reasons, however, why the XPD effects predicted by such SSC calculations are from the outset expected to be larger in amplitude than those observed experimentally. (This is a common type of discrepancy in other diffraction calculations as well, as, for example, in LEED.) These have been discussed previously in connection wtih XPD[63], and are: (1) The actual surface may have irregularities on an atomic scale that are not included in the usually idealized model cluster. Also, adsorbates may exhibit more than one type of bonding site, especially if unobserved steps or dislocations are present on the surface to some degree. These effects will in general tend to average out XPD effects in experimental data relative to a highly ideal calculation. (2) The lack of a fully-converged cluster of atoms in the calculations would also tend to produce greater anisotropy, as atoms near the periphery of a larger cluster add so as to produce a nearly isotropic background. (3) The inclusion of spherical-wave character for nearest-neighbor scattering will qualitatively tend to reduce the scattering strength, at least in the forward direction. This effect has been quantitatively estimated in XPD calculations for C1s emission from molecular CO, where it appears to reduce the forward scattering diffraction peak by about 1/2 as measured with respect to the background intensity[77]*. (4) Vibrational effects, especially at a surface or for an adsorbate, may not be adequately described by simple Debye-Waller factors, and lead to enhanced supression of XPD features. (5) Multiple-scattering effects also may be present to some degree, and these would generally be expected to smear out some features. (6) The presence of a non-isotropic inelastic scattering mechanism (for example, associated with excitations of rather localized valence electrons) also could reduce the relative intensities of diffraction features. Such phenomena have been noted as a source of reduced diffraction effects in EXAFS back scattering, for example, although it appears that for forward scattering the optical theorem[78] will require an increase in $|f_j|$ due to inelastic processes[82]. Such effects need to be further investigated for forward scattering at the $\sim 10^3$ eV energies appropriate to XPS. The last four of these effects thus need to be explored in further theoretical treatments of XPD, but we shall show that the much simpler SSC model not incorporating them still seems to describe the observed experimental phenomena rather well.

As a final comment concerning the SSC model, we note that it can be directly reduced to an expression very close to that used in EXAFS analyses[72] if it is assumed that all scattered waves ϕ_j are small in magnitude in comparison to ϕ_0. Then, if we begin at Eq. (28) (for simplicity neglecting any averaging over $\hat{\varepsilon}$), we see that all terms such as $\phi_j\phi_\ell^*$ and $\phi_j\phi_j^*$ can be neglected in expanding the absolute value squared. The thermal diffuse scattering term thus can also be neglected. After some simple algebra, it can then be shown that

$$I(\vec{k}) \propto (\hat{\varepsilon}\cdot\hat{k})^2\, e^{-2\gamma L} + 2(\hat{\varepsilon}\cdot\hat{k})e^{-\gamma L}\sum_j \frac{\hat{\varepsilon}\cdot\hat{r}_j}{r_j}\,|f_j(\theta_j)|W_j e^{-\gamma L_j} \times \cos(kr_j(1-\cos\theta_j) + \psi_j(\theta_j)). \qquad (30)$$

This simplified form has in fact been used recently by Orders and Fadley in successfully describing several aspects of normal photoelectron diffraction data[83].

*This factor of approximately 0.4-0.5 for nearest-neighbor scattering has also been verified in recent much more detailed XPD spherical-wave calculations by Saqurton, Bullock, and Fadley(to be published).

In subsequent sections, we will consider several applications of this SSC model to the interpretation of XPD data, including especially several substrate- and adsorbate- systems of known geometry to test the degree of its validity.

C. Substrate emission

The first quantitative comparisons of theoretical and experimental XPD curves were for azimuthal scans above a Cu(001) surface[62,63]. Some of this data for $Cu2p_{3/2}$ emission is shown in Fig. 37 (cf. Fig. 27), and a more recent comparison using higher and lower angular resolutions has been presented in Fig. 31. Consider first the theoretical curves labelled "damping = 1.0" in Fig. 37, which represent non-adjusted SSC calculations according to Eq. (29), as do the theoretical curves of Fig. 31. It is clear from these figures that simple SSC calculations are capable of predicting the positions and approximate relative intensities of most of the features observed, even down to the very narrow peaks noted for $15° \lesssim \phi \lesssim 75°$ in Fig. 31. There are, to be sure, some minor discrepancies as to features, as for example, in Figure 37 where the local minimum in experiment is not present in theory for $\phi = 45°$ and $\theta = 10°$ and the maxima in experiment for $\phi = 90°$ and $\theta = 13°$, 15°, 18.4°, and 45° are local minima in theory. Also, the degree of anisotropy is overestimated by theory by a factor of ~1.5-2.0, but this is not surprising in view of our prior discussion of the model.

The overall agreement between theory and experiment for Cu is improved somewhat by the empirical reduction of each scattering amplitude $|f_j|$ by a factor of 1/2[63]: such curves are denoted by "damping = 2.0" in Figure 37. Such an empirical reduction in $|f_j|$ might be justified in allowing for some or all of the last four factors discussed in the preceding section as being responsible for overestimates of anisotropy by theory,* but its magnitude has been rather arbitrarily chosen to optimize agreement, so that such adjustments will not generally be utilized in what follows and, if so, will be specifically indicated.

As more recent examples of such comparisons, we note that the closely-related crystal Ni(001) exhibits XPD azimuthal patterns very close to those of Cu(001), and somewhat better agreement with non-adjusted SSC calculations[84].

Also, Kono[85] has recently compared SSC calculations and experiment for <u>polar</u> scans above a LaB_6 crystal. Fig. 38 shows such a comparison for La4d emission, and it is clear that all main features are correctly predicted as to position and approximate relative intensity. (The experimental data here have not been corrected for a smooth-curve modulation due to the instrument response function.) Takahashi et al.[86] have also recently compared azimuthal XPD data for Ag3d

*Such empirical adjustments in $|f_j|$ by approximately 0.4-0.5x have also been found to improve agreement with experiment in more recent work (ref. 100 and Trehan and Fadley, to appear in Phys. Rev. B), and their principal origin in spherical-wave effects(ref. 77) has also been confirmed by Sagurton, Bullock, and Fadley(to be published).

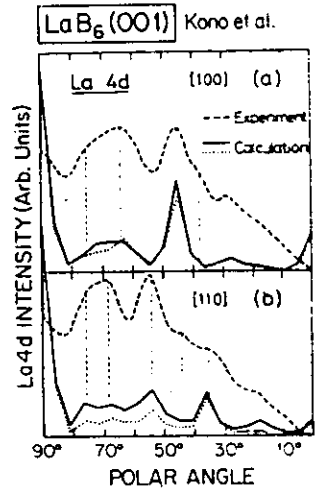

Fig. 38. Comparison of experiment and SSC theory for the polar dependence of La4d emission from LaB_6(001) along the [100] and [110] azimuths. The solid-curve theory includes both La and B atoms as scatterers; the dotted-curve theory includes only the much heavier La atoms as scatterers. No allowance for the instrument response function has been made in plotting the experimental data. (After Kono, ref. (85).)

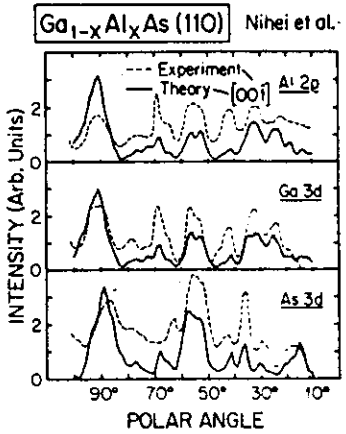

Fig. 39. Comparison of experiment and SSC theory for the polar dependence of Al2p, Ga3d, and As3d emission from $Ga_{1-x}Al_xAs$(110). (After Owari et al., ref. (87).)

emission from a Ag (110) crystal wtih SSC theory and found very good agreement for all major features.

As a final example, we show in Figure 39 a very recent comparison of SSC calculations and experimental results obtained by Nihei et al.[87] for polar scans of three core peaks in a crystal of $Ga_{1-x}Al_xAs$ ($x \gtrsim 0.5$) with (110) orientation. The SSC model utilized was somewhat simplified from that discussed here. Again, almost all of the features are correctly predicted in position and relative intensity, with the sole exception being a shift of ~6° of two features for As3d in the range $50° \lesssim \theta \lesssim 70°$.

Overall, the test cases studied to date thus permit tentatively concluding that SSC calculations provide a very good description of the XPD effects associated with substrate core-level emission. The degree of agreement found is even somewhat surprising in view of the fact that emission along or near lines of atoms in the crystal might be expected to enhance the importance of multiple scattering effects. (Perhaps this is the reason for the slight featural disagreements seen in Fig. 31 near $\phi = 0°$ and 90°, as this corresponds to emission along <110> directions.) Comparing SSC calculations with experimental measurements thus should much increase the certainty of site-type determinations, such as those represented by Figs. 32 and 33. Anticipating the next sections on adsorbate emission, we also note that emission along lines of atoms is generally not possible, so that SSC results might be expected to better describe experiment in at least this respect.

In concluding on substrate emission, we also note an alternate description of such effects in terms of Kikuchi bands[2,6,65,88]. This emphasizes photoelectron diffraction from different sets of planes in the crystal as denoted by Miller indices (hkℓ), and each set is expected to have associated with it a band of enhanced intensity for photoelectron emission within plus or minus the Bragg angle $\theta_{hk\ell}$ of being parallel to these planes. If the interplanar spacing is $d_{hk\ell}$, then the Bragg angle is determined from

$$\lambda_e = 2d_{hk\ell} \sin \theta_{hk\ell} \quad . \tag{31}$$

One thus qualitatively expects peaks of intensity for emission along low-index directions in which several sets of planes intersect, as discussed previously. Maxima at $\sim\pm\theta_{hk\ell}$ away from the planes are also expected and such features are seen in both experiment and SSC theory in Fig. 31 for $\phi \gtrsim 10°$, 80°. This model has been compared to experimental data both qualitatively[65] and quantitatively (using a simple superposition of independent (hkℓ) Kikuchi bands)[88,89], and found to provide a semi-quantitative zeroth-order description of substrate XPD. A more detailed comparison of the Kikuchi-band and SSC models appears elsewhere[88].

D. Emission from molecular adsorbates

Although the first adsorbate XPD was actually observed for an atomic adsorbate (O on Cu(001)[62,63]), it is heuristically useful to begin by considering two simple effects arising in small-molecule adsorption. These have both been studied for the system c(2x2)CO on Ni(001)[77,81].

(i) Intramolecular Scattering. Fig. 29 shows polar-scan experimental data for C1s emission from c(2x2)CO on Ni(001) for two different high-symmetry azimuthal orientations[62,80]. The C1s intensity has been normalized by dividing by the featureless O1s intensity to allow for the instrument response function, and a clear peak along the surface normal is found. A qualitative explanation of this in terms of intramolecular scattering is indicated in the inset of this figure. C1s photoelectrons are preferentially forward-scattered by the O atom in the same molecule so as to produce a constructive interference and therefore a peak in intensity directly along the C-O bond direction. This forward-scattering peak can also be termed a 0th order diffraction peak, as the scattering phase shift is very small (it is shown for simplicity to be zero in the schematic drawing). At larger angles away from the bond direction, 1st order diffraction effects might also be expected, but they cannot be resolved for certain in this data.

A more quantitative description of this data requires using the SSC model, as has been done in two prior studies[77,81]. Because the electron emission directions of interest are rather near the surface normal, the substrate Ni atoms or other CO molecules around a given emitter will be associated with scattering angles of $\gtrsim$90°. Thus, it has been shown that they have a negligible influence on such intramolecular XPD and a two-atom cluster (a C emitter and an O scatterer) is sufficient. The other important parameters of the calculation are the tilt angle θ_t of the bond axis away from the surface normal and an rms vibrational amplitude θ_{rms} for a wagging or frustrated rotational motion of the CO. θ_{rms} is incorporated via a ground-state harmonic oscillator probability distribution, and is expected to be near 10° for CO on Ni(001) at ambient temperature.

Fig. 40 compares experiment and theory for $\theta_{rms} = 10°$ and various choices of θ_t. (Again, theory predicts $\lesssim$2 times larger XPD effects than are observed and at least half of this overestimate has been shown to be neglect of curved-wave effects due to the short C-O distance[77].) An intensity maximum along the surface normal such as that observed experimentally is found in the SSC curves for all tilt angles $\lesssim$14°. Considering further the FWHM of this 0th order peak is found to limit the tilt to $\theta_t \lesssim 10°$. This conclusion is also possible in the presence of greater degrees of vibrational motion[81].

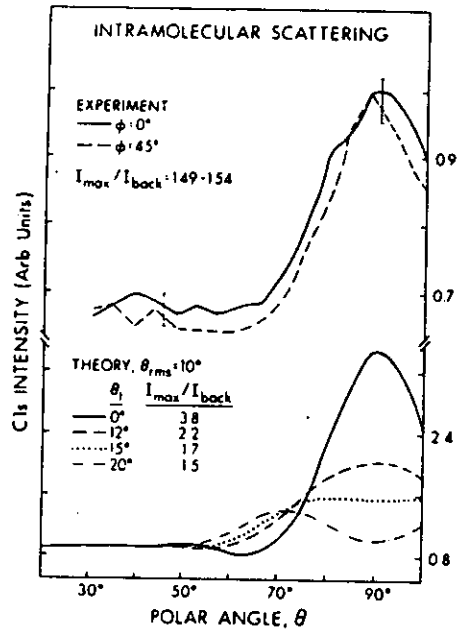

Fig. 40. Comparison of experiment and SSC theory for the polar dependence of C1s emission from c(2x2)CO on Ni(001). The calculations have been performed with a fixed root-mean-squared vibrational displacement of 10° and several tilt angles θ_t of the CO molecule relative to the Ni surface. The amplitudes of these intramolecular scattering phenomena are indicated here by the maximum-to-background ratio I_{max}/I_{back}. (From Orders and Fadley, ref. (81).)

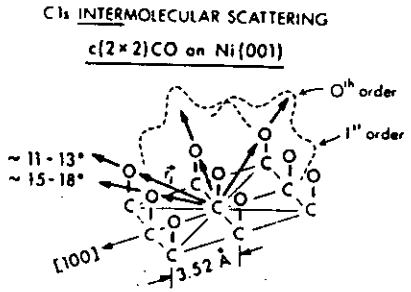

Fig. 41. Schematic illustration of the mechanism by which intermolecular scattering produces azimuthal anisotropy in C1s emission from c(2x2)CO on Ni(001). (From Orders and Fadley, ref. (81).)

Thus, this analysis permits rather straightforwardly determining the orientation of CO on this surface to within ~10°. It also suggests the general utility of such effects in studying the orientations of small molecules on surfaces, as the 0th order peak intensity in general follows the bond direction. All that is required is for an atom of reasonable scattering power (that is, of atomic number $\gtrsim$4-8) to lie between the emitting atom and the detector. Such intramolecular scattering effects thus provide a type of information very similar to that available from electron stimulated desorption ion angular distributions (ESDIAD)[90] and polarization-dependent core-level absorption edge structure measurements[91]. However, the theoretical picture in XPD seems both simpler and more clearly understood than either of these other two methods, and a synchrotron radiation source is not needed to carry out the XPD measurements, although it is for absorption edge studies.

(ii) Intermolecular scattering. A further type of XPD effect possible for an ordered overlayer of adsorbed molecules is illustrated for the case of c(2x2)CO on Ni(001) in Fig. 41. C1s emission is again considered, but in this case, for near-grazing emission directions for which scattering by O atoms in near-neighbor molecules along the surface is possible. Each O atom thus may generate both 0th order and 1st order XPD structure. For the expected C-O bond length, these effects are expected to occur for emission angles of ~10°-20° with respect to the surface. At lower angles, intermolecular scattering by C atoms in adjacent molecules also may be significant. The qualitative expectation is thus that azimuthal scans of C1s intensity should exhibit 0th order peaks at ϕ = 0°, 45°, 90°, ... (as measured from the [100] direction), with extra structure at intermediate angles possible due to 1st order effects.

Such intermolecular effects have been experimentally observed[81], as illustrated in Fig. 42 for scans at various polar angles. These data have been fourfold-averaged over a full 360° scan to reduce noise. As noted previously, the degree of mirror symmetry about ϕ = 45° can be used to judge the statistical accuracy of a given feature. Although low intensities make the statistical scatter of these measurements rather high, intermolecular scattering effects are clearly seen at the two lowest angles of θ = 7° and 11°, including 1st order peaks at ϕ positions of ~22° and ~68°. The overall anisotropies are ~15% for these low θ values, with rapidly decreasing values as θ is increased to a maximum of 18°. Also shown in Fig. 42 are SSC theoretical curves incorporating the effects of both types of adjacent CO molecules (that is, those at ϕ = 0° and 45°). Independent wagging vibrations of these molecules have also been included, with a θ_{rms} value of 10°.[81] Although theory again overestimates the degree of anisotropy, this time by ~4

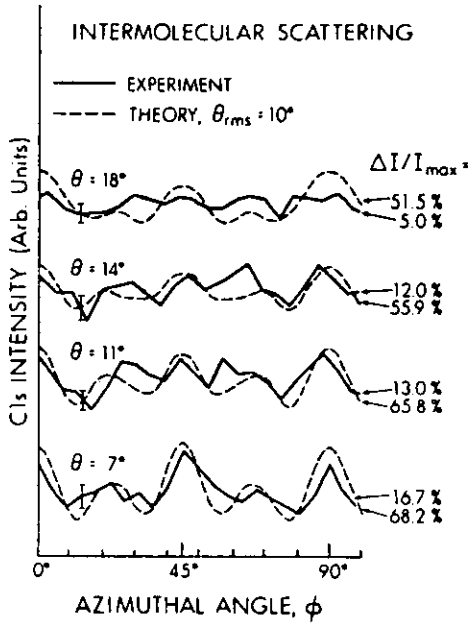

Fig. 42. Comparison of experiment and SSC theory for the azimuthal dependence of C1s emission from c(2x2)CO on Ni(001). The diffraction effects seen are due to intermolecular scattering (cf. Fig. 41). (From Orders and Fadley, ref. (81).)

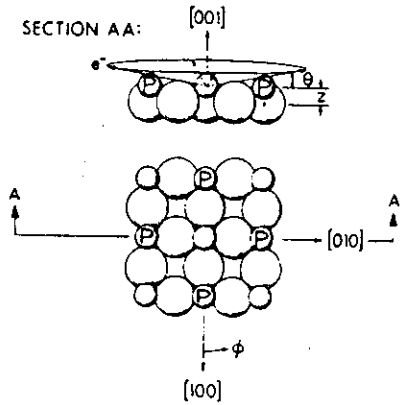

Fig. 43. General atomic geometry for c(2x2) and p(2x2) adsorbate overlayers on a (001) surface of an fcc metal, assuming that adsorption is in fourfold-hollow sites. In c(2x2), all sites are occupied; in p(2x2) only those denoted by "P".

times, the peak positions and approximate relative intensities agree very well with experiment, especially at the two lowest θ values. A more detailed discussion of these effects, including theoretical curves for varying degrees of vibrational motion, appears elsewhere.[81]

Thus, such intermolecular scattering effects should provide rather direct information on the short-range order in an adsorbate overlayer. This is by contrast with measurements such as LEED, for which long-range order over distances of $\sim 10^2$ Å is necessary for sharp patterns to be observed. Particularly with further developments in instrumentation to increase intensity, as well as angular precision and accuracy, such XPD effects thus should provide very useful surface structural information.

E. Emission from atomic adsorbates

We begin here by discussing several recent test cases designed to explore the angular sensitivity of x-ray photoelectron emission from core levels of atomic adsorbates, as well as to determine the degree to which the single scattering cluster model can be used to quantitatively describe such effects. Several practical applications to structural determinations are then discussed, together with estimates of structural sensitivity for different types of adsorption, and suggestions for improving the structural sensitivity. The use of polarized and energy-tunable synchrotron radiation for such XPD studies is also considered.

(i) Well-defined test cases. Fig. 30 makes it clear that XPD effects can be observed in emission from a core level of an atomic adsorbate, and furthermore that the resulting azimuthal patterns are very sensitive to the polar angle of emission. The discussions of the preceding two sections on substrate- and molecular adsorbate- emission also strongly suggest that a single scattering cluster model should be adequate for describing these effects. However, it is nonetheless necessary to test this idea by comparing experiment and SSC calculations for some well-defined adsorbate geometries. This has been done recently by Orders et al.[69] for c(2x2)S and c(2x2)Se on Ni(001). These overlayers have been studied previously by LEED and NPD and both consist of atomic adsorption in fourfold hollow sites, with S at a vertical distance of z = 1.30-1.35 Å above the first Ni layer[45] and Se at a distance of z = 1.55-1.60 Å; every other fourfold site is occupied, as illustrated in Fig. 43.

A series of azimuthal scans for S2p emission from c(2x2)S on Ni(001) at different polar angles θ between 7° and 17° are shown in Fig. 44 in comparison to SSC theoretical curves for z = 1.30 Å. Note that some of the θ steps here are only 1° in magnitude. Considering first only the dashed experimental curves, we

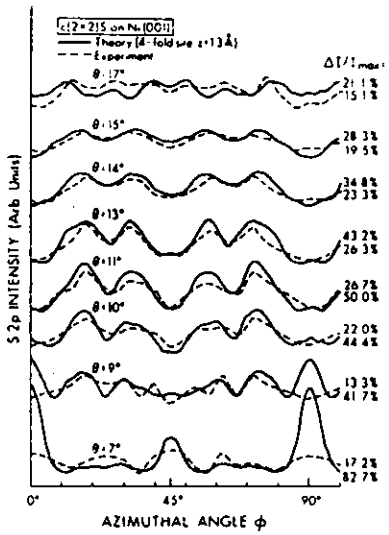

Fig. 44. Comparison of experiment and SSC theory for the azimuthal dependence of S2p emission from c(2x2)S on Ni(001) at eight closely-spaced polar angles. The theoretical calculations were performed for the generally accepted geometry of 4-fold S bonding at a vertical distance of z = 1.30Å (cf. Fig. 43). (From Connelly, ref. (33).)

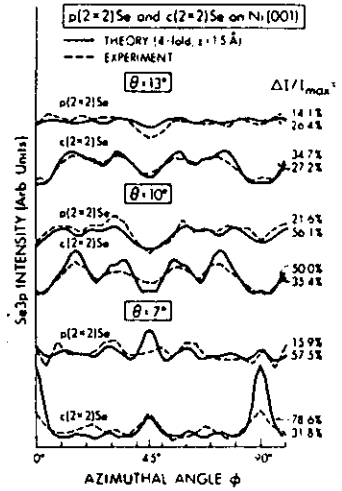

Fig. 45. Comparison of experiment and SSC theory for the azimuthal dependence of Se3p emission from p(2x2)Se and c(2x2)Se on Ni(001) at three different polar angles. The calculations were performed for the accepted geometry of 4-fold Se at z = 1.5Å. (From R. E. Connelly and R. C. White, unpublished results.)

see that the patterns change very much with θ, particularly in the range of ∿7°-11°. The expected mirror symmetry about φ = 45° is also seen in all of the experimental data, and provides strong confirmation of all of the features present in these curves. A comparison now of experiment with the SSC calculations shows that, with very few exceptions, all of the peak positions and relative intensities, and by implication thus also the changes in structure with θ, are correctly predicted by this simple model. As usual, theory predicts more anisotropy than experiment, here by ∿1.4-4.9 times, depending on the θ value. However, the only significant discrepancies as to features between experiment and theory are associated with the symmetry-identical peaks at φ = 0° and 90° for θ = 7° and 9° (and very slightly also for 10°); these peaks are predicted to be ∿2-3 times too high in theory for θ = 7°, and for this reason also persist as significant features at θ = 9° even though they are not observed experimentally. A consideration of the SSC calculations shows that, for low θ values $\lesssim$7°, the peaks at φ = 0°, 90° are produced by forward scattering or 0th order diffraction from nearest-neighbor S atoms to the emitter which are located along <100>-type directions (cf. Fig. 43). Similarly, the peak for very low θ values at φ = 45° is associated with forward scattering by next-nearest neighbor S atoms along <110>-type directions. One likely reason for overestimating the strength of nearest-neighbor scattering is that these SSC calculations assumed no refraction in scattering events from the adsorbate, thereby emphasizing smaller-angle adsorbate events too much in the final angular averaging. Also, for such close distances between emitter and scatterer, the use of the small-atom approximation may not be fully valid, and curved-wave corrections would thus be expected to effectively reduce the forward-scattering strength. It is also possible that surface non-idealities and microscopic roughness could become more important for very low takeoff angles (as discussed in another context in Sec. 3.C), and that both non-isotropic inelastic scattering and multiple scattering effects could be more important for this type of nearest-neighbor forward scattering. In any case, the overall agreement is very encouraging.

A similar comparison of experiment and SSC calculations has also been made for c(2x2)Se or Ni(001)[69], and it yields essentially identical conclusions. Some of this data is shown in Fig. 45, where the only significant discrepancies are again in the relative intensities of the φ = 0°, 90° peaks at θ = 7°, as well as in slight position shifts of ∿3-4° in the doublets for 10° $\lesssim$ φ $\lesssim$ 35° and 55° $\lesssim$ φ $\lesssim$ 80°. Overall, then, these two test cases thus provide further strong support for the quantitative utility of SSC in describing XPD from adsorbates. (Further experimental and theoretical studies aimed at explaining the few discrepancies noted are nonetheless desirable.)

(ii) Structural sensitivity and structural determinations. In addition to the test cases discussed in the prior section, adsorbate XPD measurements combined with SSC calculations have been used to study the atomic geometries of several more complex systems: c(2x2)O on Cu(001)[62,63], p(2x2)O and c(2x2)O on Ni(001)[92], and O on the stepped Cu surfaces (211) and (410)[80]. We begin by discussing the apparent structural sensitivities seen in some of these studies from both experimental and theoretical points of view.

As a first example of sensitivity to the type of overlayer structure present, Fig. 45 compares experimental and theoretical azimuthal scans from the well-defined overlayers c(2x2)Se on Ni(001) and p(2x2)Se on Ni(001). Considering experiment first, we see that there are major differences between c(2x2) and p(2x2) for all three polar angles shown. Thus, XPD is clearly very sensitive to this change in overlayer structure, albeit a rather large one. Again with only a few exceptions as to relative intensity, the theoretical curves very well predict the experimental curves for both overlayers; in fact, the only points of significant disagreement are for c(2x2)Se at $\theta = 7°$, and have been discussed in the last section. This comparison thus also lends further support to the applicability of the SSC model for describing XPD data.

In proceeding further to consider structural sensitivity, the adsorbate vertical position emerges as a critical parameter of interest. As a first illustration of how this can affect adsorbate XPD, we consider in Figs. 46 and 47 comparisons of experiment and theory at different z values for O1s emission from the expected fourfold hollow sites of c(2x2)O on Cu(001)[62,63]. (Although most of the theoretical curves shown are for $\beta \equiv$ damping = 2.0 and thus have had the $|f_j|$ values reduced by 1/2, their forms do not change significantly for $\beta = 1.0$, and thus none of the discussion below is altered with the use of unadjusted $|f_j|$'s.) Comparing experiment and theory here for z values above and below the atomic centers of the Ni surface plane at $z = 0.0$ Å shows that at $\theta = 10°$ the region of best agreement is for ~ -0.1 Å to +0.1 Å. For $\theta = 13°$, it would seem that 0.0 Å to -0.1 Å is the region of maximum agreement. Similar comparisons at a total of five θ values ultimately permitted Kono et al.[62,63] to propose that c(2x2)O is bonded in 4-fold hollow sites at a position that is co-planar with the surface Cu atoms to within $\sim \pm 0.1$ Å (that is, at $z = 0.0 \pm 0.1$ Å). Including the Cu atom immediately below the hollow, this yields a five-fold coordination for O with a Cu-O bond distance of 1.81 Å that is not very different from the 1.85 Å in the compound Cu_2O. Although no prior definitive determination of this structure has been made, very recent NPD measurements on this system are also at least partly consistent with a nearly in-plane adsorption[93], and previous LEED[94] and SIMS

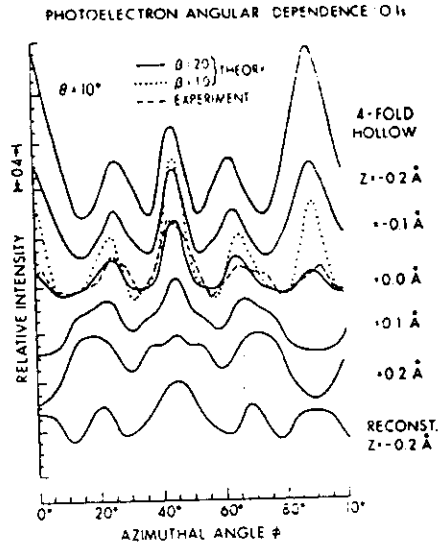

Fig. 46. Comparison of experiment and SSC theory for the azimuthal dependence of O1s emission from c(2x2)O on Cu(001) at $\theta = 10°$ and for different adsorption geometries. $\beta = 2.0$ has the same significance as damping = 2.0 in Fig. 37; $\beta = 1.0$ corresponds to damping = 1.0 or no adjustment of the $|f_j(\theta j)|$ values. Experiment and theory are compared for five z positions of 4-fold bonding and for the empirically optimum value for a previously proposed reconstructed geometry. (From Kono et al., ref. (63).)

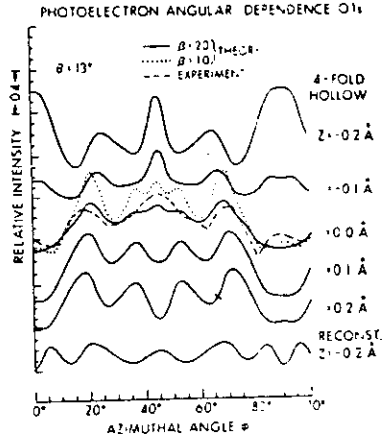

Fig. 47. As Fig. 46, but for $\theta = 13°$.

angular distribution[95] studies have also found this geometry to give one of the best fits to experiment.

A further indication of structural sensitivity is shown by the bottom curves in Figs. 46 and 47, which were calculated for another trial adsorption geometry: a reconstructed Cu surface in which O replaces every other Cu atom in the first layer. The z distance of -0.2 Å was chosen to optimally fit experiment at all θ values, but this fit is clearly very poor at θ = 13°, even though it is reasonable at θ = 10°. The reconstructed geometry thus could be ruled out. This illustrates both the necessity of using a rather full XPD data set at multiple polar angles and also the potential sensitivity of XPD to the bonding site type.

A similar XPD study of various O exposures on Ni(001) spanning the p(2x2) to c(2x2) transition in LEED[92,99] also permitted concluding that lower exposures involve fourfold O atoms at $z \approx 0.8 \pm 0.2$ Å, whereas at higher exposures, a considerable fraction of the fourfold O is nearly co-planar with Ni at $z = 0.1 \pm 0.2$ Å. This conclusion has subsequently been confirmed in high-resolution electron energy loss measurements on the same system[96], although it is at variance with recent NPD[97] and SEXAFS[98] measurements, which suggest above-plane adsorptions for both p(2x2) and c(2x2). Possible explanations for this apparent discrepancy are a variable degree of above-plane and co-planar mixing with different specimen preparation treatments, as well as an enhanced sensitivity of XPD to O in the co-planar sites where smaller-angle substrate scattering is possible[92].

However, the situation concerning vertical sensitivity is not quite as simple for all cases as that illustrated in Figs. 46 and 47. Fig. 48 shows a similar comparison of experiment and theory at different z values for c(2x2)S on Ni(001). Although significant changes in features occur with z for z values up to ~1.0 Å, beyond this point, the pattern is rather stable, with only very subtle changes in fine structure. Thus it would be difficult to conclude much more than $z \gtrsim 1.0$ Å by comparing experiment and theory for this case, and similar conclusions obtain for the other polar angles of emission in Fig. 44[99]. The same sorts of trends are seen also for c(2x2)Se on Ni(001)[99], and lead to the conclusion that vertical position sensitivity is lost if the adsorbate is too far above the surface plane.

The explanation of this lies straightforwardly in the forward-peaked nature of electron-atom scattering in XPS, and is illustrated schematically in Fig. 49. For low θ values and an adsorbate lying closer to the substrate surface, small-angle scattering is possible from both other adsorbate and substrate atoms. Since only substrate scattering can provide information on the adsorbate-substrate distances, a high z sensitivity of the order of ±0.1 Å results. On the other hand, when the adsorbate is too far above the surface ($\gtrsim$1.3 Å for O on Ni, $\gtrsim$1.0 Å for S on Ni, $\gtrsim$ 0.8 Å for Se on Ni, and $\gtrsim$0.7 Å for Te on Ni[99]), the scattering angles from the

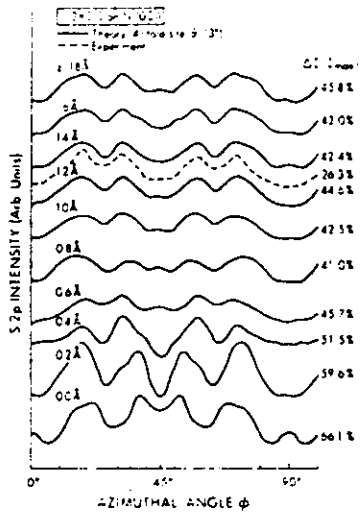

Fig. 48. As Fig. 47, but for c(2x2)S in 4-fold coordination on Ni(001) and a broader range of z values; B = 1.0 for all curves. (From Connelly, ref. (33).)

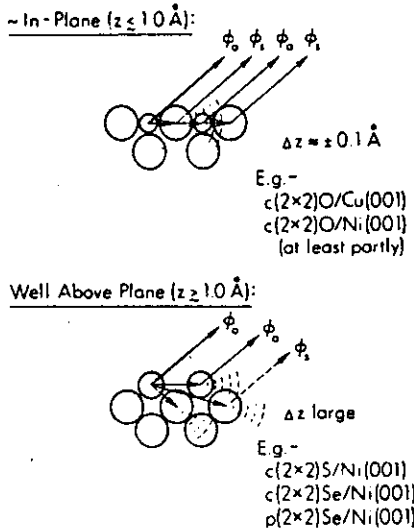

Fig. 49. Schematic explanation of the differing sensitivity of azimuthal XPD depending upon the height of the adsorbate above the substrate, with specific examples of each type of bonding indicated.

near-neighbor substrate atoms of most significance are too large to yield appreciable scattered waves ϕ_j, and the z sensitivity is very low. In fact, the XPD is predominantly produced by scattering in the two-dimensional adsorbate overlayer, as is found to be the case, e.g., for both S and Se on Ni(001). The inherent scattering strengths of the atoms involved also are important parameters here, and one can see a systematic trend through the chalcogenides in the values given above. Thus, a very low atomic number adsorbate on a very high atomic number substrate would tend to show more site type and z sensitivity at higher z values, and vice versa.

Thus, although there are to be sure a great many surface chemical problems for which adsorbed or reacting species will occupy sites at $z \lesssim 1.0$ Å with respect to the substrate surface and thus be amenable to high-precision study by XPD, the amount of information derivable for other problems involving greater z distances will be more limited. The question thus arises as to whether the method of carrying out such measurements can be changed in some way so as to improve z sensitivity, and two possible solutions seem promising. The simplest is to increase the angular resolution of the analyzer, so that more fine structure can be resolved in the XPD patterns. A theoretical simulation of this for c(2x2)S on Ni(001) is shown in Fig. 50, where curves for a cone of 3.0° half angle are compared to those for a cone of 1.5° half angle at various z values. Although the ±3.0° curves are essentially constant in form for $z > 1.2$ Å, those for ±1.5° continue to show changes in fine structure up to the rather high value of 1.8 Å. Thus, especially if a family of such azimuthal scans at high angular resolution and for various θ values were analyzed simultaneously, it should be possible to increase the sensitivity to both site type and z for higher z values. (On the negative side, however, would be the unavoidable intensity loss in increasing the angular resolution.)

A second possibility for improving z sensitivity is to use polarized synchrotron radiation and preferentially direct the primary photoelectron emission toward the substrate, as shown in Fig. 51. In so-called s polarization with the $\vec{\epsilon}$ vector lying in the plane of the surface, the maximum emission from a level exhibiting a typical XPS differential cross section will be toward the other adsorbate atoms, thus minimizing substrate scattering and lowering the z sensitivity. By contrast, in a p polarization geometry chosen to maximize the emission toward the substrate and minimize that toward the other adsorbate atoms and in the direct wave ϕ_0, the influence of the substrate should be markedly enhanced in the observed XPD. (Although to be sure a potential disadvantage of such a geometry is that the overall photoelectron intensity may also be markedly reduced.) As an illustration of the possible magnitudes of such polarization effects, Fig. 52 shows a

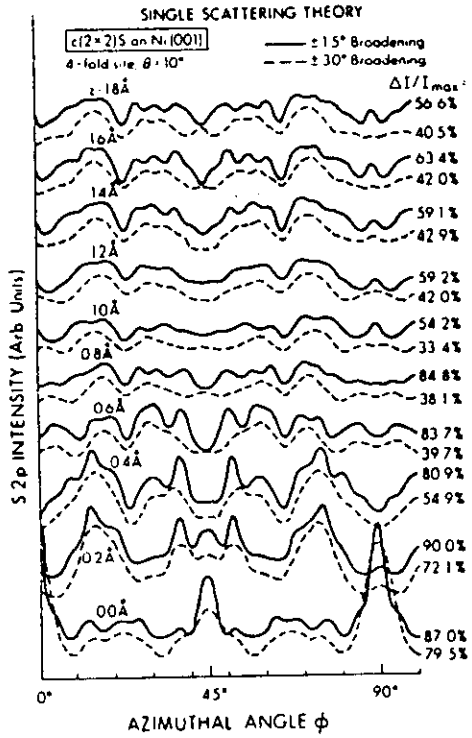

Fig. 50. The effect of reducing analyzer acceptance from ±3.0° to ±1.5° on azimuthal XPD. Theoretical SSC curves for the azimuthal dependence of S2p intensity from c(2x2)S on Ni(001) at θ = 10° are shown for the two angular acceptances and a range of 4-fold-coordinate z values from 0.0Å to 1.8Å. (From Connelly, ref. (33).)

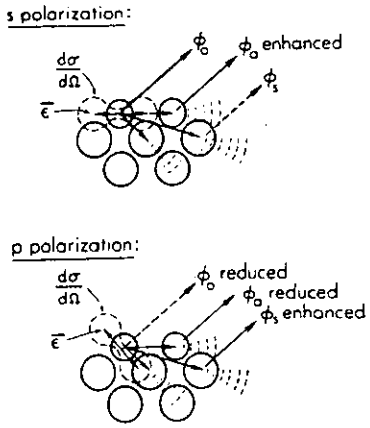

Fig. 51. Schematic explanation of how azimuthal XPD experiments in a

comparison of calculated XPD curves for c(2x2)S on Ni(001) with s- and p-polarization, and for various z values. The forms of these curves at $\theta = 10°$ (as well as at other angles not shown) are very much changed by the change in polarization, and the anisotropies for the p-polarized cases are larger by as much as a factor of 2. Recent experiments by our group at the Stanford Synchrotron Radiation Laboratory have confirmed this polarization sensitivity in XPD.[100] Also, although the curves for s polarization cease changing appreciably with z for $z \gtrsim 1.4$ Å in p polarization, changes in fine structure continue to occur all the way up to z = 2.0 Å. Thus, with increased angular resolution and/or the use of polarization variation, it appears that the high-z limitations on z sensitivity in XPD could be substantially improved.

As a further example of structural determinations using XPD, we briefly consider a recent study by Thompson and Fadley[80] of O adsorbed on the stepped Cu surfaces (211) and (410). Such surfaces are of considerable interest as controlled models of what may be the active sites on metal catalysts. As one illustration from this work, the (211) surface is found via LEED examination to reconstruct under oxygen exposure to the geometry shown in Fig. 53. It consists of a regular series of 5-atom terraces of (111) orientation and 2-atom step faces of (100) orientation. The most likely high-symmetry adsorption sites for atomic oxygen are also shown as A-C, and these can be further designated as A = 4-fold top, B = 4-fold bottom, and C = 3-fold. However, there is no prior evidence to suggest which of these sites will be occupied first, or whether a mixture of occupied sites may arise. Prior chemisorption studies on the separate low-index (111) and (100) faces do suggest however that (100) atoms should be much more reactive than (111) atoms, and it is also expected that atoms on or near step faces may exhibit higher reactivity as well.

It is thus of considerable interest to see whether oxygen adsorbed on this stepped surface exhibits any XPD features that are clearly influenced by the presence of the steps. A 5 Langmuir exposure to O_2 was found via an analysis of XPS core-peak intensities to yield a coverage equivalent to ~1 atom per high-symmetry site along the step face (or about 11% of a monolayer); this exposure also occurs at a distinct break in the curve of coverage vs. exposure for which the surface can be considered nearly saturated with O. Full 360° azimuthal scans of the O1s intensity for this system showed pronounced XPD effects, as illustrated in Fig. 54 for $\theta = 10°$. $\phi = 0°$ here corresponds to emission in an azimuth perpendicular to and away from the step faces. The reproducibility of features between the two halves of the scan (which should be mirror symmetric due to the presence of the steps) is also very good, especially for the most pronounced peaks between $\phi \approx 60°$ and $\phi \approx 140°$. Similar reproducibility was found for data obtained

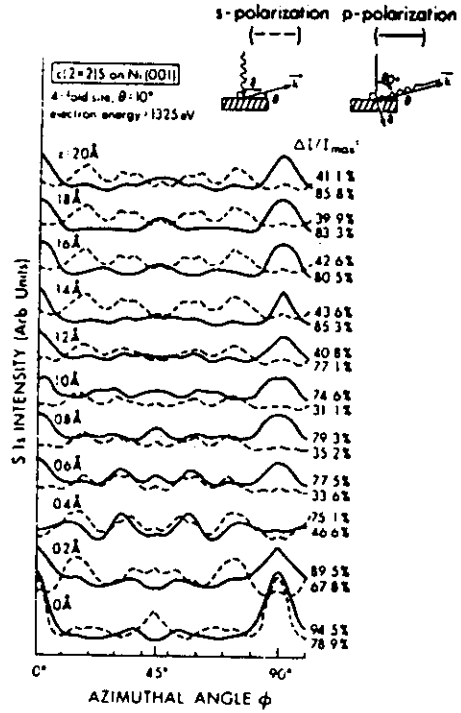

Fig. 52. The effect of changing from s- to p- polarization on azimuthal XPD. Theoretical curves for the azimuthal dependence of S2p intensity from c(2x2)S on Ni(001) at $\theta = 10°$ are shown for the two polarizations and a range of 4-fold-coordinate z values from 0.0Å to 2.0Å. (P. J. Orders and C. S. Fadley, unpublished results, plus new experimental and theoretical results in ref. 100.)

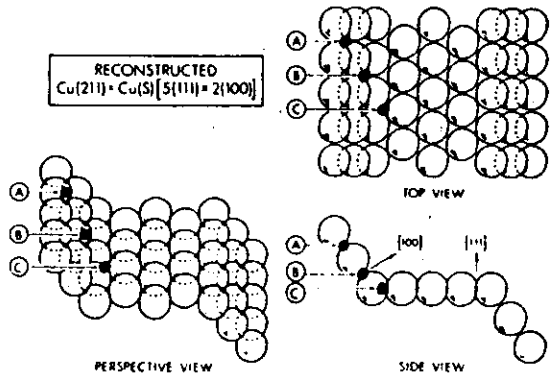

Fig. 53. Three views of a stepped Cu(211) surface as it is found to reconstruct under oxygen exposure. Included are the three possible high-symmetry coordination sites expected for oxygen bonding on or near the step faces: A = 4-fold top, B = 4-fold bottom, and C = 3-fold. (From Thompson, ref. (80).)

from (211) and (410) surfaces at different exposures.[80] In general, a mirror average of these two halves will give the best representation of the true XPD peaks, and that also is shown in Fig. 54. A full set of such mirror-averaged experimental data for six θ values between 7° and 23° is shown as dashed curves in Fig. 55, and it is clear that the diffraction features are very sensitive to polar angle as well. The anisotropies are as high as 31% for (211) and 40% for (410). The most reliable data range is for $10° \lesssim \theta \lesssim 20°$, as below this the count rates are much lower due to the instrument response function and possible residual roughness effects, and above it, the anisotropies are too low due to the large scattering angles required.

In order to next ask what the experimental data in Fig. 55 can tell us concerning the adsorption geometry, a series of SSC calculations was performed for various physically reasonable vertical positions z of oxygen in the different sites A, B and C of Fig. 53. Comparison of these theoretical curves with experiment showed that the B = 4-fold bottom site clearly gave the best fit to experiment, with A = 4-fold top being reasonably good as well, and C = 3-fold being very poor. Choosing the optimum z value for each site type proceeded via comparisons like Fig. 56 for the 4-fold bottom site at θ = 17°: it is clear here that a z distance of 0.4-0.6 Å above the centers of the Cu atoms in the step face gives the best fit to experiment. Overall use of all six θ values yields 0.6±0.2 Å as the best estimate, and the final theoretical curves for this value are summarized in Fig. 55. Although not all features are correctly predicted, especially as to relative intensity, the overall agreement in the structure-rich region for $\phi > 90°$ is very good, especially for the region $10° \lesssim \theta \lesssim 20°$ expected to be most reliable. The search and optimization procedure used thus strongly suggests a predominant 4-fold bottom adsorption site for this O exposure on Cu(211). A minority admixture of 4-fold top adsorption also is possible.

Having tentatively solved this structure it is also of interest to see whether any of the XPD features are capable of simple physical interpretation. In fact, the strong peaks seen near $\phi = 135°$ for $7° \leq \theta \leq 20°$ are all found to be due to forward scattering or 0th order diffraction from the two nearest-neighbor Cu atoms just above a B-site oxygen on the (100) step face (cf. Fig. 53). (The symmetry of the surface also dictates that similar peaks would arise in A-site emission as well, but they are found to be slightly shifted in position relative to experiment.) Also, the general dip in intensity seen at $\phi \gtrsim 100°$-120° is found to be due to enhanced inelastic scattering for emission through the step face at angles nearly parallel to it. The excellent agreement between experiment and theory for these simply explicable features thus further reinforces the 4-fold site assignment.

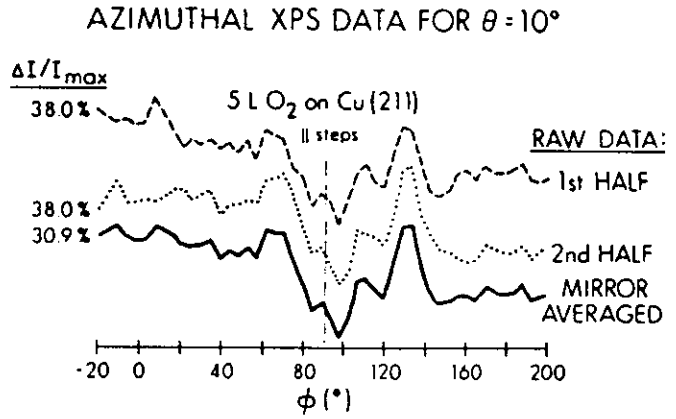

Fig. 54. Azimuthal XPD data for O1s emission from a 5L exposure of O_2 on a stepped Cu(211) surface. The mirror symmetry of the surface across a plane perpendicular to the steps is reflected in the excellent agreement between the two halves of the full 360° scan. The average of these two halves has been used for subsequent structural analysis. (Thompson, ref. (80).)

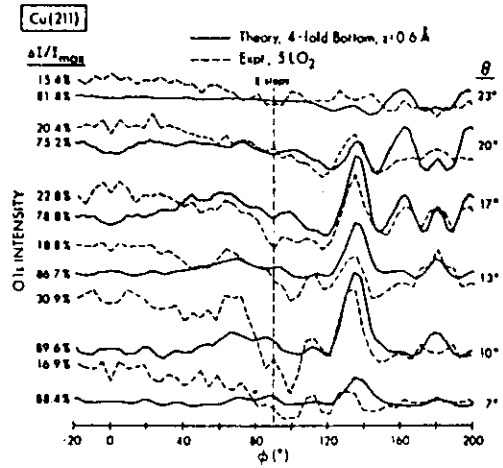

Fig. 55. Comparison of experiment and SSC theory for the data of Fig. 54, with experiment being shown here as dashed curves. The theoretical curves are for oxygen in all sites of type B in Fig. 53 and at a distance of 0.6Å above the first layer of Cu atoms on the step face; this geometry is found to optimize agreement with experiment.

It has thus been possible using this type of XPD analysis to tentatively suggest adsorption geometries for several exposures of O on Cu(211) and (410)[80]. More importantly, this work indicates that XPD may be able to provide unique structural information for this complex, yet chemically very important, class of surfaces about which rather little is known. Determination of adsorbate bonding geometries from LEED for such surfaces is a very difficult matter, for example, due to the much larger unit cells and relatively weaker substrate effects involved[101].

As a final and very recent example of the use of XPD in a surface-structural study, Kono and co-workers[102] investigated the ($\sqrt{3}\times\sqrt{3}$)R30° Ag overlayer on Si(111). They see strong XPD features in azimuthal scans of Ag3d intensity, and have made use of kinematical theory to propose a new structure for this overlayer. (See below.)

F. XPD Measurements Using Synchrotron Radiation

We have already noted in the last section that the use of polarized synchrotron radiation may permit enhancing the sensitivity of XPD to adsorbate site type and vertical position, and preliminary experiments of this type have recently been performed[100]. A further interesting question is whether it would be advantageous to be able to tune the radiation energy so as to have photoelectron energies either below or above those fixed by the usual XPS sources of $h\nu$ = 1.2-1.5 keV.

Going to lower kinetic energies of say 200-500 eV would have the advantage of yielding scattering factors less strongly forward peaked, and therefore possibly more substrate sensitivity in azimuthal scans. Also, a useful degree of anisotropy might persist up to higher θ values, thus avoiding the need for extremely small-angle grazing emission with its attendant low intensity and possible surface roughness problems. Possible problems at lower energies, however, are the need for a more complicated theoretical model involving multiple scattering (MS) effects. Very complex MS calculations are, for example, clearly necessary in the very low energy (~30-100 eV) adsorbate core-level photoelectron diffraction studies pioneered by Smith, Woodruff, Norman and co-workers[103]. A partial answer to these questions has been obtained in recent measurements by Orders et al.[100] They obtained Si 1s azimuthal scans from the well-defined c(2x2)S overlayer on Ni(001), tuning the x-ray radiation so as to sweep the photoelectron energy from 230 eV to 900 eV. Some of this experimental data for θ = 10° is shown as solid curves in Fig. 57, and it is clear that the XPD effects are very sensitive to photoelectron kinetic energy. This directly suggests the alternate possibility of fixing θ at some convenient value and making φ scans for various $h\nu$ values to build up a data set for structural determinations. Also shown in Fig. 57 are SSC curves for the known adsorbate geometry and the agreement between theory and experiment for all three energies is extremely good: all peaks are

Since the writing of this review, two additional aspects of XPD have been explored: (1) The use of near-neighbor forward scattering such as that in Figs. 40 and 41 in the analysis of epitaxial overlayer growth (W. F. Egelhoff, Phys. Rev., B30, 1052 (1984) - expt.; E. L. Bullock and C. S. Fadley, Phys. Rev., B31, 1212 (1985) - theory; and (2) The use of multiplet-split core levels to permit spin-polarized photoelectron diffraction studies of magnetic materials (B. Sinković and C. S. Fadley, Phys. Rev., B31, 4665 (1985) - theory; B. Sinković, B. Hermsmeier, and C. S. Fadley - expt., to be published, Phys. Rev. Lett. 55, 1227 (1985))

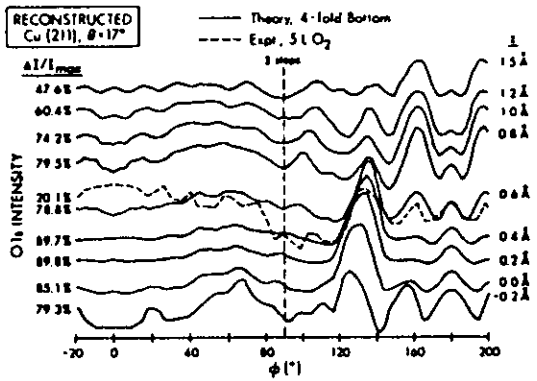

Fig. 56. Illustration of the sensitivity of the theoretical curves of Fig. 55 to the choice of z for the 4-fold bottom site. Calculations for different z values are compared to experiment for a θ = 17° emission angle.

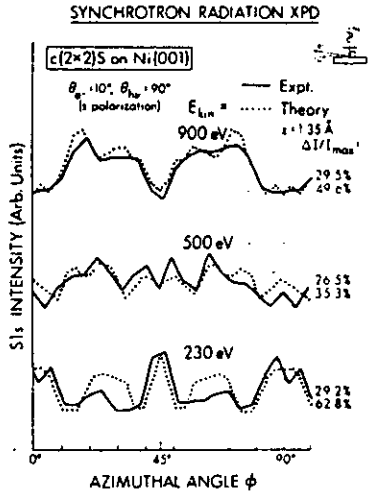

Fig. 57. Comparison of SSC theory to the results of the first azimuthal XPD experiments using synchrotron radiation for excitation. The system is again c(2x2)S on Ni(001), and photon energies have been chosen to yield electron kinetic energies of 900 eV, 500 eV, and 230 eV. The electron emission angle is θ = 10° and the radiation is s-polarized ($\hat{\varepsilon}$ is parallel to the surface). (From Orders et al., ref. (100).)

correctly predicted as to position, and generally also as to relative intensity, although a few deviations as to the latter are seen, especially at the lowest energy of 230 eV. Thus, the SSC model definitely seems useful down to a few hundred eV in energy, making this region a potentially very fruitful one for future XPD studies. A more detailed account of this study is in preparation[100].

On the opposite end of the energy scale, would higher photoelectron energies of say 10,000 eV be of any advantage? Scattering factors would be more sharply forward peaked (cf. Fig. 35) and a single-scattering approach probably more likely to be highly accurate. However, on the negative side, the total scattering cross sections would be lower and effects thus smaller, and angles even closer to grazing would be needed to see significant substrate scattering. Also, the smaller deBroglie wavelengths would lead to very fine features in the XPD patterns perhaps difficult to resolve.

A recent theoretical study by Thompson and Fadley[80] used SSC calculations to compare typical XPD effects at 1000 eV with those at 10,000 eV. The cases chosen for study were polar-scan intramolecular scattering in a vertically-oriented CO molecule with differing degrees of wagging vibration, and grazing emission azimuthal scans from c(2x2)O on Cu(001) at two z positions: in-plane at z = 0.0 Å and above plane at z = 1.0 Å. Some of these results are summarized in Figs. 58 and 59. In Fig. 58, the sharper intramolecular peak in a polar scan for 10,000 eV and no vibration (θ_{rms} = 0°) could permit more precisely determining the molecular orientation relative to a surface, but adding in a reasonable amount of vibration (θ_{rms} = 10°) quickly leads to comparable FWHM's for both energies, and an even lower anisotropy $\Delta I/I_{max}$ for 10,000 eV. The negative effect of the lowered total scattering cross section at 10,000 eV is also seen in the larger relative importance of the unscattered waves. In Fig. 59, the overall anisotropy $\Delta I/I_{max}$ in an O1s azimuthal scan is shown as a function of the polar angle at which the scan is made. The two energies and two adsorbate vertical positions are shown separately. These curves make it clear that for either in-plane or above-plane adsorption, the degree of anisotropy falls off much more rapidly with θ for 10,000 eV electrons, and that angles $\lesssim$5-10° would be necessary to see significant effects. For θ $\gtrsim$ 10°, almost no anisotropy is seen at 10,000 eV. This is a direct result of the additional peaking in the scattering factors at higher energy. The effects of increasing energy on the detailed form of the azimuthal XPD patterns is also considered elsewhere in detail[80]. Overall, however, it can be concluded that increasing kinetic energy markedly from the present XPD regime of 10^3 eV does not seem to provide any significant advantages for XPD work, even though going to lower energies does seem promising in several respects.

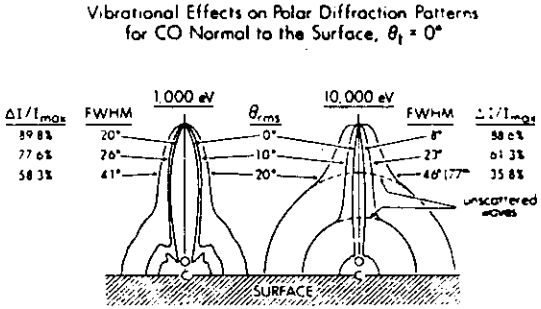

Fig. 58. Vibrational effects on C1s polar dependence in emission from CO oriented normal to a surface (θ_t = 0°) for two electron kinetic energies: 1,000 eV and 10,000 eV. Only the root-mean-squared angular displacement due to vibration is varied from 0° to 20°. (From Thompson, ref. (80).)

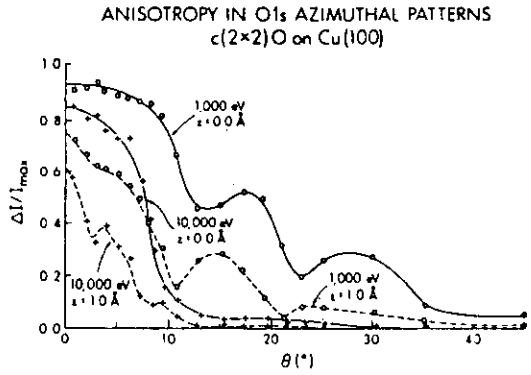

Fig. 59. Dependence of overall XPD anisotropy $\Delta I/I_{max}$ on emission angle θ, adsorbate z position, and electron kinetic energy for c(2x2)O on Cu(001). In general, increasing θ, moving the adsorbate from in-plane (z = 0.0Å) to above-plane (z = 1.0Å), or increasing energy from 1,000 eV to 10,000 eV tends to decrease the anisotropy. (From Thompson, ref. (80).)

G. Diffraction in core-level Auger emission

Inasmuch as Auger emission inevitably accompanies x-ray photoelectron excitation, and also can be produced very easily by other forms of bombardment, for example by electrons, it is of interest to ask whether similar kinds of Auger diffraction effects may arise in emission from a single crystal. For simplicity, we will concentrate on Auger energies in the 500-1500 eV XPS range and on transitions of the core-core-core type that are minimally influenced by chemical effects or valence-level complexities. (In fact, prior studies of the angular distributions of very low energy ($\lesssim$150 eV) core-valence-valence Auger electrons have proven to be rather difficult to interpret, even with the use of multiple-scattering theory[73,105].)

Fig. 28 due to Owari et al.[64] already contains some polar-scan substrate Auger data of this type for the Ge $L_3M_{4,5}M_{4,5}$ transition, which in this case has a kinetic energy of 1147 eV not very different from the Ge3d photoelectron peak at 1457 eV (the deBroglie wavelengths would have a ratio of 1.13, rather close to unity). Comparison of the observed XPD curves (a) and (b) for these two transitions reveals that they are very close in structure. Fig. 60 shows similar azimuthal-scan data due to Orders et al.[69] for adsorbate core-core-core Auger emission from c(2x2)Se on Ni(001). The Auger transition here is the same as that studied for Ge ($L_3M_{4,5}M_{4,5}$) and it has an energy of 1311 eV extremely close to the Se3p photoelectron peak at 1322 eV; the de Broglie wavelengths here are thus essentially identical. The five curves shown for different polar angles of emission are essentially identical for the Auger and photoelectron peaks. It thus seems clear that in the $\sim 10^3$ eV energy regime and for core-core-core transitions, the predominant source of such Auger anisotropies is final-state scattering and diffraction of exactly the same nature as that discussed in detail here for XPD. By implication, one would also thus expect a single-scattering theory to provide a reasonably good description of such Auger phenomena.

Because of the much different natures of the basic emission processes for photoelectrons and Auger electrons, it might at first sight seem difficult to understand why their overall diffraction effects should be essentially identical for emission at the same kinetic energy. This, however, is easily explained qualitatively in terms of the forward-peaked nature of the electron-atom scattering at these energies. That is, even though the basic Auger emission intensity will be essentially isotropic for a core-core-core transition, in contrast to the polarization-associated directionality of the photoelectron emission (cf. Fig. 34), in either case, it is only for initial emission rather close to the final observation direction $\hat{k}$ that the scattering can be significant enough to produce measureable diffraction effects. Thus, for most current XPS

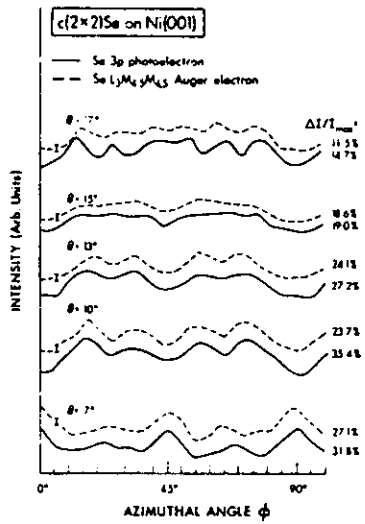

Fig. 60. Comparison of experimentally-observed diffraction effects in azimuthal scans of Se3p photoelectron- and $SeL_3M_{4,5}M_{4,5}$ Auger- emission from c(2x2)Se on Ni(001).

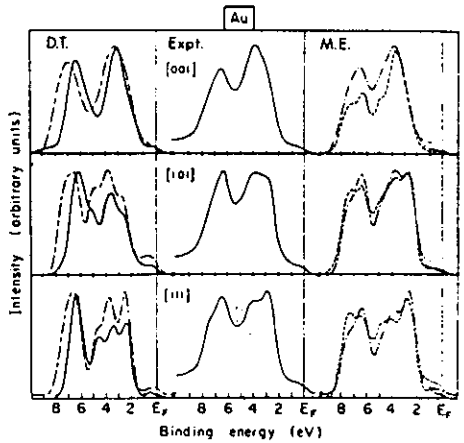

Fig. 61. Some early experimental and theoretical angle-resolved XPS valence spectra for single-crystal Au with electron emission along the [001], [101], and [111] directions. "D.T." represents calculations based upon the direct-transition model, and "M.E." calculations using the plane-wave matrix-element model. The two sets of theoretical curves in each case represent slightly different choices of the band structure used as a starting point (cf. refs. 6, 110, and 111).

experimental geometries, the variation of the primary emission intensity over the solid angle that is effective in producing the diffraction effects will be rather small; overall then, the XPD patterns should look very much like their isotropically-excited Auger counterparts, as is observed experimentally. However, for very special polarization geometries in XPS such as the p case shown in Fig. 51, one would expect the anisotropic character of the primary emission to be more important, and this should lead to inherent differences between photoelectron- and Auger- diffraction effects.

In any case, it is of considerable interest that Auger electrons exhibit effects completely analogous to those of XPD, and this suggests that future cross comparisons of the two types of data could be very useful in structure studies. The same sort of SSC model should also be valuable for interpreting Auger data, perhaps modified so as to assume isotropic initial emission simply by removing the $\hat{e}\cdot\hat{k}$ and $\hat{e}\cdot\hat{r}_j$ factors in Eq. (28).

H. Concluding remarks and comparison to other techniques

Overall then, XPD appears to have considerable potential as a surface structural tool, especially with expected improvements in angular resolution and intensity, as well as with the use of polarized, energy-tunable, synchrotron radiation for excitation. The fact that a very simple single scattering theory appears to describe these effects very well is also an advantage. Intra- and inter-molecular scattering effects can provide very direct and simply interpretable information on adsorbate structures, and similarly simple through-bond scattering has also been observed for adsorption on stepped surfaces. Azimuthal-scan data can also be analyzed by comparison to single-scattering theory so as to derive geometries with accuracies that can be as high as ± 0.1 Å, although for adsorbates situated well above the substrate surface ($\gtrsim 1.0$ Å), further improvements will be needed to achieve high positional accuracy. Analogous Auger diffraction effects at comparable energies of $\sim$500-1500 eV may also be useful for structural studies.

A brief comparison to some other currently used surface structural techniques is also worthwhile here. LEED[41,42] is certainly the most used method to date, but the accumulation of accurate I-V data is a difficult task (certainly of the same order as an XPD experiment) and the final analysis must then proceed via very complex multiple-scattering calculations. Also, rather long-range order over a region of $\gtrsim$100 Å in diameter is needed to do LEED, whereas XPD should require only very short range order, or, for certain effects, no long-range order at all beyond that in the substrate. Reflection high-energy electron diffraction (RHEED) with energies of $\sim 10^4$ eV and grazing incidence angles of $\sim 5°$[104] is also a close relative of both LEED (in general experimental geometry) and XPD (in using rather high

energies). However, to date only preliminary attempts have been made at deriving quantitative structural information from RHEED[104], even though it is very generally useful in a qualitative sense.

Angle-resolved UPS of valence levels has been shown to provide very useful structural information as well[7-9], but this must often rely on a rather complex theoretical analysis of the valence states involved. This analysis may also have to include the detailed matrix elements involved in the photoemission process, although in certain cases, symmetry-based selection rules can be used to semi-quantitatively derive structural information. Angle-resolved UPS of core levels (often referred to as "PhD" for photoelectron diffraction) attempts to do the same thing as XPD, but at much lower energies where a more complex multiple-scattering theory must be used[104]; here again long-range order is not necessary. In general, synchrotron radiation is necessary to fully exploit either form of ARUPS.

Two other diffraction-based techniques requiring synchrotron radiation are normal photoelectron diffraction (NPD)[11,106] (and the closely-related off-normal photoelectron diffraction[107]), as well as surface EXAFS or SEXAFS[98,108]. Neither of these require long-range adsorbate order. Both involve scans of photon energy, but NPD is experimentally more difficult in requiring that a certain core photoelectron peak intensity be monitored accurately throughout this scan; thus the monochromator flux and electron analyzer acceptance must be measured carefully at each $h\nu$, and Auger peaks also may cause interferences at certain $h\nu$ values. By contrast, detection can be much simplified in SEXAFS. NPD seems to require multiple-scattering calculations for comparison to experiment in order to derive adsorbate structures. Prior suggestions of the possibility of Fourier transforming NPD data to more easily derive distance information[11,106] do not seem to be fully quantitatively justifiable or useful[83]. By contrast, Fourier transformations of SEXAFS data are routinely used, with accuracies of $\sim\pm 0.05$ Å appearing to be possible. Thus, although each of these electron-based techniques has certain unique aspects as far as information context, it is also clear that each has certain limitations and/or practical problems of execution.

The use of intramolecular scattering in XPD has already been compared to deriving analogous bond-orientation information from electron stimulated desorption (ESDIAD)[90] and core-level absorption edge structure measurements[91] in Section 5.c.

Finally, other surface structural techniques involving, for example, different types of ion scattering and x-ray scattering have been reviewed recently by Eisenberger and Feldman[109]. It is again clear that each of these techniques has its advantages and disadvantages.

Overall, XPD thus appears to provide various types of structural information that should well complement these other methods and be of general utility in surface science.

6. VALENCE-LEVEL EMISSION FROM SINGLE CRYSTALS

A. Introduction

As the last major subject, we turn to angle-resolved XPS spectra from the valence levels of single-crystals. It was first noted by Baird et al.[110] that such angle-resolved valence spectra for Au exhibited significant changes with emission direction, and some of these earliest experimental results are shown in Fig. 61. For electron emission along the three low-index directions [001], [101], and [111], the relative intensities of the two main 5d-band components vary considerably, and there are also noticeable changes in the fine structure within these components. Such angular sensitivity has subsequently been observed in a number of systems encompassing both transition metals and semiconductors, including Ag[111], Cu[112], Pt[113], Si[114], MoS_2,[115] GaSe[115], and W[116]. It is thus clear that there may be no simple connection of a given single-crystal valence band spectrum with something as straightforward as the non-directional total density of electronic states, even though angle-integrated or polycrystalline XPS studies have previously been shown to be capable of deriving density-of-states information[6]. However, the angular dependence of such spectra may provide much more detailed kinds of information concerning the electronic states, and it is toward this end that two rather simple limiting theoretical models have been developed for interpreting such effects. Although much more general treatments of the photoemission process have been presented by several authors[117-119], these have not been applied to XPS in a quantitative way, and in fact, the higher energy of excitation (vis a vis UPS) makes certain simplifications readily possible. These two simplified models are introduced briefly below, and their likely limitations and domains of applicability are discussed. Comparisons of theory with illustrative experimental spectra are then given.

B. Simple theoretical models

(i) Introduction. A detailed treatment of angle-resolved XPS valence emission would require accurate wave functions for both the initial state and the final state, which involves a photoelectron at $\sim 10^3$ eV. Matrix elements between these two would then have to be evaluated. Although very accurate and complete methods for doing this have been discussed[117-119], it is convenient and adequate in discussing ARXPS to use as a starting point the simple one-electron, three-step model of photoemission. This model predicts the kinetic energy distribution just outside the surface to be given by:

$$N(E_{kin}) = N(E^f - V_0) = N(E^i + h\nu - V_0)$$
$$\propto \sum_{\substack{\text{Occ.}\\ \text{Bands}}} \int |\langle \phi_{\vec{k}^f}(E^f = E^i + h\nu)|\vec{A}\cdot\vec{\nabla}|\phi_{\vec{k}^i}(E^i)\rangle|^2 F(E^i) T(E^f, \vec{k}^f)$$
$$\times\ \delta(\vec{k}^f - \vec{k}^i - \vec{g} - \vec{k}_{h\nu}) d^3k^i \ ,$$

where E^f is the final energy of the excitation as measured inside the crystal, E^i is the initial energy from which excitation occurs, $\phi_{\vec{k}^f}$ is a final-state one-electron function corresponding to wave vector $\vec{k}^f$ and energy E^f, $\phi_{\vec{k}^i}$ is the initial-state one-electron function, $\vec{A}\cdot\vec{\nabla}$ is the relevant operator for the radiation, F(E) is the Fermi function ($\approx$ 1.0 for $E<E_{Fermi}$ and $\approx$ 0 for $E>E_{Fermi}$) and T is an escape function that could allow for inelastic scattering effects and internal reflection at the potential barrier V_0. Energy conservation is implied in setting $E^f = E^i + h\nu$. In XPS, the energies and mean free paths are high enough to assume that emission involves pure bulk states and to set T = 1.0 for all but grazing angles of emission (cf. Figs. 5 and 14). The sum is over all occupied bands and the integral over all initial wave vectors $\vec{k}^i$ inside the reduced Brillouin zone. The initial-state band-structure can thus be denoted $E^i(\vec{k}^i)$. The relevant one electron functions are assumed to be Bloch functions due to the full translational periodicity assumed for the crystal, so that the evaluation of the $\vec{A}\cdot\vec{\nabla}$ matrix directly results in a wave-vector conservation relation implied by the delta function:

$$\vec{k}^f = \vec{k}^i + \vec{g} + \vec{k}_{h\nu} \ . \qquad (33)$$

Here $\vec{k}^f$ is the final-state wave vector expressed in an extended zone scheme, $\vec{k}^i$ is the initial-state wave vector expressed in a reduced-zone scheme, $\vec{g}$ is a unique bulk reciprocal lattice vector connecting the two, and $\vec{k}_{h\nu}$ is the wave vector associated with the radiation. In general, $|\vec{k}_{h\nu}| = 2\pi/(\text{radiation wavelength})$. $\vec{k}_{h\nu}$ can be neglected with respect to reduced-zone dimensions in experiments at uv energies, but it cannot be in typical XPS measurements, as will be illustrated below for a specific example. Transitions satisfying Eq. (33) are termed direct transitions or wave-vector conserving transitions. Eqs. (32) and (33) thus implicitly assume long-range order, neglect surface effects except as a potential barrier which may produce refraction at lower takeoff angles, and do not include any consideration of vibrational effects (which can be considered to be the introduction of a type of positional disorder).

At very high energies of excitation such as those in XPS, a further approximation that seems reasonable is to assume a free-electron final state inside the crystal with momentum

$$\vec{p}^{f} = \hbar\vec{k}^{f} \tag{34}$$

and energy

$$E^{f} = E^{i} + h\nu = \frac{\hbar^2(k^f)^2}{2m} \tag{35}$$

The observed photoelectron just outside the surface would then have a momentum

$$\vec{p}^{f} = \hbar\vec{K}^{f} \tag{36}$$

and energy

$$E_{kin} = E^{f} - V_o = \frac{\hbar^2(K^f)^2}{2m} \quad , \tag{37}$$

with $\vec{K}^f$ being most simply related to $\vec{k}^f$ by refraction at the surface barrier V_o, as discussed previously in Sec. 3.C. An angle-resolved measurement of E_{kin} and the direction of emission thus determines $\vec{K}^f$, and, if V_o is known, $\vec{K}^f$ can then be used to derive $\vec{k}^f$ inside the crystal.

A further point first made by Shevchik[120] is that vibrational effects can effectively weaken the wave-vector conservation requirement in XPS and introduce a degree of averaging over the entire Brillouin zone such that all $\vec{k}^i$ points can be excited for all emission directions $\vec{k}^f \rightarrow \vec{K}^f$. Such phonon-induced non-direct transitions thus can be described in terms of Eq. (32) simply by removing the delta function so that the integral on $\vec{k}^i$ now can have non-zero contributions for all possible $\vec{k}^i$ values. Let us call this zone-averaged non-direct transition component of emission $N_{NDT}(E_{kin})$ and the direct-transition component as given by Eq. (32) without modification $N_{DT}(E_{kin})$. Since a direct transition can be viewed as a diffraction process, the observed strength of N_{DT} is furthermore reduced by vibrational effects according to a bulk temperature-dependent Debye-Waller factor W(T) as given by Eq. (27): the relevant $\Delta\vec{K}$ is here the reciprocal lattice vector $\vec{g}$. Then finally the total spectrum can be written as:

$$N_{tot}(E_{kin},T) = W(T)N_{DT}(E_{kin}) + [1-W(T)]N_{NDT}(E_{kin}) \quad , \tag{38}$$

from which it is clear that the Debye-Waller factor represents the fraction of transitions that are direct. Shevchik pointed out that the $\vec{g}$ vectors involved in XPS are sufficiently large that Debye-Waller factors of ~0.05-0.10 are not uncommon at room temperature, and thus that direct transitions might be very difficult to observe. Experiments with temperature variation also clearly may involve changes in the relative importances of the two component N_{DT} and N_{NDT}.

With this general background, we now discuss the two limiting models.

(ii) The direct-transition model. This model emphasizes the component N_{DT} of Eq. (38) (as calculated from Eq. (32)), and was first proposed by Baird, Wagner, and Fadley for interpreting angle-resolved XPS spectra[110]. Rigorous wave-vector conservation according to Eq. (33) is required for a transition to be allowed. The matrix elements $\langle\phi_{\vec{k}}^{f}|\vec{A}\cdot\vec{\nabla}|\phi_{\vec{k}}^{i}\rangle$ in Eq. (32) are also assumed to be constant for all allowed transitions, so that each transition is equally weighted in summing and integrating over the band structure $E_i(\vec{k}_i)$. The free-electron dispersion relation of Eq. (35) is also assumed, so that with Eq. (37) and perhaps an allowance for refraction at the surface, the observed energy and wave vector can finally be calculated. As noted previously in XPS, such refraction corrections will only be important for very low take-off angles $\lesssim 10°$, but in applying this same model at lower energies of ~40-160 eV they have been shown to become more important[121,122].

To illustrate the nature of $\vec{k}$ conservation for a typical XPS transition, Fig. 62 shows a scale drawing in $\vec{k}$ space of a possible direct transition in W involving photoelectron emission nearly along the [010] direction. The Brillouin zone radius is approximately $2\pi/a$, where a is the W lattice constant. MgKα radiation is assumed for excitation, leading to k^f values via Eq. (35) that range from $9.18(2\pi/a)$ for emission from the bottom of the 5d bands to $9.20(2\pi/a)$ for emission from the Fermi energy. Thus, the magnitude of $\vec{k}^f$ in XPS is very nearly constant over the full spectrum as judged against the Brillouin zone dimension within which $\vec{k}^i$ is eventually to be located, although this is not true in UPS. The finite solid angle cone of observation of the electron analyzer further distributes the observed $\vec{k}^f$ values over a disc-like region in $\vec{k}$-space: in Fig. 62, this is taken for illustration to be a cone of 1.5° half angle. $\vec{k}_{h\nu}$ will in this case be $0.32(2\pi/a)$ and thus clearly non-negligible with respect to Brillouin zone dimensions. Thus, its effect on wave vector conservation must be included. The effect of $\vec{k}_{h\nu}$ can be allowed for by shifting all points on the $\vec{k}^f$ disc of the observation cone by $-\vec{k}_{h\nu}$ as shown in Fig. 62. For an assumed angle of 48° between x-ray incidence and electron exit (a characteristic of the spectrometer geometry), this yields the right-hand shaded disc. This disc can then be projected back via one or more $\vec{g}$ vectors to yield $\vec{k}^i$ points within the zone from which emission can occur. The emission geometry here has been arbitrarily chosen so that the $\vec{k}^i$ set is centered along the x axis or [010] direction, and is shown as the left-hand shaded disc. Thus, the large value of $\vec{k}^f$ in XPS produces some degree of averaging in $\vec{k}^i$ via the finite disc sizes involved; in UPS by contrast very little averaging is produced by this effect. Also, this finite size in XPS may make it necessary to use different $\vec{g}$ vectors for different regions of the disc. Thus, this model finally predicts that an angle-resolved N_{DT} spectrum will be proportional to the

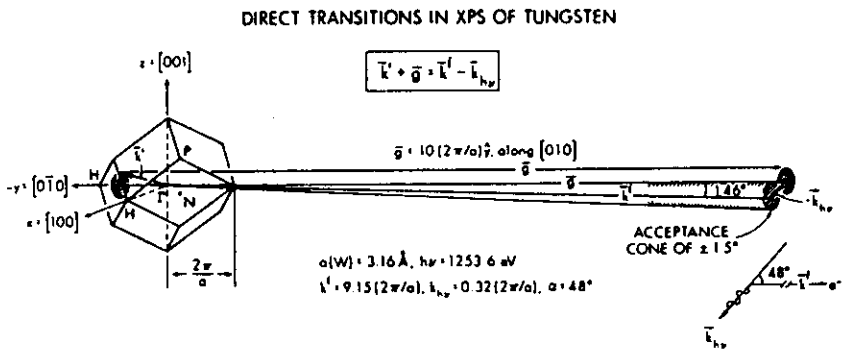

Fig. 62. Scale drawing in $\vec{k}$-space of the direct transitions that would be allowed for electron emission very nearly along the [010] direction from a W single crystal. An angle α of 48° between photon incidence and electron exit is assumed, together with an analyzer acceptance of ±1.5°. MgKα is used for excitation. The emission angle has been chosen so that $\vec{k}^f - \vec{k}_{h\nu} = \vec{k}^i + \vec{g}$ lies exactly along the [010] direction. The angular shift between $\vec{k}^f$ and $\vec{k}^f - \vec{k}_{h\nu}$ is 1.46°, as indicated. Those $\vec{k}^i$ values from which emission could occur will lie on the shaded disc inside of the Brillouin zone at left; the center of this disc lies ~5/8 of the way from Γ to H along the [0$\bar{1}$0] direction.

density of electronic states as computed over the allowed $\vec{k}^i$ region or disc, a quantity much different from the total density of states.

This direct-transition model was first shown to successfully describe normal emission angle-resolved UPS spectra from Cu at the lower energies of $40 \lesssim h\nu \lesssim 200$ eV by Wagner et al.[123], and it has subsequently also been used to map band structures of metals[121-125] and semiconductors[126] in both normal-[124,125] and off-normal[121,122,126] emission (where refraction may become important). Its utility in describing XPS spectra we discuss in the next section, but it is important to note that a Debye-Waller factor of too small magnitude would make direct-transition effects very difficult to see. In fact, for the example of Au in Fig. 61 at room temperature, W = 0.04, so that direct transition effects would certainly be very weak at that temperature; cooling Au to 4°K would by contrast yield approximately 65% direct transitions in Eq. (38).

(iii) The plane-wave matrix-element model. The second approach was first discussed in connection with XPS by McFeely et al.[111] Although Eq. (32) is again used as a starting point, it is here assumed that $\vec{k}$ conservation is somehow not an important selection rule, or equivalently that all $\vec{k}^i$ values in the zone can contribute to emission in a given $\vec{k}^f$ direction. The most likely source of this full $\vec{k}^i$ averaging is vibrational effects, as pointed out by Shevchik[120], but it was also originally suggested that final-state complexities due to electron scattering might cause such averaging as well[111]. In this limit of complete zone averaging, only the matrix elements of Eq. (32) remain as weighting factors of all of the occupied initial states to produce variations in spectra with direction. These matrix elements are further assumed to be calculable by using plane-wave or free-electron final states of the form $\phi_{\vec{k}^f}(\vec{r}) = \exp(i\vec{k}^f\cdot\vec{r})$, and tight-binding or LCAO initial states. The matrix elements then can be shown to have the form of linear combinations of Fourier transforms of atomic orbitals. There is also a further simplification in that the angular shape of the orbital in real space (for example, p_x or $d_{x^2-y^2}$) is preserved in the Fourier transform in $\vec{k}^f$ space (for example, a p_x orbital shows preferred emission along ±x, and a $d_{x^2-y^2}$ orbital along ±x,±y). Thus, information concerning the atomic-orbital makeup of a given set of levels is in principle derivable by analyzing the directionality of emission.

This plane-wave matrix-element model would not be expected to be useful at low energies where direct transitions are generally more important, and moreover the final states are expected to be much more complex than plane waves. In fact, the use of such matrix elements in Eq. (32) in an attempt to improve upon

direct-transition model calculations for Cu at ∿40-200 eV was found to markedly decrease agreement with experiment[123].

C. Comparisons of experiment and theory

Fig. 61 shows results of some of the earliest XPS studies of this type and compares XPS spectra for Au with emission along [001], [101], and [111] with theoretical curves generated by both the direct-transition (DT) and plane-wave matrix-element (ME) models[6,110,111]. Although the DT model predicts more change than is seen experimentally, both models qualitatively agree with the spectral variations seen experimentally. However, as already pointed out, the Debye-Waller factor for this case is only 0.04, so that the DT model is not appropriate for this particular case and its agreement with experiment must be viewed as fortuitous. However, Sayers and McFeely[127] and Goldberg et al.[25] have subsequently made more accurate matrix-element calculations relevant to zone-averaged tight-binding matrix-elements and they conclude that much of the ME agreement in Fig. 61 is fortuitious as well. Ley et al.[115] have however, been able to use this model in describing changes in angle-resolved XPS spectra from MoS_2, $GaSe_2$, and $SnSe_2$. Thus, it remains to fully resolve the degree to which the plane-wave matrix-element model can be used in XPS for systems where full zone averaging is expected.

A final important question is thus whether direct transitions can be observed at all in XPS, but this has been unambiguously resolved in the affirmative with recent studies by Hussain and co-workers[10,116]. The tungsten system chosen for study has an especially high Debye-Waller factor at room temperature: W = 0.55 at 300K. Thus ∿55% of the transitions at this temperature ought to be direct, and angle scans might be expected to produce spectral variations predictable by the direct-transition model. Also, raising the temperature would be expected according to Eq. (38) to reduce the effect of direct transitions, leading to more importance of zone-averaged matrix elements via N_{NDT}; thus, any significant change in spectra with temperature would be suggestive of direct transitions.

Fig. 63 shows a room-temperature azimuthal scan of W valence spectra at a polar angle of $\theta = 63.4°$ with respect to the (001)-oriented crystal surface; the azimuthal steps were 5°. The solid-curve experimental spectra show marked changes with angle, particularly as to the relative intensities of the components labelled 1-3. Component 1 at ∿4.8 eV below E_F in particular is very strong at $\phi = 0°$ and 45°, and very weak at $\phi \gtrsim 15°$. The dashed curves in the figure are based on the direct-transition model and make use of Eq. (38) with N_{NDT} taken to be the total density of states for W as a reasonable first approximation to this quantity that

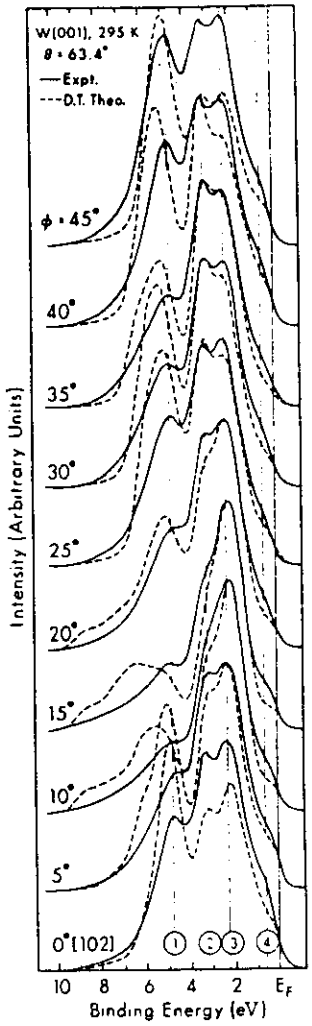

Fig. 63. Tungsten XPS valence-band spectra at T = 295°K for a 5°-step azimuthal scan from $\phi = 0°$ to 45° and a polar angle of 63.4°. Experimental curves (solid lines) are compared to theoretical curves (dashed lines) as calculated using Eq. (38), with $I_{NDT}(E)$ assumed to be proportional to the total density of states. (From. Hussain et al., ref. (116).)

is in any case not expected to change rapidly with direction. Even though this theory thus totally neglects matrix element effects in both N_{DT} and N_{NDT}, it correctly predicts all of the trends in relative intensity change found experimentally, including for example, the marked drop in importance of the 4.8 eV peak at $\phi \gtrsim 15°$. As a more quantitative indicator of the peak intensity changes with ϕ, Fig. 64 shows the ratio of the 4.8 eV peak to that at 2.3 eV for the azimuthal scan of Fig. 63 and another at θ=33°. Here again all of the experimental features are predicted by the direct-transition model, even if somewhat more dramatically than is actually observed. Some of the small discrepancies remaining are no doubt due to the neglect of matrix elements in the model. Similar agreement is found also for peak intensity ratios from polar scans of spectra[116].

A further important observation made in this work[116] is that the photon wave vector clearly influences the wave vector conservation in the manner expected. Fig. 65 overlays a pair of 2°-step symmetry-related polar scans around the [102] and [201] directions, and these would be superimposable with the [102] spectrum over that at [201] if $\vec{k}_{h\nu}$ were not significant. Including the effect of $\vec{k}_{h\nu}$ (as shown in the figure insets) produces a 4.0° shift in matching the two scans. This shift, together with a 0.6° refraction correction, yields an overall value of 4.6° in very good agreement with the 6.0° empirical shift needed to make the spectra optimally agree with one another. Without such a shift, the agreement is very poor, for example, the [102] and [201] spectra are very different.

The pronounced temperature dependence of W valence spectra also supports the presence of direct transitions in W near room temperature[116], as is shown in Fig. 66. Here, spectra obtained at two azimuths that are 6° apart for θ = 33° are shown as a function of temperature. At 295 K with a Debye-Waller factor of 0.55, the two spectra are very different, particularly as regards the 4.8 eV component, but they become essentially identical at 1000K where the Debye-Waller factor is down to 0.14. The marked difference at 295K suggests direct transitions, as zone-averaged matrix elements by themselves would not be expected to alter intensities that rapidly with ϕ. Conversely, the near identity of the spectra at 1000K is thus attributed to the slow variation of the now dominant zone-averaged matrix elements with direction.

Such temperature-dependent data can also be used to decompose spectra into their N_{DT} and N_{NDT} components[116], as Eq. (38) indicates that measurements of N_{tot} at any two temperatures, together with calculated W values at those temperatures, can be used to solve for N_{DT} and N_{NDT}. This is found to yield self-consistent decompositions into components for various spectra and various pairs of temperatures, as shown in Fig. 67. The direct-transition components so isolated

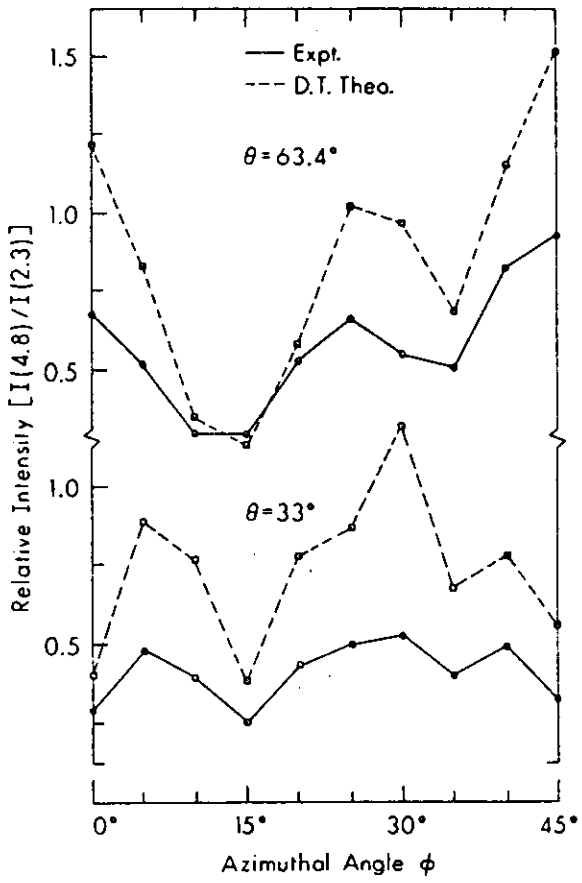

Fig. 64. Azimuthal dependence at T = 295°K of the relative intensity of the W valence-band peak at − 4.8 eV (cf. Fig. 63). The intensity of this peak is measured with respect to that at − 2.3 eV, and results are shown for polar angles of both 63.4° and 33°. Both experimental and direct-transition theoretical curves are shown. (From Hussain et al., ref. (116).)

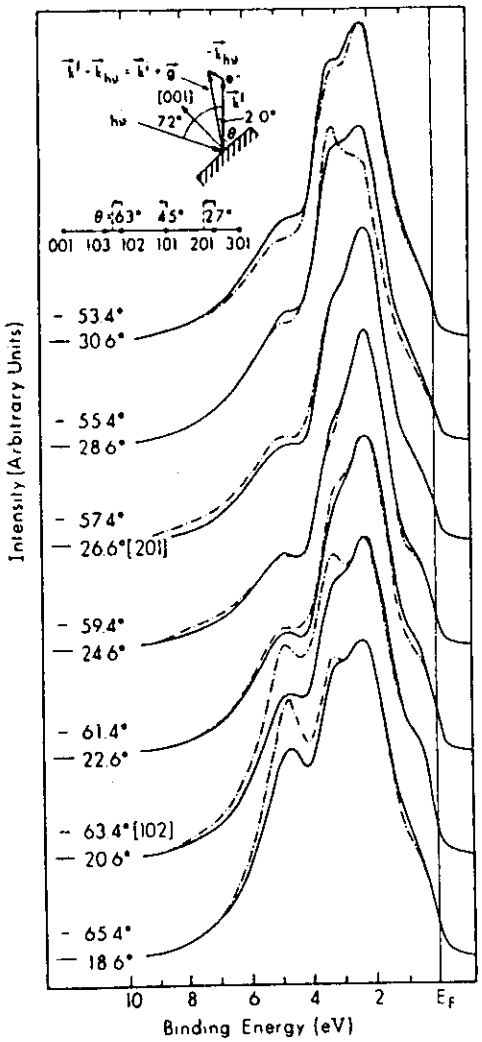

Fig. 65. Effect of photon wave vector $\vec{k}_{h\nu}$ on wave vector conservation in W valence-band emission at T = 295°K. A shift of 6.0° is needed in order to match spectra obtained at $\phi = 0°$ and various θ values near the symmetry-equivalent [201] and [102] directions; most of this shift is due to $k_{h\nu}$, as explained in the insets. (From Hussain et al., ref. (116).)

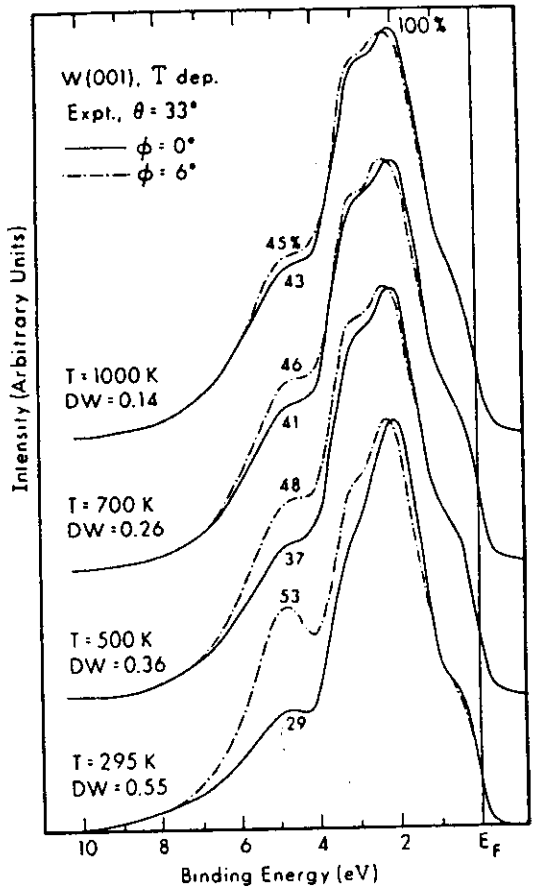

Fig. 66. Temperature dependence of W valence-band spectra for $\theta = 33°$ and emission along two azimuths separated by 6°. The temperatures and their associated Debye-Waller factors are also given, along with the relative intensity of the peak at ~ 4.8 eV (as measured in % of that at ~ 2.3 eV). (From Hussain et al., ref. (116).)

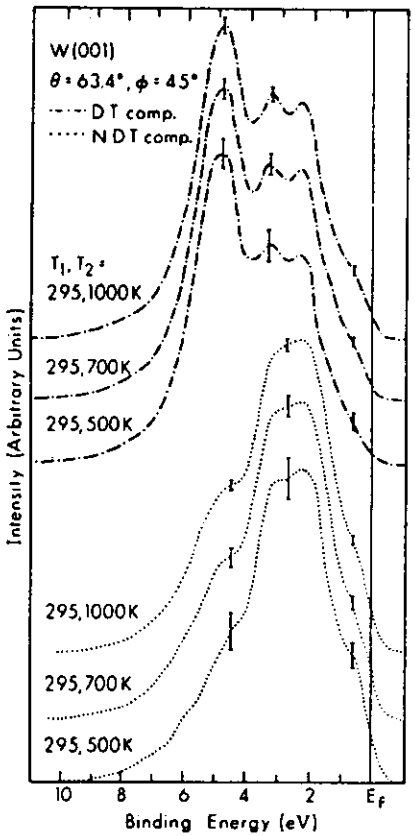

Fig. 67. Use of temperature-dependent W valence spectra to decompose measured intensities into their direct-transition and non-direct transition components with the use of Eq. (38). Different pairs of temperatures yield essentially the same results. (From Hussain et al., ref. (116).)

furthermore agree very well with pure direct-transition calculations of N_{DT} only. This method thus could be very useful in future band-mapping studies using XPS.

As a further example, Hussain et al.[10] have carried out the first swept-hν angle-resolved XPS study of valence spectra, again on tungsten to emphasize direct transition involvement. These measurements were done in normal emission from W (011) with monochromatized synchrotron radiation in the range 1100-1250 eV. Some of the results are shown in Fig. 68 together with direct transition calculations of the same type as those in Fig. 63. The agreement with experiment is thus excellent, especially with regard to the relative intensity change of the peak at ~4.8 eV, thereby providing more support for the applicability of the simple direct-transition model.

As a final point concerning the direct-transition model, one can ask why it works as well as it does and why, for example, complexities in the final state wave function do not cause significant deviations from it[111,128]. Such final-state complexities can be considered most simply as the mixing in of other plane-wave components $\exp(i(\vec{k}^f+\vec{g}')\cdot\vec{r})$ to an initial $\exp(i\vec{k}^f\cdot\vec{r})$ excitation via diffraction events associated with the reciprocal lattice vectors $\vec{g}'$. Here, $\vec{g}'$ is not the same as the $\vec{g}$ involved in the primary $\vec{k}$ conservation, but may be another bulk $\vec{g}$ vector or a vector associated with the reciprocal lattice of the surface. That such $\vec{g}'$ mixing events may be very weak in XPS is reasonable in view of the forward-peaked nature of the electron-atom scattering factors (cf. discussion of Sec. 5.B) that must be involved in producing such diffracted waves. An additional effect of possible importance is a smearing in $\vec{k}^f$ due to the inelastic scattering that effectively limits the wave function to a region of order Λ_e in size along its propagation direction[119]. Thus, the uncertainty principle dictates $\Delta k^f \Lambda_e \sim 1/2$ or $\Delta k \gtrsim 1/2\Lambda_e$ as a reasonable estimate of such smearing. That is, a $\vec{k}^f$ disc such as that in Fig. 62 will come to have an added thickness Δk^f along $\vec{k}^f$. However, for the specific example of W with a mean free path in XPS of ~13 Å, $\Delta k^f \gtrsim 0.02(2\pi/a)$, which is not very large compared to the Brillouin zone size as represented by $(2\pi/a)$. Direct calculations also verify that this much smearing along the propagation direction does not significantly alter the predicted XPS spectra,[116] even though such Δk^f effects appear to be important for understanding UPS spectra in the 40-200 eV region[122]. Thus neither of these two final-state complexities appears to be highly significant in describing XPS valence spectra.

D. Concluding remarks

In conclusion, although it may at first sight appear to be difficult to see direct-transition effects in the XPS spectra of many systems due to Debye-Waller

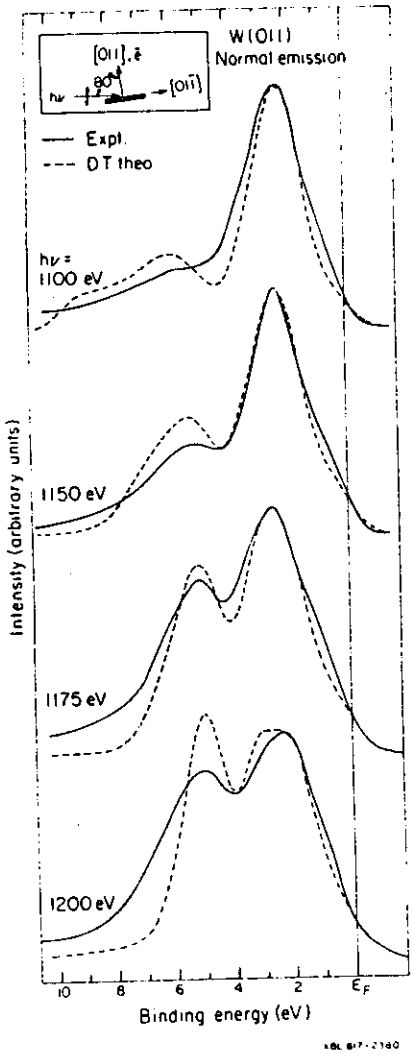

Fig. 68. Comparison of direct-transition theory to the first XPS valence-band experiments making use of tunable synchrotron radiation. Emission was normal to a W(011) surface; the geometry is shown as an inset. (From Hussain et al., ref. (10).)

attenuation, the inherent simplicity of the theoretical model which describes such effects at high energies of emission makes such measurements very appealing for band-structure studies. In fact, with the possible use of cryogenic cooling to increase W (see table of representative values for different elements in ref. 116) and multi-temperature measurements to permit isolating the direct-transition component, it should be possible to expand the range of systems that could be studied in this way. Using synchrotron radiation at lower energies of $\sim$ 200-400 eV would also reduce $|\vec{g}|$ and thus increase W while at the same time probably retaining the desired theoretical simplicity. Also, decreasing the angular acceptance of the analyzer would be very beneficial in reducing the size of the disc over which $\vec{k}^i$ is averaged, thereby providing more precise band mapping information.

To provide some indication as to how much increased angular resolution might affect such spectra, Fig. 69 shows recent direct-transition theoretical curves by Hussain and Fadley[129] for several very close-lying emission directions above a W (001) surface at two different angular apertures: ±1.5° and ±3.0° (at about which all prior XPS experiments have been carried out). It is clear that the ±1.5° curves are much more sensitive than the ±3.0° curves to small changes in emission direction. The ±3.0° curves are expected to show a greater degree of zone averaging, and this is borne out by the fact that at least some non-zero direct-transition intensity is predicted over the entire valence band region from 0-7 eV for all of the angles shown. By contrast, the ±1.5° curves exhibit greater differences, sharper features, and regions of zero predicted intensity (e.g., at $\sim$3 eV for θ = 56° and 57°). Furthermore, an analysis of these calculations shows that the ±1.5 curves for certain angles directly reflect that the $\vec{k}^i$ disc is centered very near a high-symmetry Brillouin zone point. For example, for θ = 53°, the disc center is near N and the 3-peaked structure reflects the 3 bands there[130], whereas for θ = 56°, 57°, the disc is near H where only a single low-lying band lies below the Fermi level[130]. The positions of the major peaks noted at these angles also correlate very well with band positions. Thus, for the first time, it is possible to predict that high-angular-resolution XPS can provide detailed point-by-point mapping of band structures. Recent experiments on W in our laboratory at a ±1.5° resolution[131] also confirm this enhanced sensitivity to angle, and the results are also consistent with direct-transition theory.

Finally, it would certainly be of interest from a theoretical point of view to further explore the calculation of the relevant $\vec{A}\cdot\vec{\nabla}$ matrix elements involved in such studies, as a fully accurate treatment of either direct transitions or zone-averaged non-direct transitions requires accounting for them and it is at present unclear as to whether a simple model can be reliably used to include them.

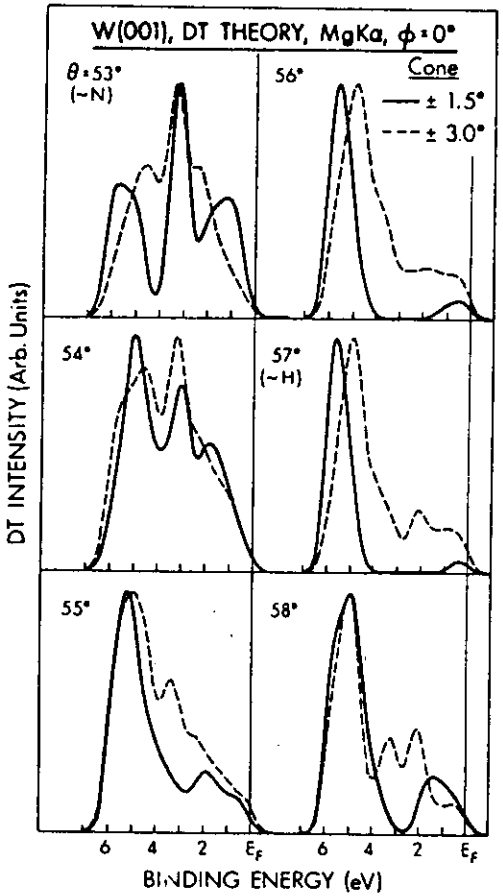

Fig. 69. The effect of increased angular resolution on the direct-transition component of W valence-band emission. Pure direct-transition theoretical curves are compared for a ±3.0° analyzer acceptance (dashed curves) and for a ±1.5° acceptance (solid curves). ϕ is fixed at 0° and θ is scanned in 1°-steps from 53° to 58°. For θ = 53° and 57°, the discs of allowed $\vec{k}_i$ points are very close to the N and H points in the Brillouin zone, respectively, as indicated (cf. Fig. 62).

As a final comparison to the closely-related use of angle-resolved UPS to study valence levels[7-9], it is clear that this technique has contributed very much to our understanding of both bulk- and surface- electronic structure. In general, it can be carried out at higher resolutions than ARXPS (~0.2-0.3 eV in UPS compared to ~0.5-1.0 eV in XPS), and both phonon effects and $\vec{k}$ smearing due to the finite analyzer acceptance core are much less as problems due to the much smaller energies involved. However, a detailed analysis of ARUPS data may require knowledge of both the initial- and final- state band structures, as well as a proper inclusion of both matrix elements and multiple-scattering effects. In ARXPS, by contrast, a very simple theory seems to describe the data very well, at least as far as the direct transition component is concerned. Thus, it seems that ARXPS will serve as a very useful complement to ARUPS, especially in bulk band structure studies.

Acknowledgements

In connection with those aspects of this review involving work at the University of Hawaii, the author is very much indebted to his several colleagues for their considerable contributions to the development of angle-resolved x-ray photoelectron spectroscopy. This group includes R. J. Baird, S. M. Goldberg, Z. Hussain, P. F. Heden, S. Kono, P. J. Orders, L.-G. Petersson, K. A. Thompson, and L. F. Wagner. Many helpful comments from B. L. Henke are also appreciated. The support of the National Science Foundation, the Petroleum Research Fund, and N.A.T.O. is also gratefully acknowledged. The hospitality of the Department of Physics, Montana State University during a portion of the writing of this manuscript is also very much appreciated. The author is also grateful to E. A. Stern for some very helpful comments concerning EXAFS theory and its relationship to XPD.

References

1. J. Jenkin, J. Elect. Spect., 23, 187 (1981).
2. K. Siegbahn, U. Gelius, H. Siegbahn, and E. Olsen, Phys. Lett., 32A, 221 (1970).
3. C. S. Fadley and S. A. L. Bergstrom, Phys. Lett., 35A, 375 (1971); and in Electron Spectroscopy, D. A. Shirley, ed., North Holland, Amsterdam (1972), p. 233.
4. C. S. Fadley, R. J. Baird, W. Siekhaus, T. Novakov, and S. A. L. Bergstrom, review in J. Elect. Spect., 4, 93 (1974).
5. C. S. Fadley, review in Prog. in Sol. St. Chem., G. A. Samorjai and J. O. McCaldin, eds., Pergamon Press, New York (1976), Vol. 11, p. 265.
6. C. S. Fadley, review in Electron Spectroscopy: Theory, Techniques, and Applications, C. R. Brundle and A.D. Baker, eds., Academic Press, London (1978), Vol. 2, Ch. 1.
7. B. Feuerbacher, B. Fitton, and R. F. Willis, eds., Photoemission and the Electronic Properties of Surfaces, Wiley, New York (1978).
8. M. Cardona and L. Ley, eds., Photoemission in Solids, Springer-Verlag, Berlin (1978), Vols. 1 and 2.
9. E. W. Plummer and W. Eberhardt, review in Adv. in Chem. Phys., L. Prigogine and S. A. Rice, eds., John Wiley, New York (1982), Vol. XLIX, p. 533.
10. Z. Hussain, E. Umbach, J. J. Barton, J. G. Tobin, and D. A. Shirley, Phys. Rev., B 25, 672 (1982).
11. S. D. Kevan, D. H. Rosenblatt, D. Denley, B.-C. Lu, and D. A. Shirley, Phys. Rev., B 20, 4133 (1979); Z. Hussain, D. A. Shirley, C. H. Li, and S. Y. Tong, Proc. Nat. Acad. Sci. (U.S.A.), 78, 5293 (1981).
12. R. J. Baird and C. S. Fadley, J. Elect. Spect., 11, 39 (1977).
13. E. W. Plummer, Nucl. Inst. and Meth., 177, 179 (1980).
14. N. V. Smith, in Photoemission in Solids, M. Cardona and L. Ley, eds., Springer-Verlag, Berlin (1978), Ch. 6.; N. V. Smith, P. K. Larsen, and M. M. Traum, Rev. Sci. Inst., 48, 454 (1977).
15. R. Z. Bachrach, S. B. M. Hagstrom, and F. C. Brown, in Vacuum Ultraviolet Radiation Physics, E. E. Koch, R. Haensel, and C. Kunz, eds., Pergamon, London (1974), p. 795; G. V. Hansson, B. Goldberg, and R. Z. Bachrach, Rev. Sci. Inst., 52, 517 (1981).
16. C. J. Powell, Surf. Sci., 44, 29 (1974).
17. I. Lindau and W. E. Spicer, J. Elect. Spect., 3, 409 (1974).
18. M. P. Seah and D. P. Dench, Surf. Int. Anal., I, 2 (1979).
19. J. M. Hill, D. G. Royce, C. S. Fadley, L. F. Wagner, and F. J. Grunthaner, Chem. Phys. Lett., 44, 225 (1976).
20. R. P. Vasquez, J. D. Klein, J. J. Barton, and F. J. Grunthaner, J. Elect. Spect., 23, 63 (1981).
21. B. L. Henke, Phys. Rev., A 6, 94 (1972).
22. W. A. Fraser, J. V. Florio, W. N. Delgass, and W. D. Robertson, Surf. Sci., 36, 661 (1973).
23. J. H. Scofield, J. Elect. Spect., 8, 129 (1976).
24. R. F. Rielman, Alfred Msezone, and S. T. Manson, J. Elect. Spect., 8, 389 (1976).
25. S. M. Goldberg, C. S. Fadley, and S. Kono, J. Elect. Spect., 21, 285 (1981); Solid State Commun., 28, 459 (1978).
26. D. R. Penn, J. Elect. Spect., 9, 29 (1976) and J. Vac. Sci. Tech., 13, 221 (1976).
27. V. I. Nefedov, N. P. Sergushin, I. M. Band, and M. B. Trzhaskowskaya, J. Elect. Spect., 2, 383 (1973).
28. W. J. Carter, G. K. Schweitzer, and T. A. Carlson, J. Elect. Spect., 5, 827 (1974); T. A. Carlson, Surf. and Int. Anal., 4, 125 (1982).

29. C. J. Powell and P. E. Larson, Appl. Surf. Sci., 1, 186 (1977).
30. D. T. Clark and H. R. Thomas, J. Polym. Sci. (Polym. Chem, Ed.), 15, 1093 (1977).
31. C. S. Fadley, J. Elect. Spect., 5, 725 (1974).
32. J. Brunner and H. Zogg, J. Elect. Spect., 5, 911 (1977).
*33. R. E. Connelly, M.S. Thesis, Univ. of Hawaii (1982); and R. E. Connelly and C. S. Fadley, to be published.
34. G. Hollinger and M. Pijolat, Surf. Sci., 105, 114 (1981); and M. Pijolat, doctoral thesis, Univ. Claude Bernard, Lyon, France (1980).
35. R. P. Vasquez and F. J. Grunthaner, Surf. Sci., 99, 681 (1980), and references therein.
36. D. T. Clark and H. R. Thomas, J. Polym. Sci. (Polym. Chem., Ed.), 15, 2843 (1977).
37. R. J. Baird, Ph.D. thesis, Univ. of Hawaii (1977).
38. R. J. Baird, C.S.Fadley, S. Kawamoto, and M. Mehta, Chem. Phys. Lett., 34, 49 (1975).
39. R. J. Baird, C. S. Fadley, S. Kawamoto, M. Mehta, R. Alvarez, and J. A. Silva, Anal. Chem., 48, 843 (1976).
40. O. A. Baschenko and V. I. Nefedov, J. Elect. Spect., 17, 405 (1979); 21, 153 (1980); and 26, 109 (1982).
41. J. B. Pendry, Low Energy Electron Diffraction, Academic Press, London (1974).
42. M. A. Van Hove and S. Y. Tong, Surface Crystallography by LEED, Springer-Verlag, New York (1979).
43. M. F. Ebel and W. Liebe, J. Elect. Spect., 16, 463 (1979).
44. J. C. Ashley and V. E. Anderson, J. Elect. Spect., 24, 127 (1981) and IEEE Trans. on Nucl. Sci., NS-28, 4132 (1981).
45. J. E. Demuth, D. W. Jepsen, and P. M. Marcus, Phys. Rev. Lett., 32, 1182 (1974); D. H. Rosenblatt et al., Phys. Rev., B 23, 3828 (1981); S. Brennan, J. Stöhr, and R. Jaeger, Phys. Rev., B 24, 4871 (1981).
46. M. Aono, C. Oshima, T. Tanaka, E. Bannai, and S. Kawai, J. Appl. Phys., 49, 2761 (1978).
47. A. Jablonski, Adv. in Coll. and Int. Sci., 8, 213 (1977).
48. V. I. Nefedov, P. P. Pozdeyev, V. F. Dorfman, and B. N. Pypkin, Surf. and Int. Anal., 2, 26 (1980).
49. W. N. Delgass, G. L. Haller, and J. H. Lunsford, Spectroscopy in Heterogeneous Catalysis, Academic Press, New York (1979), Ch. 8; P. J. Angevine, J. C. Vartuli, and W. N. Delgass, Proc. 6th Int. Cong. Catal., London, 1976, 2, 611 (1977).
50. J. Finster, P. Lorenz, and A. Meisel, Surf. and Int. Anal., 1, 179 (1979).
51. P. H. Citrin and G. K. Wertheim, Phys. Rev. Lett., 41, 1425 (1978).
52. T. M. Duc, C. Guillot, Y. Lassailly, J. Lecante, Y. Jugnet, and J. C. Vedrine, Phys. Rev. Lett., 43, 789 (1979); J. F. van der Veen, F. J. Himpsel, and D. E. Eastman, Phys. Rev. Lett., 44, 189 (1980).
53. G. K. Wertheim and G. Crecelius, Phys. Rev. Lett., 40, 813 (1978).
54. R. Haydock and M. J. Kelly, Surf. Sci., 38, 139 (1973); M. C. Dejonqueres and M. Cyrot-Lackmann, Surf. Sci., 53, 429 (1975); K. S. Sohn, D. G. Dempsey, L. Kleinmann, and E. Caruthers, Phys. Rev., B 13, 1515 (1976); B 14, 3185, 3193 (1976).
55. M. Mehta and C. S. Fadley, Phys. Rev. Lett., 39, 1569 (1977); Phys. Rev., B 20, 2280 (1979).
56. D. G. Dempsey and L. Kleinman, private communication.
57. R. J. Baird, C. S. Fadley, S. M. Goldberg, P. J. Feibelman, and M. Sunjic, Surf. Sci., 72, 495 (1978).
58. A. B. Bradshaw, W. Domcke, and L. S. Cederbaum, Phys. Rev., B 16, 1480 (1977).

---

* Now appearing as:

33. R. E. Connelly, C. S. Fadley, and P. J. Orders, J. Vac. Sci. Tech., A2, 1333 (1984).

59. M. Mehta and C. S. Fadley, Phys. Lett., A55, 59 (1975).
60. M. Mehta and C. S. Fadley, unpublished results.
61. M. Mehta and C. S. Fadley, Chem. Phys. Lett., 46, 225 (1977).
62. S. Kono, S. M. Goldberg, N. F. T. Hall, and C. S. Fadley, Phys. Rev. Lett., 41, 1831 (1978); L.-G. Petersson, S. Kono, N. F. T. Hall, C. S. Fadley, and J. B. Pendry, Phys. Rev. Lett., 42,1545 (1979).
63. S. Kono, S. M. Goldberg, N. F. T. Hall, and C. S. Fadley, Phys. Rev., B 22, 6085 (1980).
64. M. Owari, M. Kudo, Y. Nihei, and H. Kamada, J. Elect. Spect., 21, 131 (1981).
65. R. J. Baird, C. S. Fadley, and L. F. Wagner, Phys. Rev., B 15, 666 (1977).
66. J. M. Adams, S. Evans, J. M. Thomas, J. Am. Chem. Soc., 100, 3260 (1978); S. Evans, E. Raftery, and J. M. Thomas, Surf. Sci., 89, 64 (1979).
67. N. Koshizaki, M. Kudo, M. Owari, Y. Nihei, and H. Kamada, Jap. J. Appl. Phys., 19, L349 (1980).
68. A. Liebsch, Phys. Rev. Lett., 32, 1203 (1974); Phys. Rev., B 13, 544 (1976).
69. P. J. Orders, R. E. Connelly, N. F. T. Hall, and C. S. Fadley, Phys. Rev., B 24, 6163 (1981).
70. R. N. Lindsay, C. G. Kinnibergh, and J. B. Pendry, J. Elect. Spect., 15, 157 (1979).
71. T. Fujikawa, J. Phys. Soc. Jap., 50, 1321 (1981); 51, 251 (1982); and J. Elect. Spect., 26, 79 (1982).
72. P. A. Lee, Phys. Rev., B 13, 5261 (1976).
73. P. A. Lee and G. Beni, Phys. Rev., B 15, 2862 (1977).
74. L. McDonnell, D. P. Woodruff, and B. W. Holland, Surf. Sci., 51, 249 (1975).
75. Z. Hussain and D. A. Shirley, NPD results for sulfur s- and p- emission to be published. (Cf. also ref. 107.)
76. P. A. Lee and J. B. Pendry, Phys. Rev., B 11, 2795 (1975).
77. L.-G. Petersson, S. Kono, N. F. T. Hall, C. S. Fadley, and J. B. Pendry, Phys. Rev. Lett., 42, 1545 (1979).
78. L. I. Schiff, Quantum Mechanics, McGraw-Hill, New York (1968), pp. 136-137 and 324-325.
79. M. Fink and A. C. Yates, At. Data, 1, 385 (1970); M. Fink and J. Ingram, At. Data, 4, 129 (1972).
*80. K. A. Thompson, Ph.D. Thesis, Univ. of Hawaii (1981); K. A. Thompson and C. S. Fadley, to be published.
81. P. J. Orders, S. Kono, C. S. Fadley, R. Trehan, and J. T. Lloyd, Surf. Sci., 119, 371 (1982).
82. B. K. Teo and P. A. Lee, J. Am. Chem. Soc., 101, 2815 (1979).
*83. P. J. Orders and C. S. Fadley, Phys. Rev., B, to appear.
84. P. J. Orders, J. T. Lloyd, and C. S. Fadley, unpublished results for substrate Ni azimuthal XPD.
85. S. Kono, Hyomen Kagaku (Surface Science), 2, 153 (1981).
86. S. Takahashi, S. Kono, H. Sakurai, and T. Sagawa, J. Phys. Soc. Jap., 51, 3296 (1982).
*87. M. Owari, M. Kudo, Y. Nihei, and H. Kamada; and Y. Nihei, M. Owari, M. Kudo, and H. Kamada, papers presented at the 9th Int. Conf. on Atomic Spectroscopy/XXII Colloquium Spectroscopicum Internationale, Sept. 1981, Tokyo, Japan.
88. S. M. Goldberg, R. J.Baird, S. Kono, N. F. T. Hall, and C. S. Fadley, J. Elect. Spect., 21, 1 (1980).
89. M. Kudo, M. Owari, Y. Nihei, Y. Gohshi, H. Kamada, Jap. J. Appl. Phys., 17, Supp. 17-2, 275 (1978).

---

* Now appearing as:

80. K. A. Thompson and C. S. Fadley, J. Elect. Spect., 33, 29 (1984), and Surf. Sci., 146, 231 (1984).

83. P. J. Orders and C. S. Fadley, Phys. Rev., B27, 781 (1983); E. L. Bullock, C. S. Fadley, and P. J. Orders, Phys. Rev., B28, 4867 (1983); M. Sagurton, E. L. Bullock, and C. S. Fadley, Phys. Rev., B30, 7332 (1984).

87. M. Owari et al., J. Elect. Spect., 34, 215 (1984).

90. T. E. Madey, Surf. Sci., 79, 575 (1979) plus earlier references therein.
91. J. Stohr, K. Baberschke, R. Jaeger, R. Treichler, and S. Brennan, Phys. Rev. Lett., 47, 381 (1981).
92. L.-G. Petersson, S. Kono, N. F. T. Hall, S. Goldberg, J. T. Lloyd, and C. S. Fadley, Mat. Sci. and Eng., 42, 111 (1980).
93. D. H. Rosenblatt, J. G. Tobin, M. G. Mason, R. F. Davis, S. D. Kevan, D. A. Shirley, C. H. Li, and S. Y. Tong, Phys. Rev., B 23, 3828 (1981); D. A. Shirley, private communication.
94. J. H. Onuferko and D. P. Woodruff, Surf. Sci., 95, 555 (1980) and references therein.
95. B. J. Garrison, N. Winograd, and D. E. Harrison, Phys. Rev., B 18, 6000 (1978); S. P. Holland, B. J. Garrison, and N. Winograd, Phys. Rev. Lett., 43, 220 (1979).
96. T. S. Rahman, J. E. Black, and D. L. Mills, Phys. Rev. Lett., 46, 1469 (1981) and references therein.
97. D. H. Rosenblatt, J. G. Tobin, M. G. Mason, R. F. Davis, S. D. Kevan, and D. A. Shirley, private communication.
98. J. Stohr, R. Jaeger, and T. Kendelewicz, Phys. Rev. Lett., 49, 142 (1982) and references therein.
99. N. F. T. Hall, Ph.D. Thesis, Univ. of Hawaii (1982); N. F. T. Hall and C. S. Fadley, to be published.
*100. P. J. Orders, C. S. Fadley, R. Trehan, B. Sinkovic, Z. Hussain, and J. Lecante, to be published.
101. D. W. Jepsen, Phys. Rev., B 22, 5701 (1980) and references therein.
102. S. Kono, H. Sakurai, K. Higashiyama, and T.Sagawa, Surf. Sci., to appear.
103. D. P. Woodruff, D. Norman, B. W. Holland, N. V. Smith, H. H. Farrell, and M. M. Traum, Phys. Rev. Lett., 41, 1130 (1978); N. V. Smith, H. H. Farrell, M. M. Traum, D. P. Woodruff, D. Norman, M. S. Woolfson, and B. W. Holland, Phys. Rev., B 21, 3119 (1980); H. H. Farrell, M. M. Traum, N. V. Smith, W. A. Royer, D. P. Woodruff, and P. D. Johnson, Surf. Sci., 102, 527 (1981); W. M. Kang et al., Phys. Rev. Lett., 47, 931 (1981).
104. T. Matsudaira, N. Nishijima, and M. Onchi, Surf. Sci., 61, 651 (1976); D. Aberdam, R. Baudoing, E. Blanc, and C. Gaubert, Surf. Sci., 71, 279 (1978).
105. J. L. Beeby, Surf. Sci., 80, 55 (1979); S. Holloway, Surf. Sci., 80, 62 (1979); P. A. Maksym and J. L. Beeby, Surf. Sci., 110, 423 (1981).
106. S. D. Kevan, R. F. Davis, D. H. Rosenblatt, J. G. Tobin, M. G. Mason, D. A. Shirley, C. H. Li, and S. Y. Tong, Phys. Rev. Lett., 46, 1629 (1981) and references therein; S. Y. Tong and J. C. Tang, Phys. Rev., B 25, 6526 (1982).
*107. D. H. Rosenblatt, S. D. Kevan, J. G. Tobin, R. F. Davis, M. G. Mason, D. A. Shirley, J. C. Tang, and S. Y. Tong, Phys. Rev.,B 26, 3181 (1982).
108. P. H. Citrin, P. Eisenberger, and R. C. Hewitt, Phys. Rev. Lett., 41, 309 (1978); 45, 1948 (1980); S. Brennan, J. Stohr, and R. Jaeger, Phys. Rev., B 24, 4871 (1981); and references therein.
109. P. Eisenberger and L. C. Feldman, Science, 214, 300 (1981).
110. C. S. Fadley, Far. Soc. Disc., 60, 18 (1975); R. J. Baird, C. S. Fadley, and L. F. Wagner, Phys. Rev. Lett., 37, 111 (1976).
111. F. R. McFeely, J. Stohr, G. Apai, P. S. Wehner, and D. A. Shirley, Phys. Rev., B 14, 3273 (1976).
112. L. F.Wagner, Z. Hussain, C. S. Fadley, and R. J. Baird, Solid State Commun., 21, 453 (1977); G. Apai, J. Stohr, R. S. Williams, S. P. Kowalczyk, and D. A. Shirley, Phys. Rev., B 15, 584 (1977).

---

* Now appearing as:

100. B. Sinkovic et al., Phys. Rev., B30, 1833 (1984); P. J. Orders et al., Phys. Rev. B30, 1838 (1984).

107. An additional reference for swept-energy studies is: J. J. Barton et. al., Phys. Rev. Lett., 51, 272 (1983).

113. Z. Hussain, L. F. Wagner, and C. S. Fadley, unpublished ARXPS results for the valence bands of Pt.
114. N. Erikson, Phys. Scr., 16, 462 (1977).
115. R. H. Williams, P. C. Kemeny, and L. Ley, Solid State Commun., 19, 495 (1976).
116. Z. Hussain, S. Kono, R. E. Connelly, and C. S. Fadley, Phys. Rev. Lett., 44, 895 (1980); Z. Hussain, C. S. Fadley, S. Kono, and L. F. Wagner, Phys. Rev., B 22, 3750 (1980).
117. G. D. Mahan, Phys. Rev., B 2, 4334 (1970), and review in Electron and Ion Spectroscopy of Solids, L. Fiermans, J. Vennik, and W. Dekeyser, eds., Plenum Press, New York (1978).
118. C. Caroli, D. Lederer-Rozenblatt, B. Roulet, and D. Saint-James, Phys. Rev., B 8, 4552 (1973).
119. P. J. Feibelman and D. E. Eastman, Phys. Rev., B 10, 4932 (1974).
120. N. J. Shevchik, J. Phys., C 10, L555 (1977); Phys. Rev., B 16, 3428 (1977).
121. L.-G. Petersson, Z. Hussain, S. Kono, and C. S. Fadley, Solid State Commun., 34, 549 (1980).
122. Z. Hussain, S. Kono, L.-G. Petersson, C. S. Fadley, and L. F. Wagner, Phys. Rev., B 23, 724 (1981).
123. L. F. Wagner, Z. Hussain, and C. S. Fadley, Solid State Commun., 21, 257 (1977).
124. J. Stohr, P. S. Wehner, R. S. Williams, G. Apai, and D. A. Shirley, Phys. Rev., B 17, 587 (1978).
125. P. Thiry, D. Chandesri, J. Lecante, C. Guillot, R. Pinchaux, and Y. Petroff, Phys. Rev. Lett., 43, 82 (1979).
126. T. C. Chiang, J. A. Knapp, M. Aono, and D. E. Eastman, Phys. Rev., B 21, 3513 (1980).
127. M. J. Sayers and F. R. McFeely, Phys. Rev., B 17, 3867 (1978).
128. G. Paasch, Phys. Status Solidi, B 87, 191 (1978).
129. Z. Hussain and C. S. Fadley, unpublished results of ARXPS direct-transition calculations for W with high angular resolution.
130. N. E. Christensen and B. Feuerbacher, Phys. Rev., B 10, 2349 (1974).
131. R. C. White, Z. Hussain, D. W. Shinn, and C. S. Fadley, unpublished experimental ARXPS valence data for W with ± 1.5° resolution.